MICROPIPETTE DEFLECTION EXPERIMENTS ON THE NEMATODE *C. elegans*

MICROPIPETTE DEFLECTION EXPERIMENTS ON THE NEMATODE *C. elegans*

By

RAFAEL D. SCHULMAN,
B.Sc. (University of Western Ontario)

A Thesis
Submitted to the School of Graduate Studies
in Partial Fulfillment of the Requirements
for the Degree
Master of Science

McMaster University

MASTER OF SCIENCE (2014) McMaster University
(Physics) Hamilton, Ontario

TITLE: Micropipette deflection experiments on the nematode *C. elegans*

AUTHOR: Rafael D. Schulman,
B.Sc. (University of Western Ontario)()

SUPERVISOR: Dr. Kari Dalnoki-Veress

NUMBER OF PAGES: x, 73

Abstract

This thesis describes the use of a micropipette deflection technique to measure the viscous forces experienced by the millimeter sized undulatory swimmer and model organism *C. elegans*. Using a specialized pipette, we are able to simultaneously measure both the lateral and propulsive forces acting on the worm. We find that the measured force curves are well described by Resistive Force Theory, which is a low Reynolds number hydrodynamic model. This work constitutes the first justification of its applicability at Reynolds numbers of this magnitude (roughly 0.1). Through our comparison with Resistive Force Theory, we extract the worm's drag coefficients, which are in agreement with an existing theoretical prediction. Through a simple scaling argument, we obtain a relationship between the size of the worm and the typical viscous forces, which is in good agreement with our data.

We also present a study aimed at measuring how the hydrodynamic forces on the worm change in proximity to solid boundaries. Using micropipette deflection, forces are measured at controlled distances from a single planar boundary and midway in between two parallel boundaries. We find the viscous forces and drag coefficients to increase significantly as the worm approaches a boundary. We find a constant value for the ratio of normal to tangential drag coefficients at all distances from a single boundary, but measure it to increase significantly as the worm is confined between two boundaries. In addition, the worm is seen to undergo a continuous gait modulation, primarily characterized by a decreased swimming amplitude, as it is subject to larger drag forces in confinement.

Finally, the interactions between two worms swimming nearby one another are probed. Worms are held adjacent to one another using micropipettes, and are found to tangle with each other, rather than interact hydrodynamically. We develop simple models that well capture the onset and probability of tangles as a function of the separation distance between the worms.

Preface

This is a "sandwich" thesis based on the papers published or submitted during my Master's, which have contributions from work I have done. The first chapter comprises an introduction to the relevant concepts necessary to understand the featured studies. The second chapter contains a detailed description of the experimental details, including methods and data analysis, pertinent to the papers. This chapter is also intended to aid those who are interested in utilizing some of the same methodologies or techniques that I have applied during my studies. Chapter 3 summarizes the main findings of each of the papers, and specifies the contributions I have made in the development of each. Finally, the conclusions of the thesis are presented in Chapter 4.

Acknowledgements

The last two years have been a whirl: moving back to Hamilton, forging new friendships, taking courses, making and breaking pipettes, and spending many hours in the lab playing with worms. There have been several people who have been there for me along the way, when I have most needed it. Here it is then, the many thanks I owe to those who have supported and guided me over the last two years.

First and foremost, I would like to thank my supervisor Kari, who has been an incredible mentor throughout these two years. His infectious enthusiasm and optimism have given me the drive and push I have needed to complete my research projects. With his simple ideas and inventive tricks, he has helped me surpass several of the experimental hurdles along the way, always leaving me amazed by his talent as an experimentalist. Although this comprises the end of my Master's, I am grateful to have another four years of his guidance to look forward to, as I begin my PhD.

I owe a great deal of credit to Matilda, for teaching me everything there is to know about worms and pipettes. She has always been extremely helpful, patient, and encouraging while training me to do experiments, discussing analysis, and editing my manuscripts. Further thanks go out to the rest of the members of the KDV experience for providing help when I have needed it, engaging in thought provoking discussions (often about surface tension), and always keeping me entertained. Special thanks to all the worms, who have bravely given their lives for my research.

Stepping outside of the physics building, I am thankful for the support of those close to me. My family has always encouraged, motivated, and supported me in my academic career. My parents, who are always proud of my accomplishments, have given me the confidence and ambition to pursue my interests. I am so grateful for all they have done for me. I would also like to thank all my friends, who have helped me unwind after a hard day's work. Last, but most certainly not least, I would like to thank my girlfriend Michelle. Her infinite emotional support has been so important to me over these two years. Throughout a rollercoaster of assignments, exams, failed experiments, practice talks (so many practice talks), paper rejections and unsuccessful appeals, she has been there for me and believed in me. I really am lucky to have such a wonderful person in my life.

Contents

List of Figures

Chapter 1

Introduction

Locomotion through a fluid environment is seen for organisms covering a vast range of length scales. However, the relevant physics describing the swimming of microscopic swimmers, or "microswimmers", differs considerably from that applicable to macroscopic swimmers. Macroscopic swimmers dwell in a fluid environment in which the flow is dominated by inertia, and viscous forces can be neglected. On the other hand, microswimmers are subjected to enormous viscous forces, and experience negligible inertial forces [1]. Since our intuition is derived from experiences with inertial macroscopic locomotion, the highly viscous environment of microswimmers is often found to be counterintuitive. However, over the last century, studies of all sorts (theoretical, experimental, and computational) have elucidated many of the properties of small scale swimming. Indeed, much remains to be learned in this subject, and it continues to be an active field of research. Although this research is important from a fundamental standpoint, it is also promising in terms of the potential applications it can offer, such as collective motion of bacteria to induce mixing in microfluidic devices [2, 3], fluid pumping [4–6], and microscopic robotic swimmers capable of towing loads for biomedical purposes such as robotic surgery and advanced drug targeting [7, 8].

Studying microswimming is not only interesting from physicist's point of view, but also highly relevant to biologists. In particular, bacteria, sperm, and other microorganisms often occupy fluid environments. To attain a full understanding of these systems, it is crucial that the physics is well understood. In particular, there are several questions that are of interest to both biologists and physicists. How do mi-

croswimmers attain propulsion in various environments? Can the propulsion strategy be optimized as the environment is changed? How do microscopic swimmers interact with nearby boundaries? What are the interactions between nearby swimmers? What type of collective effects can emerge from hydrodynamic and steric interactions within groups of swimmers? How well do current theoretical models describe the kinematics and forces of microswimmers?

A tremendous amount of experimental work has been done to begin to answer some of the questions above. Rapidly improving experimental techniques have allowed for direct imaging of microswimmers and the flow around them. However, to gain insight into the physics at work in these systems, it is often necessary to measure the forces that are involved in the swimming. In the last decade, direct force measurements of motile unicellular organisms have been achieved using optical traps [9, 10]. Such direct force measurements are often crucial for evaluating the success of theoretical models.

In this thesis, we present direct measurements on the undulatory swimmer *Caenorhabditis elegans* which probe the hydrodynamics forces involved in its swimming, as well as the interactions between two nearby worms. The experiments have been designed to shed light on some of the questions I have presented above. The outline of the thesis is as follows. In Chapter 1, a brief overview of the relevant concepts to this research is presented. The equations governing fluid flow will be presented, followed by a more in-depth look at the highly viscous regime, and the constraints microswimmers are faced with upon designing an effective propulsion strategy. Next, some milestone theoretical treatments of microswimmers are reviewed, including an introduction to Resistive Force Theory (RFT). Finally, there is a review on *C. elegans*, with a focus on its undulatory locomotion. In Chapter 2, the experimental methods employed in our experiments are described, including micropipette deflection, maintenance of *C. elegans* cultures, and image analysis. In Chapter 3, three manuscripts in which I have been a contributing author are presented. Paper I contains the first direct force measurement of swimming *C. elegans*, with a comparison to RFT as well as a simple scaling argument. Paper II takes a close look at the effects of nearby solid boundaries on the forces, drag coefficients, and swimming form of the worm. Paper III is a bit of a digression, in which the tangling between two adjacent worms is investigated.

1.0.1 Stopping distance of a bacterium

As will be explained in more detail later in this thesis, the physics governing swimming at length scales relevant to microscopic organisms is vastly different from that applicable to, for instance, humans swimming. To illustrate this point, I would like to work through a simple example. Consider a spherical bacterium of radius R_b, propelling itself through water with speed $v_{0,\mathrm{b}}$. At time $t = 0$, the bacterium ceases to propel itself. At this time, it will continue moving forward due to its inertia, but will experience a viscous drag force causing it to decelerate and eventually come to rest after some distance d, which is the quantity we wish to compute. We can apply Newton's second law to this problem

$$m_\mathrm{b} a_\mathrm{b} = F_\mathrm{d}, \tag{1.1}$$

where m_b is the mass of the bacterium, a_b is the acceleration of the bacterium, and F_d is the viscous drag force on a sphere, given by Stokes law

$$F_\mathrm{d} = -6\pi\mu R v, \tag{1.2}$$

in which μ is the viscosity of the fluid, R is the radius of the sphere, and v is the speed of the sphere [11]. Therefore, Eq. 1.1 becomes

$$m_\mathrm{b} a_\mathrm{b} = -6\pi\mu R_\mathrm{b} v_\mathrm{b}, \tag{1.3}$$

where v_b is the speed of the bacterium over time. We can roughly approximate the bacterium as a sphere of constant density ρ_b. Therefore,

$$\frac{4}{3}\pi R_\mathrm{b}^3 \rho_\mathrm{b} a_\mathrm{b} = -6\pi\mu R_\mathrm{b} v_\mathrm{b}. \tag{1.4}$$

Now we can apply the chain rule to the acceleration

$$a_\mathrm{b} \equiv \frac{\mathrm{d}v_\mathrm{b}}{\mathrm{d}t} = \frac{\mathrm{d}v_\mathrm{b}}{\mathrm{d}x_\mathrm{b}}\frac{\mathrm{d}x_\mathrm{b}}{\mathrm{d}t} = v_\mathrm{b}\frac{\mathrm{d}v_\mathrm{b}}{\mathrm{d}x_\mathrm{b}}, \tag{1.5}$$

where x_b is the position of the bacterium and we have used the fact that $v_\mathrm{b} \equiv \frac{\mathrm{d}x_\mathrm{b}}{\mathrm{d}t}$. Inserting Eq. 1.5 into Eq. 1.4 yields the differential equation

$$\frac{4}{3}R_\mathrm{b}^2\rho_\mathrm{b}\frac{\mathrm{d}v_\mathrm{b}}{\mathrm{d}x_\mathrm{b}} = -6\mu, \tag{1.6}$$

which is readily integrated

$$\int_{v_{0,\mathrm{b}}}^{0} -\frac{2}{9\mu}R_\mathrm{b}^2\rho_\mathrm{b}\mathrm{d}v_\mathrm{b} = \int_0^d \mathrm{d}x_\mathrm{b}. \tag{1.7}$$

Therefore, the stopping distance is given by

$$d = \frac{2}{9\mu}R_\mathrm{b}^2\rho_\mathrm{b}v_{0,\mathrm{b}}. \tag{1.8}$$

Now we can substitute in reasonable values for all parameters to estimate the stopping distance. The viscosity of water is $\mu \sim 1 \cdot 10^{-3}$ Pa· s, the radius of a bacterium is roughly $R_\mathrm{b} \sim 2$ μm, the typical speed is roughly $v_{0,\mathrm{b}} \sim 30$ μm/s, and we can approximate the density to be roughly equal to that of water $\rho_\mathrm{b} \sim 1 \cdot 10^3$ kg/m^3 [6]. Inserting these values into Eq. 1.8 gives $d \sim 0.3$ Å. This is truly a mind boggling result, as this distance is many orders of magnitude smaller than the size of the bacterium, and is even smaller than a typical atomic radius. In comparison, a human swimming could typically coast on the order of a body length after a typical breast stroke. Essentially, the bacterium stops instantaneously as if it had no inertia. In the next few sections, I will explore the equations governing fluid flow to illustrate why this striking result comes about and what it implies.

1.1 The Navier-Stokes equations

The term "fluid" categorizes matter which continuously deforms (or flows) when subjected to a shearing stress [12]. Although the definition seems specific, it is a fairly broad category which includes gases, liquids, and even entire galaxies. Despite the apparent breadth and dissimilarity within this category, there is a single set of equations that governs the flow of all fluids. These equations are known as the Navier-Stokes equations

$$\rho\left(\frac{\mathrm{d}\mathbf{u}}{\mathrm{d}t}+\mathbf{u}\cdot\nabla\mathbf{u}\right)=-\nabla p+\mu\nabla^2\mathbf{u}+\mathbf{f}, \tag{1.9}$$

where $\mathbf{u}=(u,v,w)$ is the velocity field of the fluid with u,v,w as the x,y,z components of this field, ρ is the density of the fluid, p is the pressure field, and $\mathbf{f}$ represents any body forces acting on the fluid [11]. Since the fluid velocity is a field, the quantities u,v,w,p, and $\mathbf{f}$ are functions of position $\mathbf{x}=(x,y,z)$. In addition, if the fluid is incompressible, the following condition is also included

$$\nabla\cdot\mathbf{u}=0\ . \tag{1.10}$$

These equations comprise a system of four coupled partial differential equations, which are non-linear ($\mathbf{u}\cdot\nabla\mathbf{u}$ term) and second order ($\nabla^2\mathbf{u}$ term). For these reasons, these equations are notoriously difficult to solve. In fact, the equations are so difficult that the Clay Mathematics Intitute has offered $1,000,000 for the one capable of proving whether, for a given set of boundary conditions, solutions to the equations exist and are unique [13]. Exact analytical solutions can only be obtained under special circumstances in which either symmetries or appropriate approximations permit enormous simplifications to the governing equations [11, 14].

Although complicated, the Navier-Stokes equations are simply a statement of Newton's second law for a unit fluid volume. The left hand side of Eq. 1.9 corresponds to ma in Newton's second law, and as such, the left hand terms are often termed the "inertial terms" [11]. The right hand side of Eq. 1.9 represent the sum of all forces acting on a fluid volume, such as pressure gradients ($-\nabla p$), viscous drag ($\mu\nabla^2\mathbf{u}$), and body forces such as gravity.

As with any partial differential equation including spatial derivatives, appropriate boundary conditions are necessary to completely solve a problem at hand. For instance, a hydrodynamic boundary condition is needed to dictate how the velocity field behaves at a fluid-solid boundary. In this case, the relevant boundary condition is typically the no-slip condition [11, 14]. This boundary condition fixes the fluid velocity at the fluid-solid interface to be equal to that of the solid (velocity continuity). Therefore, if the boundary is at rest, the fluid at the interface must also be at rest.

1.2 The Reynolds number

In many cases, some of the terms in Eq. 1.9 are negligible and can effectively be removed from the equation. For instance, we often deal with flows in which any body forces are small compared to the other relevant forces, so $\mathbf{f}$ can be ignored (and will be for the remainder of this section). In particular, finding a regime in which the inertial term can be ignored would be beneficial, as this would render Eq. 1.9 linear, and hence much more tractable. To gain insight into the circumstances in which such an approximation can be made, we can non-dimensionalize the inertial term. We let $\mathbf{u} = V\tilde{\mathbf{u}}$, where V is the typical velocity scale of the flow and a tilde indicates a non-dimensionalized variable. In addition, we can set $\mathbf{x} = L\tilde{\mathbf{x}}$ and $t = \frac{L}{V}\tilde{t}$, where L is a typcal length scale of the flow. Derivatives can be handled using the chain rule

$$\frac{\mathrm{d}}{\mathrm{d}t} = \frac{\mathrm{d}\tilde{t}}{\mathrm{d}t}\frac{\mathrm{d}}{\mathrm{d}\tilde{t}} = \frac{V}{L}\frac{\mathrm{d}}{\mathrm{d}\tilde{t}}, \tag{1.11}$$

$$\nabla = \left(\frac{\partial}{\partial x}, \frac{\partial}{\partial y}, \frac{\partial}{\partial z}\right) = \left(\frac{\partial\tilde{x}}{\partial x}\frac{\partial}{\partial\tilde{x}}, \frac{\partial\tilde{y}}{\partial y}\frac{\partial}{\partial\tilde{y}}, \frac{\partial\tilde{z}}{\partial z}\frac{\partial}{\partial\tilde{z}}\right) = \frac{1}{L}\left(\frac{\partial}{\partial\tilde{x}}, \frac{\partial}{\partial\tilde{y}}, \frac{\partial}{\partial\tilde{z}}\right) = \frac{1}{L}\tilde{\nabla} \tag{1.12}$$

Thus, the inertial term becomes

$$\begin{aligned}\rho\left(\frac{\mathrm{d}\mathbf{u}}{\mathrm{d}t} + \mathbf{u}\cdot\nabla\mathbf{u}\right) &= \rho\left(\frac{V}{L}\frac{\mathrm{d}(V\tilde{\mathbf{u}})}{\mathrm{d}\tilde{t}} + (V\tilde{\mathbf{u}})\cdot\frac{1}{L}\tilde{\nabla}(V\tilde{\mathbf{u}})\right) \\ &= \frac{\rho V^2}{L}\left(\frac{\mathrm{d}\tilde{\mathbf{u}}}{\mathrm{d}\tilde{t}} + \tilde{\mathbf{u}}\cdot\tilde{\nabla}\tilde{\mathbf{u}}\right).\end{aligned} \tag{1.13}$$

As seen in Eq. 1.13, the typical magnitude of the inertial term scales as $\rho V^2/L$. We can perform the same analysis on the viscous term

$$\mu\nabla^2\mathbf{u} = \mu\frac{1}{L^2}\tilde{\nabla}^2(V\tilde{\mathbf{u}}) = \frac{\mu V}{L^2}\tilde{\nabla}^2\tilde{\mathbf{u}}, \tag{1.14}$$

and as seen, the typical magnitude of this term scales as $\mu V/L^2$. We can now define a quantity referred to as the Reynolds number (Re) as the ratio of typical inertial to

viscous forces [11, 14]

$$\mathrm{Re} = \frac{\rho L V}{\mu}. \tag{1.15}$$

For flows of large length scales, high speeds, and/or in low viscosity fluids, Re >> 1 and the inertia of the flow dominates the viscous forces present. In this high Re regime, the viscous term may be removed from Eq. 1.9, rendering the equations first order. However, the non-linear term is intact, which poses difficulties. In particular, in this regime, one is faced with complicated behaviours such as turbulence, chaotic eddies, and vortices [11]. The chaotic nature of this regime imposes difficulties for generating accurate weather predictions, for instance. In predicting the weather, these equations must be solved numerically given some initial conditions. However, due to the presence of chaos, slight variations in the initial conditions may lead to vastly different outcomes [15].

The focus of this thesis will be on the low Re regime, in which viscous forces dominate, and the equations governing the fluid dynamics become linear, making them more tractable

$$0 = -\nabla p + \mu \nabla^2 \mathbf{u}. \tag{1.16}$$

This regime is characteristic of flows of small length scales, low speeds, and/or in high viscosity fluids. In this regime, the flow is laminar (fluid flows in parallel layers), smooth and steady [11, 14].

To address the reason behind the vastly different stopping distances for a bacterium swimming in comparison to a human swimming, we can compute the Reynolds number for each case. For the example of the bacterium swimming in water, a characteristic length scale of the flow will be on the order of $R_\mathrm{b} \sim 2$ μm, and a characteristic velocity of the flow will be on the order of $v_{0,\mathrm{b}} \sim 30$ μm/s. Inputting these values into Eq. 1.15 gives Re $\sim 6{\cdot}10^{-5}$. Evidently, a bacterium lives in a world in which viscous forces are nearly a million times stronger than inertial forces. For this reason, a microscopic swimmer, or microswimmer, can be well approximated as having no

inertia [1,6]. On the other hand, a human swimming in water may involve flow length scales of $L \sim 1$ m and velocity scales of $V \sim 1$ m/s, such that Re $\sim 1{\cdot}10^6$. Humans experience swimming that is inertia-dominated, and viscous forces can justifiably be ignored. Therefore, since Re differs by roughly 11 orders of magnitude, it is not surprising that the physics describing swimming of microscopic organisms is so different from that applicable to humans. It is these enormous viscous forces that cause the bacterium described in the beginning of this chapter to come to rest so abruptly, whereas the inertial flow that humans experience allows for coasting.

1.3 Time reversibility: the Scallop Theorem

There are some interesting consequences associated with living in the low Re regime. In the opening example of this chapter, we saw that the motion of the bacterium ceased essentially instantaneously once the bacterium stopped propelling itself. That is, in the low Re regime, since inertia does not exist, flow is instantaneously generated in response to a force, and vanishes equally quickly once the force is removed. Similarly, due to the absence of inertia, an unbalanced force on a low Re swimmer, will produce an infinite acceleration. Consequently, the swimmer's speed will change infinitely quickly, until it moves at such a speed that the viscous drag force acting on it perfectly cancels the unbalanced force, and hence there is no net force on the swimmer and it moves with a constant speed [16]. For this reason, the instantaneous speed (and therefore displacement) of the object itself, is solely determined by the forces acting on it in that instant of time, and independent of any events of the past. This time-independence at low Re is clear upon inspection of Eq. 1.16, from the absence of t [1,16,17]. Another important property of Eq. 1.16 is that it is linear. This linearity, along with the time-independence, has an important consequence: namely, the scallop theorem. The scallop theorem states that if a low Re swimmer's sequence of body motions is invariant under time-reversal, the swimmer will attain no net propulsion. This striking point was made by Nobel Prize winner Edward Purcell in his famous 1976 lecture "Life at low Reynolds number" [1].

To understand the implications of this notion, let us think about what an organism must do to swim. To move in a fluid, an organism must change its body shape in

some way that will generate propulsion. Of course, the sequence of deformations performed by the organism must in some way be cyclical, in order to keep swimming. During these derformations, the only forces acting on the body are those exerted by the fluid, and for each cycle, the swimmer aims to experience a net displacement in some direction. Now, let us consider a type of swimming cycle which involves "reciprocal motion", defined to be a cycle of body motions in which the body first performs a sequence of motions to deform itself in a particular way, and then follows by an exact reversal of the shape changing motions (although potentially done at different rates). In other words, the sequence of body motions is invariant under time-reversal. Reciprocal motion is exemplified by the scallop, which lives at high Re. It simply opens and closes its hinge. As seen in the first column of Fig 1.1, it opens its shell very slowly, as such does not push against the water appreciably, and does not gain much momentum towards the left. To complete the cycle, it quickly closes its shell, and in doing so, pushes water towards the left, and attains momentum towards the right, coasting a distance in that direction. However, at low Re, according to the scallop theorem, the displacements attained from some set of motions will be perfectly cancelled by the displacements attained during the reversal of those motions. Therefore, if a scallop lived at low Re, where the relevant forces are viscous and not inertial, it would make no net progress. As seen in the second column of Fig. 1.1, when it opens its shell slowly, it generates a small viscous force towards the left but over a long time. However, when the shell closes quickly, the larger viscous force propels the scallop towards the right over a shorter time, finally attaining no net displacement. That is the essence of the scallop theorem.

1.3.1 Circumventing the Scallop Theorem

Of course, there are numerous ways of escaping the constraints posed by the scallop theorem and attaining propulsion at low Re. For instance, due to hydrodynamic interactions, two swimmers undergoing time-reversible motion in proximity to one another can actually attain net displacements [17,18]. In the same way, if a reciprocal swimmer interacts with a nearby flexible boundary, propulsion may be attained [17]. Furthermore, if the fluid is non-Newtonian, the scallop theorem is no longer valid, and the reciprocal swimmer can attain propulsion [17]. This case is particularly relevant

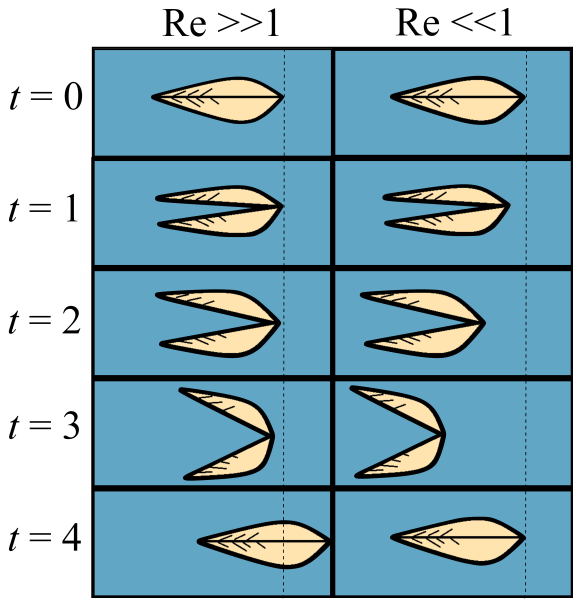

Figure 1.1: Schematic of scallop propulsion at high and low Re at equally spaced snapshots (down a column). At high Re (left column), the scallop can open its shell slowly and deliver little momentum to the fluid, and in turn, move very little towards the left. Upon quickly shutting its shell, it pushes water towards the left and experiences a large force, coasting towards the right. At the end of the sequence, the scallop has attained a net displacement towards the right. At low Re (right column), the scallop opens its shell slowly and experiences a small viscous force towards the left, albeit over a long time, and moves a considerable distance towards the left. Upon quickly closing its shell, it experiences a large viscous force towards the right, but over a short time, and returns to its original position, indicated by the vertical dotted line.

for biological swimmers, since those often swim through complex fluids. However, to ensure propulsion at low Re, microscopic swimmers have developed a variety of propulsion strategies in which the swimming motions are not time reversible.

A familiar non-reciprocal propulsion mechanism of microswimmers is the helical rotation of flagella [19]. This mechanism is commonly used by bacteria, such as *E. coli*. If a single cell has several flagella, the flagella tend to form bundles which move in unison [19]. In the case of *E. coli*, the flagellar bundle forms a stiff helix that is rotated by a motor within in the cell wall, reminiscent of a corkscrew. Another interesting mechanism is utilized by *Chlamydomonos reinhardtii*, an alga cell which has two flagella [20,21]. This organism is capable of bending its two flagella in unison, to generate motion akin to that of a human breast stroke. Other organisms, such as

Paramecium generate propulsion through the periodic, coordinated, beating of short, thin filaments which cover the cell body, called cilia [22].

Another popular mechanism of propulsion is undulatory locomotion, in which travelling waves are propagated down the length of the swimmer. This form of locomotion is known to be efficient, and is most popular among organisms which are long and slender [23]. For instance, sperm of many species actuate an undulatory beating of a single flagellum using molecular motors distributed along the flagellum [6]. Undulatory locomotion is also the propulsion strategy of most nematodes [24]. In fact, the nematode and model organism *Caenorhabditis elegans* undergoes undulatory locomotion, and is commonly employed as the subject of studies concerning this form of locomotion. Since undulatory locomotion is straightforward to describe mathematically, it is a popular choice of theoretical studies focusing on low Re swimming.

1.4 Theoretical treatments of microswimmers

In this section, I will briefly present some milestone theoretical works aimed at describing the hydrodynamics associated with undulatory swimming at low Re. Of course, there is a sufficient volume of excellent theoretical studies that I will only be scratching the surface. We will begin with the first and simplest treatment- Taylor's swimming sheet.

1.4.1 Taylor's swimming sheet

Taylor pioneered the theoretical treatments of microswimmers in his 1951 work, where he aimed to learn how microorganisms can attain propulsion using viscous forces rather than imparting momentum to the surrounding fluid [25]. To answer this question, he considered the viscous flow generated by propagating transverse travelling waves down a sheet, as seen in Fig 1.2. The sheet is infinite in extent in the y-direction, thereby rendering the problem 2-dimensional. It produces travelling waves of speed v_{wave} with a given amplitude (b), wavenumber ($k = 2\pi/\lambda$), and angular frequency (ω). To simplify the problem, only small amplitudes (in comparison to the wavelength) are considered, such that $kb << 1$. In Taylor's work, Eq. 1.16 is solved given the no-slip boundary condition at the surface of the sheet, and the boundary

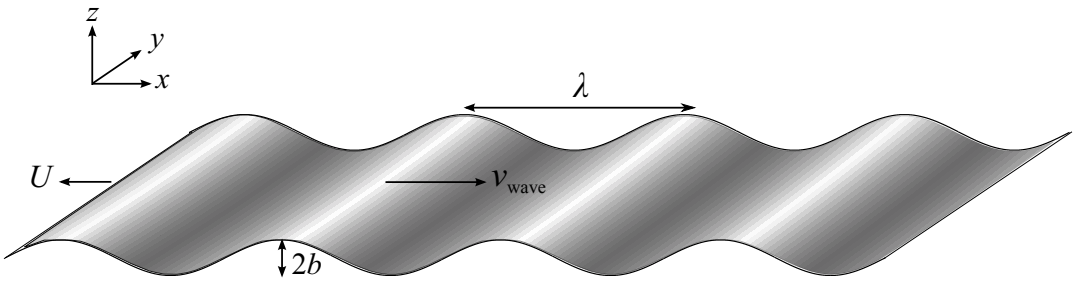

Figure 1.2: Taylor's swimming sheet propagating travelling waves of speed v_{wave} in the positive x-direction. The waves have an amplitude of b which is much smaller than the wavelength λ. The resultant propulsion speed of the sheet is U in the opposite direction as of the travelling wave velocity. The sheet is considered to be infinite in the y-direction.

condition that the flow must vanish at infinity [25]. Taylor finds that the sheet does attain a propulsion velocity (U)

$$U = -\frac{1}{2}\omega k b^2 = -\frac{1}{2} v_{\text{wave}} (kb)^2, \tag{1.17}$$

which is in the opposite direction as the velocity of the travelling wave. The propulsion speed of the sheet is much smaller than the wave speed, since $kb << 1$. An interesting point to be made here is that U does not depend on the viscosity of the fluid. Although it seems odd at first glance, it can be simply understood. The propulsive force (F_{P}), which is derived from viscous forces, scales linearly with the viscosity ($F_{\text{P}} = \mu\ f(\omega, k, b)$ in general). The waving sheet will have a forward speed that generates a resistive drag force (F_{d}). This drag force scales linearly with μ as well as U (in general, $F_{\text{d}} = U\mu\ g(\omega, k, b)$). However, as discussed in Sec. 1.3, low Re swimmers must experience a zero net force: $F_{\text{P}} + F_{\text{d}} = 0$. Then it follows that $U = -f/g$, and is independent of the viscosity.

Thus, Taylor showed that by propagating transverse waves down a sheet with only viscous forces present, a net propulsion can be attained in the direction opposite to the travelling waves. Further work has extended Taylor's waving sheet result, by for instance including the effects of a nearby boundary [26]. In this work, it was found that if the waveform of the sheet is fixed, the propulsion speed increases as

it approaches the boundary. On the other hand, if the power the sheet can exert is constant (and the waveform is allowed to change), the propulsion speed decreases upon approaching the boundary.

1.4.2 Stokeslets and moving slender rods

Since Eq. 1.16 is linear, the method of Greens functions may be used to solve problems. In this method, the flow and pressure fields are found for a point driving term (in this case represented by a point force in the fluid $\mathbf{F}\delta(\mathbf{x}-\mathbf{x}')$, localized at some point $\mathbf{x}'$). The flow field from the singular force is termed a "stokeslet". Subsequently, the flow from an extended object exerting a force on the fluid may be solved by a linear superposition of stokeslets spaced along the object [6, 27, 28].

Let us consider a slender cylinder of length L_c and radius r_c ($r_c/L_c << 1$) being pushed by some force (F_c) to move either tangential to its central axis ($F_{c,T}$) or normal to it ($F_{c,N}$) at low Re [6]. Slender cylinders are relevant, because undulatory swimmers and flagella are typically very long and thin. Since the cylinder is slender, the flow around it can be simply represented by a line of N stokeslets along its axis, each of strength $F_{c,T}/N$ or $F_{c,N}/N$. Thereafter, several approximations can be made, such as only keeping terms which are leading order in $\ln(r_c/L_c)$. In addition, end effects can be ignored by looking only at the flow induced at segments far from the ends (near the center). Subsequently, the expression for the flow as a function of the driving force is inverted. In this way, the final result yields the force needed to keep the cylinder in motion (alternatively, the drag force acting on the cylinder) at some speed. The result is that the drag force per unit length ($f_{c,T}$ or $f_{c,N}$) is linearly proportional to the speed

$$f_T = -c_{c,T} v_{c,T} \mu \tag{1.18}$$

$$f_N = -c_{c,N} v_{c,N} \mu, \tag{1.19}$$

where $v_{c,T}$ and $v_{c,N}$ are the speeds of the cylinder in motion tangential and normal to its central axis, and $c_{c,T}$ and $c_{c,N}$ are tangential and normal drag coefficients per unit length of the cylinder [6]. From the calculation, the drag coefficients can be evaluated

to be

$$c_{\mathrm{c,N}} = 2c_{\mathrm{c,T}} = \frac{4\pi}{\ln(L_{\mathrm{c}}/r_{\mathrm{c}})}. \tag{1.20}$$

There are two important messages to learn from this calculation. First of all, a straight slender cylinder in motion tangential or normal to its axis experiences a drag force which is linearly proportional to its translation speed. Second, the tangential and normal constants of proportionality are different. As we will see, this anisotropy in the drag coefficients is critical for an undulatory microswimmer (and in fact, for any undulator) to attain propulsion [6, 16]. The results of the calculation above form the basis of Resistive Force Theory (RFT).

1.4.3 Resistive Force Theory (RFT)

In RFT, a slender swimmer moving at some velocity can be broken down into infinitesimal body segments ($\mathrm{d}l$), each moving relative to the fluid with a velocity that can be decomposed into a component tangential (v_{T}) and normal (v_{N}) to the body [6, 16, 24, 27–30]. Each segment velocity induces an opposing drag force ($\mathrm{d}F$), given by

$$\mathrm{d}F_{\mathrm{T}} = -c_{\mathrm{T}} v_{\mathrm{T}} \mu \ \mathrm{d}l, \ \mathrm{d}F_{\mathrm{N}} = -c_{\mathrm{N}} v_{\mathrm{N}} \mu \ \mathrm{d}l, \tag{1.21}$$

where c_{T} and c_{N} are the tangential and normal drag coefficients, which are constants over the length of the slender swimmer. The drag coefficients can either be determined experimentally or calculated for a particular geometry (as done previously for case of the straight cylinder, for instance). Once the drag coefficients are known, it is possible to determine the propulsive force and speed of the swimmer given simply the motion sequence of its body. Therefore, RFT is a simplistic model to apply in practice, and is lucrative when complex hydrodynamic calculations wish to be avoided. RFT has recently been tested and validated using high-speed imaging of sperm and bacteria [31–33]. RFT has also proven successful when compared with direct force measurements of *E. coli* using optical traps [10]. In addition, our work

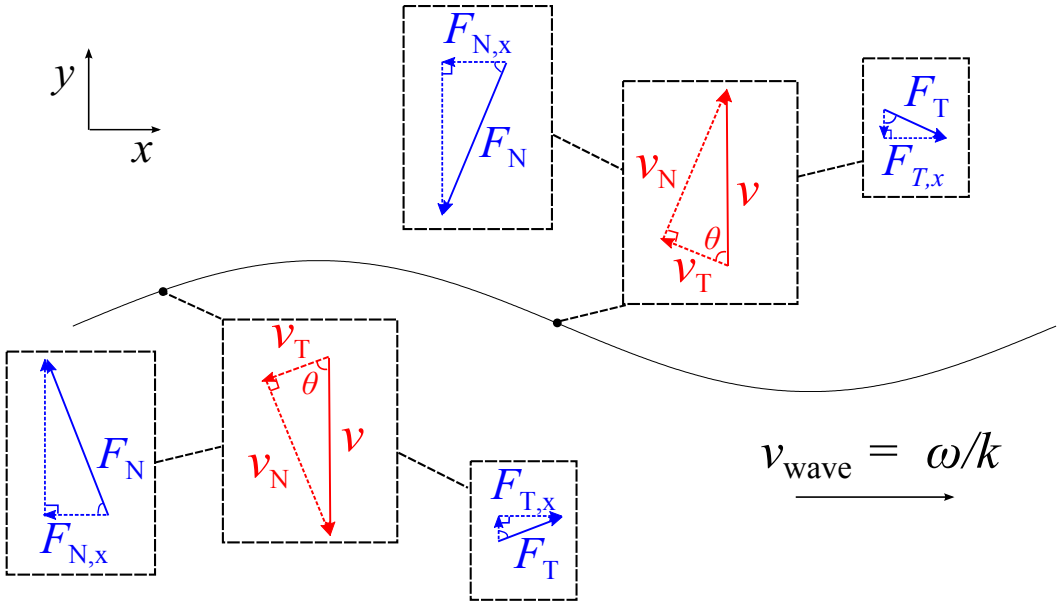

Figure 1.3: A sinusoidal undulatory microswimmer propagating travelling waves in the positive x-direction. The velocity of the undulator's body, v, can be decomposed into components normal (v_N) and tangential (v_T) to the body. These velocities generate drag forces in the opposite directions (F_N and F_T). The force F_N always has a component in the negative x-direction (positive propulsive direction), whereas the force F_T always has a component in the positive x-direction (negative propulsive direction). In all cases, the angle arc represents the angle θ.

in Paper I and Paper II provide direct quantitative verification of RFT in terms of predicting the hydrodynamic forces involved in the swimming of *C. elegans*.

As an illustration of RFT, let us examine the case of a simple undulator propagating travelling waves of the form $y(x,t) = A\sin(kx - \omega t)$ down its body. The velocity of the body will be $v = \dot{y} = -A\omega\cos(kx - \omega t)$. As seen in Fig. 1.3, we can decompose the velocity into the normal and tangential components $v_N = v\sin\theta$, $v_T = v\cos\theta$, where θ is the angle between the tangential velocity component and the vertical. Using Eq. 1.21, we must then have

$$\mathrm{d}F_T = -c_T\mu v\cos\theta\ \mathrm{d}l,\ \mathrm{d}F_N = -c_N\mu v\sin\theta\ \mathrm{d}l. \tag{1.22}$$

As seen in Fig. 1.3, at all points on the undulator's body, the normal component of the drag force has a component along the negative x-direction (positive propulsive

direction), whereas the tangential component of the drag force has a component along the positive x-direction (negative propulsive direction). Therefore, the net propulsive viscous force for each segment is

$$\mathrm{d}F_{\mathrm{P}} = |\mathrm{d}F_{\mathrm{N,x}}| - |\mathrm{d}F_{\mathrm{T,x}}| = |\mathrm{d}F_{\mathrm{N}} \cos\theta| - |\mathrm{d}F_{\mathrm{T}} \sin\theta|, \tag{1.23}$$

$$\mathrm{d}F_{\mathrm{P}} = (c_{\mathrm{N}} - c_{\mathrm{T}}) A\mu\omega |\cos(kx - \omega t) \sin\theta \cos\theta| \, \mathrm{d}l \tag{1.24}$$

along the negative x-direction (positive propulsive direction), that is, in the opposite direction as the travelling wave. To find the total propulsive force, Eq. 1.24 must be integrated over the body of the undulator. However, the important point has already been made, the propulsive force of an undulator is simply proportional to $(c_{\mathrm{N}} - c_{\mathrm{T}})$ according to RFT. Thus, if we define $K = c_{\mathrm{N}}/c_{\mathrm{T}}$, we see that if $K > 1$, an undulatory swimmer will propel itself in the opposite direction as its travelling wave. If $K < 1$, we are faced with the curious case of the undulator moving in the same direction as its travelling wave. Importantly, if $K = 1$, the swimmer can attain no net propulsion, which raises the important point that *a microswimmer must have an anisotropy in its drag coefficients in order to propel itself forward* [6, 16, 28, 29].

Luckily, for a non-spherical object, there is usually an inherent anistropy in the drag coefficients. For an infinite cylinder, K approaches a limiting value of 2. For most undulatory microswimmers, such as nematodes, this value is typically within the range of 1-2 [6, 16, 24].

To attain theoretical estimates of the drag coefficients for a slender low Re undulator, Gray and Hancock performed a similar analysis as we did in Sec. 1.4.3 [27, 29]. However, in their calculation, they consider the flow around a cylinder (of radius r_{c}) that is propagating travelling sinusoidal waves (of wavelength λ) down its length. In their work, they also include higher order flow singularities, to better approximate the velocity field around the cylinder. Finally, the average drag coefficients they derive are different from the straight cylinder (Eq. 1.20):

$$c_{\mathrm{N}} = 2c_{\mathrm{T}} = \frac{4\pi}{\ln(2\lambda/r_{\mathrm{c}}) - \frac{1}{2}}, \tag{1.25}$$

where there is now a dependence on the wavelength of the undulator, rather than the length of the cylinder. On the other hand, the value of K is still exactly equal to 2. In addition, by applying a similar analysis to the propulsive force calculation from earlier in this section, and balancing this propulsive force with the resistive drag felt during forward propulsion, Gray and Hancock developed a prediction for the swimming speed of an undulatory microswimmer

$$U = 2\pi^2 f \lambda \frac{\left(\frac{A}{\lambda}\right)^2 (K-1)}{1 + 2\pi^2 K \left(\frac{A}{\lambda}\right)^2}, \tag{1.26}$$

where A and f are the amplitude and undulation frequency of the undulatory swimmer, and a positive value of U denotes the swimmer moving in the opposite direction of its travelling waves [24, 29]. Once again, we see that if K=1, the swimmer attains no net propulsion. However, Gray and Lissman found that using $K = 2$, Eq. 1.26 yields predictions of swimming speeds that are larger than those they had observed for several species of swimming nematodes [24]. In fact, their estimates of K ranged between 1.5 and 2. In the same set of experiments, they dropped thin wires into highly viscous solutions and measured their fall speeds. In doing so, they found $K \sim 1.5$, smaller than the expected value of 2.

In an attempt to refine the drag coefficient estimates of Gray and Hancock (Eq. 1.25), Lighthill performed a more careful analysis, in which hydrodynamic interactions between different segments of the undulator's body are accounted for in more detail [28]. Lighthill's derivation is carried out for the helical rotation of a filament; however, it is also applicable to undulatory locomotion of small amplitude (although Lighthill does state that he would expect the results to apply even for undulatory waves of arbitrary amplitude). The drag coefficients are given by

$$c_{\mathrm{N}} = \frac{4\pi}{\ln(0.18\Lambda/r_{\mathrm{c}}) + \frac{1}{2}}, \; c_{\mathrm{T}} = \frac{2\pi}{\ln(0.18\Lambda/r_{\mathrm{c}})}, \tag{1.27}$$

and their ratio is

$$K = 2\frac{\ln(0.18\Lambda/r_c)}{\ln(0.18\Lambda/r_c) + \frac{1}{2}}, \tag{1.28}$$

where Λ is the wavelength of the undulator as measured along its body (as opposed to along its central axis). Lighthill's study does include a slenderness approximation, and thus, one should only consider cases where $\Lambda >> r_c$. Indeed, for a real undulatory swimmer, the wavelength is much larger than the radius, so the assumption is valid (for example, $\Lambda/r_c \sim 40$ for the nematode *C. elegans*). Eq. 1.28 produces a K value between 1 and 2, when $\Lambda/r_c \gtrsim 9$, and increases asymptotically towards 2 as $\Lambda/r_c \to \infty$ (the limit of a straight cylinder).

1.5 Swimming near a boundary

Up until now, we have focused on the case in which the microswimmer is moving in an effectively infinite, or unbounded, fluid, in which boundary effects can be ignored. However, boundary effects are important to consider due to their biological relevance. There are several systems in which microorganisms move near an interface, such as in biofilm formation [34, 35], sperm locomotion in the female reproductive tract [36], and in bacterial infections which are surface-associated [37, 38]. In order to fully comprehend the dynamics within these systems, it is necessary to understand how the physics of a single microswimmer is modified by the presence of a nearby boundary.

The nature of viscous forces is that they oppose gradients in the fluid velocity field [11]. For instance, in laminar flow, the difference in velocity between adjacent layers leads to a friction force (or a dissipation of momentum) between the layers. As an example, for a unidirectional laminar flow pointing in the x-direction which only contains a velocity gradient in the y-direction ($\mathbf{u} = u(y)\hat{\mathbf{x}}$), the magnitude of the viscous shear stress (τ) is given by

$$\tau = \mu\frac{\partial u}{\partial y}, \tag{1.29}$$

and is thus proportional to the gradient in the fluid velocity field [11]. Now, instead, imagine the flow below a cylinder moving perpendicular to its axis in the positive

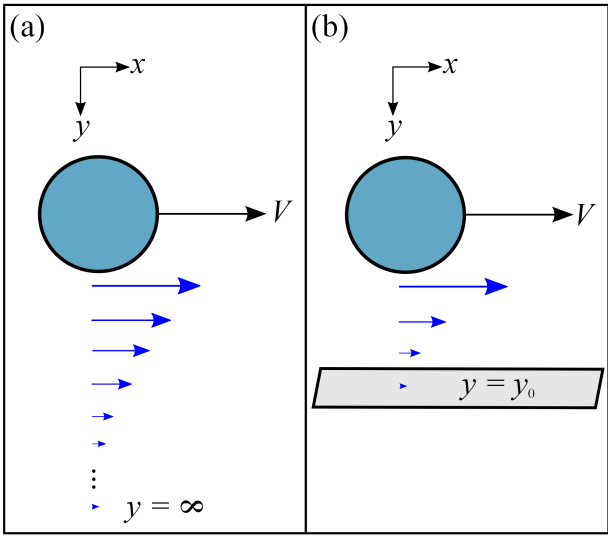

Figure 1.4: Approximate velocity field (blue arrows) below a cylinder (looking edge on) translating normal to its axis with velocity V (black arrow) in the positive x-direction in (a) an infinite fluid and (b) near a solid boundary located at y_0. In an infinite fluid, the velocity below the cylinder is equal to V at the fluid-cylinder interface and equal to 0 at infinity. When a solid boundary is placed at $y = y_0$, the velocity must equal zero at the fluid-solid boundary, thereby increasing the velocity gradient in the fluid near the cylinder.

x-direction in an unbounded fluid, with some velocity V, as seen in Fig. 1.4(a). Due to the no-slip condition (mentioned in Sec. 1.1), the fluid velocity at the cylinder-fluid interface must be equal to V. On the other hand, the fluid must be at rest infinitely far from the cylinder. Interpolating the rest of the field, we see that there is a velocity gradient in the y-direction, which will generate a viscous force on the cylinder. Now imagine that a solid planar surface is placed below the cylinder, as seen in Fig. 1.4(b). As dictated by the no-slip boundary condition, the fluid velocity field at this planar interface must be zero, while still fulfilling that the fluid velocity at the cylinder surface be V. Interpolating the rest of the field, the net result is that the gradient in the fluid velocity below the cylinder is greater in the presence of the boundary than it was in an infinite fluid. Therefore, a translating cylinder (or a microswimmer), will experience larger viscous forces near a solid boundary due to the increased velocity gradient.

Some theoretical studies have investigated the effects of the increased viscous

forces due to nearby boundaries on the propulsion and trajectories of low Re swimmers [26, 39–41]. If the swimmer operates at a constant power output, its waveform is often subject to change due to the presence of a boundary [26, 39, 41]. On the other hand, if the waveform is held constant, propulsion increases near a boundary, albeit so does the power output required by the swimmer [26, 39, 41]. Experiments have confirmed changes in both propulsion, trajectories, and swimmer waveform near solid boundaries [42–44]. In one study, bull spermatozoa swam faster and with a different waveform and frequency, while in proximity to a boundary [42]. However, there is a need for more detailed observations, including direct force measurements, of microswimmers at controlled distances from boundaries to test many of the predictions made by theoretical studies. In Paper II, we perform such measurements on *C. elegans*, and measure significant increases in the viscous forces, and observe a modification to the swimming waveform at close proximity to boundaries.

To derive the RFT drag coefficients for a slender object near a boundary is more difficult than in an infinite fluid. In particular, the slender object cannot simply be replaced by a sequence of stokeslets (and higher order singularities), but an appropriate image system of flow singularities (including stokeslets oriented in the opposite direction) is also needed in order to satisfy the no-slip boundary condition at the surface [40]. Thus, it is not surprising that a full derivation for the drag coefficients of an undulating cylinder near a boundary has not been carried out. The most applicable study has been carried out by Katz *et al.*, in which the case of a slender cylinder moving parallel to a planar solid boundary is considered [40]. In their analysis, they restrict the calculation to an intermediate regime in which $r_c << h << L_c/2$, where h is the distance from the center of the cylinder to the boundary. By considering the cylinder moving both tangential and normal to its axis, Katz *et al.* derive the resistance coefficients

$$c_N = 2c_T = \frac{4\pi}{\ln(2h/r_c)}, \tag{1.30}$$

and, once again, K=2 in this case and does not vary with h. As we see, the drag coefficients are similar to those for a cylinder in an infinite fluid (Eq. 1.20), but here, h replaces L_c as the relevant length scale in the logarithm. In the same study, Katz *et*

al. consider the same cylinder located midway between two parallel planar boundaries (a distance h away from each), and, once again, moving in directions parallel to the boundaries. The analysis is still restricted to the regime $r_c << h << L_c/2$. In this case, the drag coefficients are

$$c_N = \frac{4\pi}{\ln(2h/r_c) - 1.609},\ c_T = \frac{2\pi}{\ln(2h/r_c) - 0.453}, \tag{1.31}$$

and their ratio is

$$K = 2\frac{\ln(2h/r_c) - 0.453}{\ln(2h/r_c) - 1.609}. \tag{1.32}$$

Therefore, in confinement between two boundaries, the value of K does vary with h. Specifically, both c_N and c_T increase as the cylinder approaches the bounday; however c_N increases faster, causing K to increase in proximity to a boundary. Surprisingly, for $h/r_c >> 1$ (as assumed in the derivation) but still finite, K is larger than 2! Specifically, $K \to \infty$ at $h/r_c \sim 2.5$ and decreases monotonically towards $K = 2$ as $h/r_c \to \infty$. This case comprises the first time we have seen the value of K exceeding the typical limiting value of 2. Thus, we might anticipate that slender undulatory swimmers will also experience a value of $K > 2$ in such channel confinement. As a result, undulatory microswimmers confined in a channel would attain a larger propulsive force (which scales with $c_N - c_T$, as seen in Eq. 1.24) and a greater propulsion speed, in accordance with Eq. 1.26. Direct measurements of microswimmers at controlled distances from boundaries are needed in order to quantitatively test these predictions. In Paper II, the drag coefficients of *C. elegans* are measured and quantitatively compared with the predictions of Katz *et al.* In particular, Eq. 1.30 compares well to the experimental values, and indeed, a value of $K > 2$ is measured in channel confinement.

1.6 Interactions between swimmers

When a microswimmer moves through a viscous fluid, it induces a flow field surrounding itself. Therefore, it is expected that if several microswimmers are moving in

proximity to one another, they might interact hydrodynamically. These interactions can lead to emergent collective effects. For instance, dense bacterial suspensions exhibit intermittent formation of swirls and jets with length scales much larger than that of a single bacterium [45, 46]. Even for smaller number of cells, hydrodynamic interactions are thought to play an important role. For instance, the spermatozoa of wood mice, opposums, and fishflies are seen to experience a favourable interaction (in terms of propulsion speed and efficiency) when swimming nearby neighbours [47–49]. In particular, the fishfly sperm have been observed to exhibit in-phase beating of their flagella, a phenomenon termed "phase-locking" [49]. Phase-locking has also been experimentally studied by holding two flagellated cells at controlled separations using micropipettes [50]. In fact, in his 1951 paper, Taylor also studies two sheets swimming parallel to one another, and finds that in-phase swimming leads to the smallest amount of energy dissipation [25]. In addition, if the two sheets are swimming out of phase initially, viscous stresses tend to force the swimmers to be in phase over time. The same result has been found computationally in a later study including higher amplitude swimming [51]. Moreover, hydrodynamic interactions are thought to play a role in the bundling of bacterial flagella; a phenomenon which is important for bacterial locomotion [6, 52].

The larger organism *C. elegans* is also seen to experience collective motion when swimming in thin liquid layers due to a combination of steric and surface tension forces [53]. In addition, phase-locking has been observed for the nematode when placed in a confined fluid space [54]. However, in this case, steric interactions between the nematodes were deemed more important than hydrodynamic interactions. Studying the collective motion between these nematodes served as the motivation for Paper III. However, rather than finding evidence for collective motion when held adjacent to one another, the worms are seen to tangle. This tangling behaviour is investigated in detail in Paper III.

1.7 *Caenorhabditis elegans*

C. elegans (Fig. 1.5) is a millimeter sized, transparent nematode, which is considered to be one of the most well understood multicellular organisms [55, 56]. Interestingly,

Figure 1.5: An optical microscopy image of an adult *C. elegans*, roughly 1 mm long and 60 μm in diameter. The head of the worm is in the lower left corner. The scale bar represents 100 μm.

C. elegans was the first multicellular organism to have its entire genome sequenced. In fact, this simple worm has served as a model organism in biology for several decades. In part, this is due to its simple anatomy. It contains roughly 1000 cells, and lacks a respiratory and circulatory system [55, 56]. During its lifetime, it progresses through several life stages, each with a well defined body length, from L1 ($\sim$250 μm) to L2 ($\sim$380 μm), L3 ($\sim$500 μm), L4 ($\sim$640 μm), young adult ($\sim$900 μm), and finally adult ($\sim$1100 μm) [57]. On the other hand, it is one of the simplest organisms which has a nervous system (consisting of approximately 300 neurons). For this reason, it is often employed as the subject of studies researching neurological behaviour, functions, and development. In recent years, the worm has also become a popular subject of biophysical research. Some studies focus on determining the material properties of the worm [58, 59]. However, the larger effort from biophysicists has been on studying the undulatory locomotion of *C. elegans*.

1.7.1 The undulatory locomotion of *C. elegans*

C. elegans is long and slender, and well suited for implementing undulatory propulsion. Amazingly, this simple organism is able to propel itself through a wide variety

of environments. Its native environment is thought to be moist soil, and as such, the organism has been studied while swimming in mono- and polydisperse wet granular media [60, 61]. However, the worm is also able to move on the surface of (and within) agar [62], and swim through viscoleastic fluids and fluids with polymer networks [63,64]. In addition, *C. elegans* has been studied while swimming in structured environments, in which there is a pattern of regularly spaced pillars [65,66]. Finally, the worm can also swim through a simple liquid buffer, called M9 [55,67,68]. To learn about the fundamental hydrodynamics involved in this undulator's motion, placing it in M9 is the simplest starting point.

In a buffer, *C. elegans* swims with a reproducible waveform. Its typical propulsion speed is $U \sim 0.3$ mm/s, and its undulation parameters are roughly $f \sim 2$ Hz, $\lambda \sim$ 1-2 mm, and amplitude of approximately 0.25 mm [62, 67–69]. Thus, one can calculate the Reynolds number of the adult worm given Eq. 1.15, with $L \sim 1$ mm, $V \sim 0.3$ mm/s, $\mu \sim 1$ mPa·s and $\rho \sim 1000$ kg/m^3 (since the buffer has a similar viscosity and density as water), giving Re ~ 0.3. The smaller worms have lower values of Re. Still, we see here that young adult and adult worms are not firmly in the low Reynolds number regime, and inertial forces may not be entirely negligible. However, in one study, it was found that the flow field around the worm is consistent with predictions made by low Re theories [67]. Despite this, RFT is used in studies of *C. elegans* without proper justification of its applicability at this high of a Reynolds number [62, 67, 68]. The ideal way to verify RFT's applicability would be to perform direct force measurements which can be compared to the predictions made by the theory.

1.7.2 Force measurements on *C. elegans*

Although scarce, there have been some force measurements on the undulating nematode. In two separate studies, arrays of force sensing pillars were constructed for the worms to move in between while on agar [70, 71]. In one of these studies, the pillars were made of an elastic material, and could deflect when subjected to a force [70]. By using some elastic theory, the authors could calculate a theoretical force-deflection relationship for the pillars. Thus, by observing the displacements of the pillars as the worms pushed against them while moving through the agar, the authors could

compute forces. In the other study, the pillars were connected to strain gauges [71]. From the output of the strain gauges, the forces required to deflect the pillars were calculated. Both of these experiments found the forces involved to be on the order of micronewtons. However, in both of these studies, the worm is crawling atop a gel, and not swimming in a liquid. Therefore, these experiments have measured contact pushing forces of *C. elegans* while moving on a gel surface, rather than hydrodynamic, or viscous, forces involved in swimming.

Another study undertook a more indirect approach towards measuring the hydrodynamic forces of the worm swimming in a buffer. In this study, the flow fields surrounding the worm were visualized using particle tracking and velocimetry techniques [67]. Using this flow field, the authors could integrate the fluid stresses around the worm's body, to compute the viscous forces acting on the worm. In this way, lateral and propulsive forces of the worm were attained. The typical viscous forces were estimated to be on the order of nanonewtons. However, the flow fields were only visualized in the plane of swimming of the worm, and as such, contributions from viscous stresses acting on the upper and lower surfaces of the worm were neglected. In the same study, kinematic properties of the swimming worm were measured, and subsequently, Eq. 1.26 was used to estimate the value of K to be 1.4.

To estimate the theoretical predictions of c_N and c_T for *C. elegans*, we can use $\lambda \sim 1$ mm, $\Lambda \sim 1.2$ mm, and $r_c = r_w \sim 30$ μm for an adult worm, where r_w is the radius of the worm. Then, Gray and Hancock's coefficients (Eq. 1.25) are $c_N \sim 3.4$ and $c_T \sim 1.7$ ($K = 2$), and Lighthills coefficients (Eq. 1.27) are $c_N \sim 5.1$ and $c_T \sim 3.2$ ($K \sim 1.6$). However, as mentioned previously, RFT has not been verified for a Reynolds number this high. If verified, experimental measurements are necessary to test the theoretical drag coefficient predictions. Testing RFT for *C. elegans* and extracting the nematode's drag coefficients is the purpose of Paper I.

1.7.3 The gait modulation of *C. elegans*

The motion of *C. elegans* atop agar is qualitatively different from that in a buffer [62]. In particular, the two forms of motion appear so different that they are given different names: *C. elegans* crawls on agar and swims in a buffer. Crawling is associated with undulations of smaller wavelength, frequency, and amplitude [62,67–69,72]. However,

several experiments have shown that *C. elegans* is able to continuously modulate its gait, or type of motion, from swimming to crawling, and that the modulation occurs in response to increasing environmental resistance [62, 67, 68, 72]. In practice, the environmental resistance on the worm has been increased by raising the viscosity of the buffer (by several orders of magnitude) [67, 68], and by pressing the worm down onto a gel surface using a glass plate [72]. The gait modulation is adaptive, because maintaining the same frequency and amplitude of undulations over orders of magnitude increases in resistance would demand an enormous power output of the worm.

Chapter 2

Experimental Details and Data Analysis

In the following description of experimental details and data analysis, I will limit my discussion to the two studies in which I have been the primary author (Paper I and Paper II). The majority of the methods for Paper III are similar to that being described in this section, although more detail can be found in the supplementary information of that paper.

2.1 Micropipette deflection

Micropipette deflection is a technique that is perfectly suited for measuring forces in the range of μN- nN, and for objects of size μm-mm [59, 73, 74]. In this regime, force measurements are difficult to attain using other popular instruments, such as Atomic Force Microscopes. The technique involves a very thin glass capillary ($\sim$ 1000 times longer than it is thin), which, due to its high aspect ratio, is very flexible. Therefore, if a force is applied to the end of the capillary (or micropipette), it will deflect. For small deformations, the micropipettes are hookean. Thus, if the micropipettes are calibrated such that their spring constants are known, forces can be measured by multiplying the measured deflections with the spring constant.

Furthermore, the micropipettes are hollow, and by connecting a syringe to one end, suction can be applied through the opening of the pipette. Therefore, it is possible to

capture and hold on to appropriately sized object. If the object somehow experiences a force while being held, this will cause the micropipette to deflect, thereby allowing the force to be determined.

During an experiment, a pipette is observed under an optical microscope, so that μm deflections can be detected. The deflections are analyzed using an in-house cross-correlation script in MATLAB. Using an interpolation scheme within the cross-correlation script, sub-pixel deflections can be measured.

2.1.1 Micropipette fabrication

Micropipettes are made by stretching glass capillary tubes with an inner diameter of 0.7 mm and an outer diameter of 1 mm (World Precision Instruments Inc., item 1B100-6) with a pipette puller (Narishige PN-30) over a hot filament. Once pulled, the micropipettes are extremely thin (outer diameter of ~ 20 μm and inner diameter of ~ 10 μm), long (2-4 cm) and flexible. However, these thin pipettes have ends that tend to be jagged, which is undesirable for holding worms. To get a clean cut, the ends of the micropipettes must first be coiled around a hot (enough to soften the glass but not melt it) platinum iridium wire, whose temperature is controlled by a DC power supply. Subsequently, the power supply is rapidly turned off, causing the wire and coiled pipette tip to cool. As the glass pipette cools, it contracts, and is subject to large internal stresses. These stresses finally cause the coiled portion of the pipette to snap off, leaving behind the long, straight, and thin portion of the micropipette, with a straight cut at its end. While viewed under a microscope, these straight micropipettes are then bent into a desired configuration using a small hand-held tool over a hot platinum iridium wire. Two types of pipettes were used in Paper I and Paper II. One of these is a straight pipette with no bends. Such a pipette can only be measured to deflect side-to-side, and as such, can only measure forces along one direction. The other pipette is straight, but at its end contains a a small L-shaped bend in the plane normal to the straight portion, as seen in Fig. 2.1. If such a pipette is observed from below (as seen in the schematic), deflections in two perpendicular directions can be observed. Thus, two orthogonal forces can simultaneously be measured by observing the displacements of each side of the L-shape. The L-shaped bend is very rigid compared to the long straight portion, which is the only part that deflects

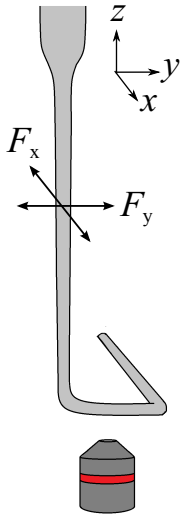

Figure 2.1: A schematic of a pipette with an L-shaped bend at its end, being observed from below with a microscope. By observing the L-shaped bend, deflections in the x- and y-directions can be measured independently, allowing perpendicular forces F_{x} and F_{y} to be measured simultaneously. The straight portion is roughly 3 cm long, while each bend is approximately 300-600 μm in length.

considerably. Each side of the L-shape is roughly 300-600 μm long and the straight part of the pipette is typically $\sim$ 3 cm long. If a pipette is too short, its spring constants will be higher than what is desired for most worm experiments. If a pipette is too long, the spring constant will be very small, and its opening will be narrow, making it difficult to attain an adequate suction force.

2.1.2 Micropipette calibration

To calibrate a micropipette, it is first connected to a syringe at the thick opening, and subsequently filled with water. The pipette is then held horizontally using an xyz-translation stage over a microscope stage, as seen in Fig. 2.2(a). To calibrate a pipette with an L-shaped bend, the pipette is oriented such that the tip faces downward. A mirror tilted at 45° is placed in front of the L-shape, and a light source is placed on the other side of the L-shape. The pipette is then positioned close to the mirror. In this configuration, one can place the microscope objective so that it focuses on the mirror image of the L-shape, rather than on the L-shape itself. Using this scheme, the view in the microscope is equivalent to viewing the system along the y-axis, in

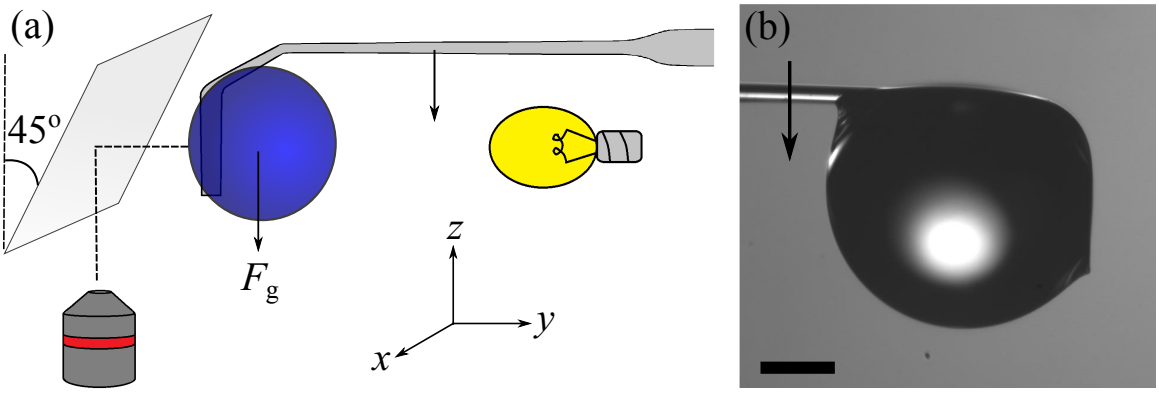

Figure 2.2: (a) A schematic illustrating the calibration of a pipette with an L-shaped bend at its end. The gray rectangle represents the mirror, which allows the system to be viewed along the y-axis. The light bulb represents the light source, and is positioned on the opposite side of the droplet as the mirror. The weight of the droplet causes the flexible portion of the pipette to deflect downwards. (b) An image of the L-shaped bend with a water droplet. As pressure is applied at the syringe, the water droplet grows, causing the L-shaped bend to move downwards. The scale bar represents 100 μm.

Fig. 2.2(a).

Sufficient pressure is then applied to the syringe to create a droplet of water at the end of the pipette (Figs. 2.2(a) and 2.2(b)). The added weight of the droplet causes a downwards (negative z-direction) deflection of the flexible portion of the pipette (Fig. 2.2(a)), which in turn causes the L-shaped bend to move downwards in the field of view (Fig. 2.2(b)). Images are snapped regularly as the droplet is filled with more water and the pipette continues to deflect in response (Figs. 2.3(a) and 2.3(b) show this deflection for a straight pipette). The deflections are subsequently analyzed using the aforementioned cross-correlation script to evaluate the displacement of the horizontal portion of the L-shape, as seen in Fig. 2.2(b). The images of the droplet are processed using another in-house code, which detects the circumference of the droplet, fits the shape to an ellipsoid, and extracts the volume of water from the ellipsoidal fit. The weight of the droplet, and hence the force on the pipette, can then simply be found by multiplying the volume with the density of water and the gravitational constant. As seen in Fig. 2.3(c), plotting the droplet weight as a function deflection (Δd) yields a linear relationship with slope equal to the pipette's spring constant, k_b.

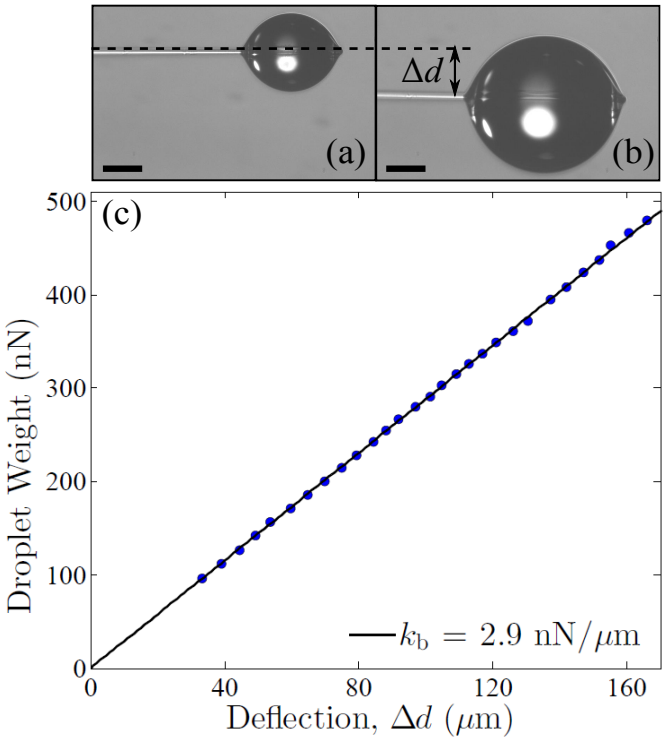

Figure 2.3: An example of the calibration of a straight pipette. Image of a straight pipette with a (a) small and (b) large droplet. The deflection (Δd) of the pipette between the two images is labelled. The scale bars represent 100 μm. (c) A plot of droplet weight as a function of deflection. The slope of the line is equal to the spring constant of the pipette. The micropipette is hookean over the entire force range covered in the calibration.

This procedure is repeated several times to find a mean value for k_b. A 10% error is typically assigned in the calibration which accounts for variability in k_b between trials, as well as other potential sources of error.

The procedure for calibrating a straight pipette is exactly analogous to the above procedure. In this case, the mirror is placed parallel to the end of the straight portion of the pipette (to view the system along the x-axis) and the light source is once again positioned on the opposite side of the droplet.

2.2 Worm handling

2.2.1 Maintenance of worm cultures

To begin our stock of *C. elegans*, wild-type worms (N2) were obtained from the Caenorhabditis Genetics Center. The worm populations have henceforth been grown on Escherichia coli OP50 NGM plates at 20 °C in an incubator (Thermo Scientific, Heratherm Inc 18). Worms can be kept on a single plate without dying for several months, as they enter an inactive state (Dauer) when food is scarce. However, to ensure that active and healthy worms are present on the NGM plates, it is necessary to regularly transfer worms to fresh plates in a process termed "chunking". To chunk, a tool is sterilized using an ethanol burner, and is then used to cut out a roughly 1 cm x 1 cm square of agar from a *C. elegans* populated plate. Next, the piece of agar is placed onto a new plate which has been stored in a refrigerator prior to chunking. The worms present in the transferred chunk of agar move into the rest of the fresh plate, which contains an abundance food. As those worms reproduce, a new population will grow that covers the plate. To have a large selection of healthy worms for an experiment, plates should be chunked 2-3 days prior. When not in use, the sides of the NGM plates are wrapped in parafilm to avoid mould contamination. For the same reason, the interior of the incubator should be cleaned with ethanol monthly.

2.2.2 Picking worms

To collect worms for an experiment, a Pasteur pipette with a thin metal wire attached to its end is used as a picker. The agar plate containing worms is placed underneath a microscope, and the wire picker is sterilized using an ethanol burner. While observing through the ocular, a desirable worm is located. Worms should be seemingly healthy, undulating through the agar, and of the desired size for the experiment in question. Next, the picker is brought down towards the agar. With a very gentle scooping motion, the worms can be picked up, as they tend to adhere to the wire. If the picker is handled too vigorously, the worm may be injured or even killed. Once the worm has been picked up, the picker is quickly dipped into an M9 buffer. In doing so, the worm is transferred into the M9, where it is able to survive for roughly 2-3 hours. The picker is once again sterilized, and the above procedure is repeated until a sufficient number

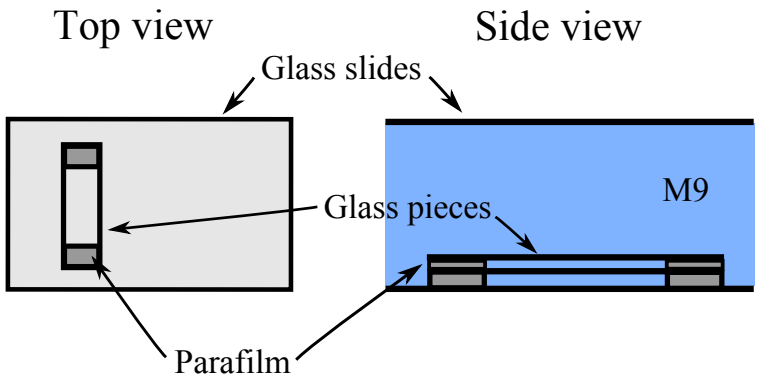

Figure 2.4: Top and side view of the chamber with an internal thin channel (neither schematic drawn to scale). Melted parafilm is used to afix the channel to the lower surface of the chamber. A chosen number of melted Parafilm layers are used to space the channel. In this case, the channel is spaced by a single stretched layer of Parafilm. The rubber spacers and clips which hold the entire chamber together are not shown.

of worms have been transferred into the M9. In a typical experiment, a selection of 20 worms is appropriate.

2.3 Experimental setup

2.3.1 Types of chambers

Two types of chambers were used in Paper I and Paper II. The first chamber consists of a hollow cylinder (cut from tubing) glued upright onto a thick glass microscope slide. The cylinder is clear and approximately 1 cm in diameter. The cylinder is filled with M9 in which the worms are placed. In this chamber, a pipette with an L-shaped bend (Fig. 2.1) is used and enters the chamber from above, such that the L-shape is in a plane parallel to the bottom glass surface.

The second chamber contains a thin channel that is mounted within it, as seen in Fig. 2.4. The chamber is constructed as follows. A thin glass slide ($\sim$ 150 μm thickness) forms the bottom surface of the chamber. Next, small rectangular pieces are cut out of other thin glass slides, and will form the upper and lower surfaces of the internal channel. The bottom surface of the channel is affixed to the glass slide (or the bottom surface of the chamber) by placing strips of parafilm between the

rectangular piece and the slide at either end, and subsequently melting the Parafilm by placing the slide on a heating stage at 90 °C. Next, the upper surface of the channel is mounted atop the now affixed lower surface. This is once again done by placing layers of Parafilm between the ends of the pieces, and then placing the chamber on the heating stage. A single sheet of Parafilm is ~ 100 μm thick. Thus, channel heights can be modified by choosing the number of layers of Parafilm to space the channel, as well as stretching the sheets of Parafilm, which can decrease their thickness to ~ 60 μm. For instance, in Fig. 2.4, the channel is spaced by a single stretched sheet of Parafilm, and is thus roughly ~ 60 μm. Now the internal channel of desired spacing has been constructed atop the lower glass surface of the chamber. At this point, a droplet of M9 is placed on the glass surface, and worms are picked and transferred into the sessile droplet. The chamber is then completed by placing rubber spacers ($\sim$ 3 mm thick) on the lower glass slide beside the droplet, laying a second glass slide on top, and using two small clips to hold the chamber together. The entirety of the chamber is filled with the M9 buffer, which remains held within the chamber due to surface tension. For this chamber, a straight pipette is inserted from the side of the chamber, such that it can enter the internal channel as well.

In both chambers, the pipettes are inserted deep enough that their flexible portions are completely immersed in the fluid. This precautionary measure is taken to prevent capillary forces at the buffer meniscus from disturbing the force measurements.

2.3.2 Catching worms and performing experiments

In the buffer-filled chambers, the worms are seen to swim nearby, and in the same plane as, the bottom glass surface. The pipette is moved using a translation stage until it is within the field of view. Then, the microscope stage is translated to position the pipette close to the tail of a swimming worm. Once sufficiently close, suction is applied through a syringe to capture a swimming worm by its tail. Worms are never sucked in by more than 15% of their total length. Upon capture, worms perform a reproducible sequence of swimming motions. The majority of the swimming is in the plane of focus, which is parallel to the bottom surface, as worms are caught whilst swimming in this plane. For experiments in both chambers, the system is observed from below with a microscope. Images of the swimming are snapped with a high-

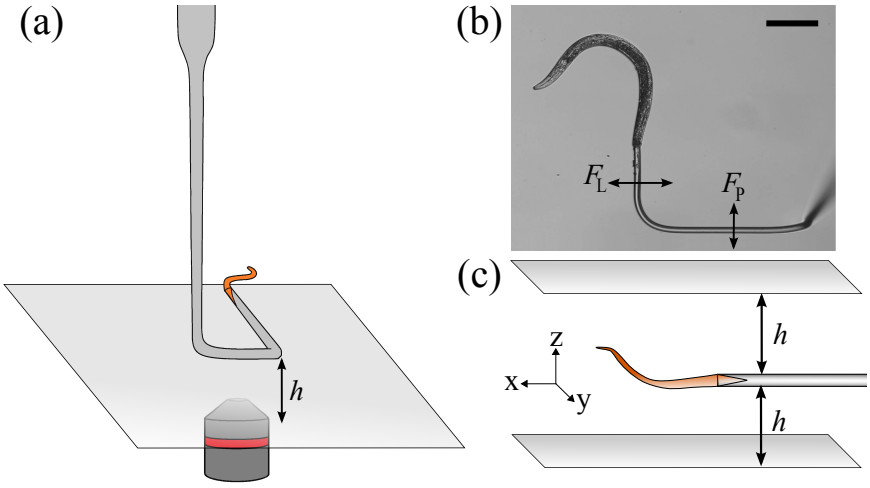

Figure 2.5: (a) Experimental setup for a pipette with an L-shaped bend. In this geometry, forces can be measured at controlled distances (or infinitely far away from) a single planar boundary. (b) An image taken of a young adult worm being held by the tip of a pipette with an L-shaped bend. By observing the motion of the L-shape, both lateral and propulsive forces can be measured. The scale bar represents 200 μm. (c) Experimental setup for a straight pipette holding a worm in the internal channel of a chamber. In this geometry, lateral forces are measured when the worm is swimming in the $x-y$ plane, at a distance h from either surface.

speed camera (Allied Vision Technologies, Model: GT1660) at 56 fps. Any data in which the worms are swimming out of plane, and hence move in and out of focus, are discarded.

As the worm swims, it experiences viscous forces parallel to its swimming axis, called propulsive forces F_{P}, but also generates forces perpendicular to this axis, called lateral forces F_{L}. If a worm is held by the tip of a pipette that contains an L-shaped bend, as seen in Fig. 2.5(a), the long flexible portion is free to deflect in both lateral and propulsive directions. Therefore, in observing the L-shaped bend from below (Fig. 2.5(b)), F_{L} and F_{P} can be measured simultaneously by measuring the motion of the L-shape in either direction. In Paper I, a pipette with an L-shaped bend is used, and the forces are measured as the distance from the boundary (h) is essentially infinite ($h/r_{\mathrm{w}} > 100$). In Paper II, the distance h is monitored and adjusted using a digital actuator. The distance can be precisely measured by moving the pipette until it is seen to be in contact with the bottom surface, and then raising it while

tracking the change in height using the actuator. Forces can not only be measured at controlled distances from a single planar boundary (Fig. 2.5(a)), but also midway in between two planar boundaries (Fig. 2.5(b)). The chamber with an internal channel is used to study the latter geometry. In such an experiment, worms are captured from anywhere within the chamber, and subsequently, the pipette and worm are positioned within the thin internal channel as shown in Fig. 2.5(c). In this confining geometry, one is restricted to use a straight pipette which can only be used to measure the lateral forces acting on the worm.

2.4 Data analysis

As mentioned previously, an in-house cross correlation script is used to precisely measure pipette deflections. To attain the zero force (or equilibrium) position of the pipette deflections, we wait for the worm to perform an Ω-turn. These are events in which the worm curls up into a ball and remains in that position for some time (on the order of a second). Since there is very little movement during this time, the viscous forces acting on the worm are small. Therefore, the pipette's position at this point in time allows us to determine the position of zero deflection. Releasing the worm may also be used to find the zero position when a straight pipette is used.

In order to attain kinematic information regarding the worm's swimming, and be able to apply RFT, it is necessary to perform some processing on the worm's body within each image.

2.4.1 Image processing of the worm's body

The image processing is done using a code I have written in MATLAB. The first step of the image processing is to threshold the image of the worm (Fig. 2.6(a)) into a binary (black or white) image. The threshold intensity is set manually and depends on the light intensity and contrast of the particular experiment. In the binary image, the worm is black on a white background (Fig. 2.6(b)). Next, a series of binary morphological operations on the thresholded image are performed. These operations include inverting the colour scheme so that the worm is white, filling in any holes in the worm, and dilating the worm to smooth out edges. The modified binary image

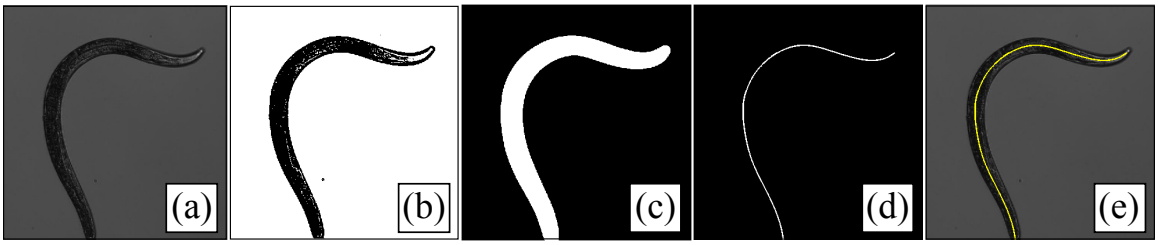

Figure 2.6: (a) Original image of the worm (b) Thesholded binary image (c) Modified binary image after numerous morphological operations (d) Centerline curve of the worm (e) Centerline curve (yellow) superimposed on the original image.

(Fig. 2.6(c)) is then thinned out so that a one pixel thick curve representing the worm's centerline remains. This centerline curve is parametrized by the x- and y-positions of the pixels. The x and y parametrizations of the centerline are independently smoothed and interpolated using spline fits, such that 1000 points are finally used to represent the centerline of the worm's body (Fig. 2.6(d)). 1000 points are chosen as this number of data points reasonably represents the worm's centerline to within our experimental resolution. Furthermore, increasing the number of points implies longer computational times for future calculations. As seen in Fig. 2.6(e), the resultant curve well approximates the centerline of the worm's body. From the centerline, it is straightforward to calculate various quantities of interest, such as the curvature and arclength of the worm.

2.4.2 Applying RFT

Since the 1000 points forming the worm's centerline are known at each point in time that an image is taken, it is possible to calculate the velocity of each of these points over time. To calculate the velocity of a body point in a frame, the position of the point in the previous frame is subtracted from the position of the point in the subsequent frame, and then the difference in position is divided by the total time between those frames. By comparing the direction of the velocity of a point with the orientation of the body at the same point, it is possible to deconstruct the velocity into a component tangential (v_{T}) and normal (v_{N}) to the body. Note that at this juncture, it is not yet possible to calculate any forces because c_{N} and c_{T} are

not known. However, since they are constant along the entire worm, we can leave these factors out of the calculation until the end. Thus, drawing from Eq. 1.21, the quantities

$$\mathrm{d}\tilde{F}_{\mathrm{T}} = -v_{\mathrm{T}}\mu\ \mathrm{d}l,\ \mathrm{d}\tilde{F}_{\mathrm{N}} = -v_{\mathrm{N}}\mu\ \mathrm{d}l. \tag{2.1}$$

are calculated for every point, where $\mathrm{d}\tilde{F}$ denotes the force on the segment less the factor of the drag coefficient, and $\mathrm{d}l$ is equal to the spacing between points (one thousandth of the worm's arclength) . Next, each of these forces are further decomposed into components along the lateral ($\mathrm{d}\tilde{F}_{\mathrm{T,L}}$ and $\mathrm{d}\tilde{F}_{\mathrm{N,L}}$) and propulsive ($\mathrm{d}\tilde{F}_{\mathrm{T,P}}$ and $\mathrm{d}\tilde{F}_{\mathrm{N,P}}$) directions. These force contributions from all segments are summed together, such that $\tilde{F}_{\mathrm{T,L}}$, $\tilde{F}_{\mathrm{N,L}}$, $\tilde{F}_{\mathrm{T,P}}$, and $\tilde{F}_{\mathrm{N,P}}$ are all known over time. Therefore, the RFT predictions of the lateral and propulsive forces are

$$F_{\mathrm{L}} = c_{\mathrm{T}}\tilde{F}_{\mathrm{T,L}} + c_{\mathrm{N}}\tilde{F}_{\mathrm{N,L}},\ F_{\mathrm{P}} = c_{\mathrm{T}}\tilde{F}_{\mathrm{T,P}} + c_{\mathrm{N}}\tilde{F}_{\mathrm{N,P}}. \tag{2.2}$$

Since F_{L} and F_{P} are known from pipette deflections, the RFT predictions for these forces can be simultaneously fit to the data, while treating the drag coefficients as free parameters. An additional free parameter is employed which allows for a small horizontal time shift between the RFT and measured force curves. Such a phase shift can, for instance, be caused by damping of the force transducer, inertial effects of the worm, and various imaging artifacts. These phase shifts are always smaller than $T/20$, where T is the period of the worm's motion. Note, in Paper I, $K = c_{\mathrm{N}}/c_{\mathrm{T}}$ was fixed at 1.5 to reduce the number of free parameters. In Paper II, in the section in which a straight pipette was used, RFT fits were only performed on the lateral force data.

Chapter 3

Featured papers

We present a micropipette deflecton technique for directly studying the hydrodynamic forces involved in the swimming of *C. elegans* as well as for investigating the tangling of two adjacent worms. Using suction, we catch worms by their tails such that their tails serve as fixed nodes during swimming. The hydrodynamic forces generated by the worms during swimming cause the micropipette to deflect. Using calibrated micropipettes of known spring constant makes it possible to compute forces from deflections. Paper I encompasses the first description of our experiment and the first directly measured hydrodynamic forces of *C. elegans* swimming. In this study, the success of Resistive Force Theory in capturing our force curves is demonstrated, thereby evidencing its applicability at a Reynolds number as high as ~ 0.1 . Paper II involves a similar experimental set up, but in these experiments, the effects of nearby solid boundaries are investigated. This study comprises the first force measurements on microswimmers with the inclusion of boundary effects. Resistive Force Theory is applied to determine how the worms' drag coefficients depend on the distance from a boundary. In addition, this paper quantifies a gait modulation that the worms undergo upon being subjected to high confinements. Paper III focuses on the tangling between two worms that occurs when they are held adjacent to one another. Although no forces are measured in this work, the deflections of the pipettes are used to identify and count tangling events. Simple theoretical models are applied to describe the observed tangling behaviour.

3.1 Paper I

Dynamic force patterns of an undulatory microswimmer

R.D. Schulman, M. Backholm, W.S. Ryu and K. Dalnoki-Veress, Phys. Rev. E, **89**, 050701(R) (2014).

In this work, we perform direct force measurements of *C. elegans* swimming in a buffer. Using a micropipette with an L-shaped bend at its end, we catch worms at different life stages by their tail. As the worms swim, they experience lateral and propulsive viscous forces, which are simultaneously measured. We find that the lateral and propulsive force curves are reproducible over time as well as between worms.

By performing image analysis on our high speed image sequences of the swimming worm, we extract data describing the position and velocity of its centerline over time. Using this data, we are able to apply the equations of RFT. Letting the drag coefficients be free parameters (but fixing their ratio at $K = 1.5$), we fit the RFT curves to our experimental data. In doing so, we witness an excellent agreement between RFT and our data, thereby demonstrating the success of RFT even at a Reynolds number this high ($\mathrm{Re} \sim 0.1$) . From our fits, we extract the drag coefficients of the worm, which are in agreement with the predictions of Lighthill (Eq. 1.27) within experimental error [28].

Assuming that the swimming of the worms of various sizes is self-similar (a good assumption), a scaling argument shows that the rms lateral force and mean propulsive force should scale as L_{out}^2, where L_{out} is the worm length found outside of the pipette. This scaling argument captures the rms lateral force data, but deviates from the mean propulsive force data at small worm sizes. In particular, the small worms generate smaller mean propulsive forces than expected, which is attributed to the small worms performing more "hooklike" motions that violate the self-similarity assumption.

In this study, the experiment was designed in collaboration with Matilda Backholm and Kari Dalnoki-Veress. I conducted the experiments and performed all data analysis. The image analysis script for the worm's body was written by me. I composed the drafts of the manuscript, which were in turn edited by Matilda Backholm, Kari Dalnoki-Veress, and William Ryu.

PHYSICAL REVIEW E **89**, 050701(R) (2014)

Dynamic force patterns of an undulatory microswimmer

Rafael D. Schulman,[1] Matilda Backholm,[1] William S. Ryu,[2] and Kari Dalnoki-Veress[1,3,*]

[1]*Department of Physics and Astronomy and The Brockhouse Institute for Materials Research, McMaster University, 1280 Main Street West, Hamilton, Ontario, Canada L8S 4M1*

[2]*Department of Physics, University of Toronto, 60 St. George Street, Toronto, Ontario, Canada M5S 1A7*

[3]*Laboratoire de Physico-Chimie Théorique, UMR CNRS Gulliver 7083, ESPCI, Paris, France*

(Received 23 January 2014; published 30 May 2014)

We probe the viscous forces involved in the undulatory swimming of the model organism *C. elegans*. Using micropipette deflection, we attain direct measurements of lateral and propulsive forces produced in response to the motion of the worm. We observe excellent agreement of the results with resistive force theory, through which we determine the drag coefficients of this organism. The drag coefficients are in accordance with theoretical predictions. Using a simple scaling argument, we obtain a relationship between the size of the worm and the forces that we measure, which well describes our data.

DOI: 10.1103/PhysRevE.89.050701 PACS number(s): 87.19.ru, 47.63.Gd, 47.15.G−

Locomotion through a fluid environment is common to organisms over a wide range of length scales, from whales and humans to primitive algae and bacteria. However, the physics of "microswimming," which is the propulsion at very small length scales, differs vastly from that applicable to macroscopic swimmers. Studying the principles of locomotion in this regime is crucial for our fundamental understanding of a diverse collection of organisms, including bacteria, sperm, and a variety of other microorganisms. Furthermore, microswimmers offer a wide variety of applications including robotic microswimmers capable of cargo towing for biomedical purposes, such as advanced drug targeting [1,2], collective swimming of bacteria to induce mixing in microfluidic devices [3,4], and fluid pumping [5–7].

The Reynolds number is a quantity that measures the relative magnitude of viscous and inertial forces in a fluid. At small length scales, the Reynolds number is typically less than unity, which implies that viscous forces are dominant and inertia can be neglected. In addition, to achieve propulsion in this regime, it is obligatory to perform a motion that is not time reversible, according to the scallop theorem [8]. This theorem asserts that if a swimmer performs a sequence of motions that is unchanged when played in reverse, such as a scallop, which simply opens and closes, it will not acquire any net displacement. There are numerous ways of breaking this symmetry, such as the helical beating of a flagellum [8–10], and motions similar to a human breast stroke, as is performed by the simple alga cell *Chlamydomonas reinhardtii* [11,12]. Another common way to break this symmetry is to propagate traveling waves down a body, which is successfully achieved by undulatory swimmers [13–16].

Undulatory locomotion is known to be a very efficient mechanism of propulsion and is effective over a large range of length scales [17]. Extensive theoretical efforts have been put forth in understanding the locomotion of a slender undulator, in which the length of the swimmer is much larger than its width [10,15,16,18,19]. Among these, resistive force theory (RFT) is a simple model in which the viscous force on a body segment moving through a low Reynolds number fluid can be decomposed into a component tangential and normal to that segment [10,15,16,18,20]. Each of these components is linearly proportional to the speed of the segment in that direction and related through the normal and tangential drag coefficients, c_N and c_T. The ratio c_N/c_T has important implications in the propulsion of the swimmer. Namely, if $c_N/c_T > 1$, propulsion is directed contrary to the direction of the traveling wave. If $c_N/c_T < 1$, we are faced with the curious case of the undulator moving in the same direction as its traveling wave, while the swimmer can attain no net propulsion if $c_N/c_T = 1$. In RFT, the difficulty lies in determining the drag coefficients. Several theoretical studies have derived

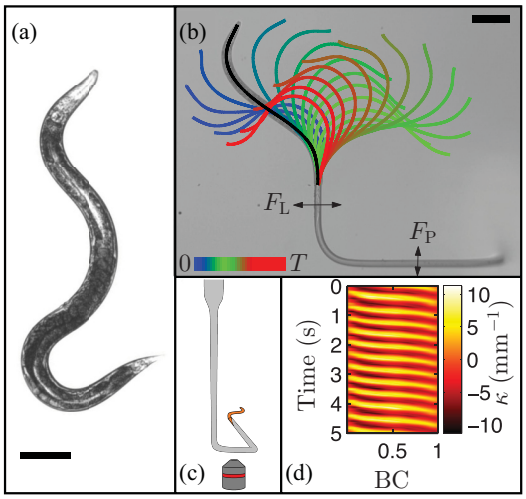

FIG. 1. (Color online) (a) *C. elegans*. The scale bar represents 100 μm. (b) Time lapse of the worm's centerline over one period (T), with colors representing time. A sample centerline is overlaid on the worm in black. Arrows indicate motion of the end of the pipette as a result of the two orthogonal forces. The scale bar represents 150 μm. (c) Schematic of the micropipette used in our experiments with a worm held at the end (not to scale). (d) Curvature color plot for the swimming. BC (body coordinate) denotes the distance along the worm, where 0 represents the head and 1 represents the portion of the worm nearest the pipette. Positive curvatures are indicated by lighter color and denote the convex side to the left.

*dalnoki@mcmaster.ca

values for the coefficients; however, assumptions regarding the swimming and approximations must be made [10,15,18,20]. Indeed, experimental measurements are crucial in order to evaluate the validity of RFT and to determine the magnitude of the drag coefficients. There have been experiments which have evaluated RFT for a variety of single-celled organisms using kinematic data from high-speed imaging [21–23]. Other experiments have performed average force measurements of nonundulatory microorganisms in optical traps [24,25]. However, to date, direct and time-resolved measurements of drag forces on an undulating microswimmer are still lacking. Furthermore, direct verification of the applicability of RFT for swimmers at length scales where the Reynolds number may not be much less than unity is still needed.

Many experiments on undulatory microswimmers have focused on the model organism *Caenorhabditis elegans* [Fig. 1(a)], a millimeter sized hermaphroditic nematode [26]. These studies have characterized the kinematics of *C. elegans* in various environments, including swimming in a buffer of various viscosities [27,28], viscoelastic media [29], crawling on agar [30], structured environments [31,32], and through complex environments such as granular materials [33,34]. Attempts have been made to measure crawling forces using pillars as force transducers for *C. elegans* crawling on agar [35,36]. In another work, the viscous forces of swimming *C. elegans* were inferred from particle tracking and particle image velocimetry [28]. However, these studies, though insightful, have not succeeded in performing direct measurements of forces and drag coefficients in fluid.

Here we present a method to directly measure the time-varying propulsive and lateral forces of *C. elegans*. A comparison between our experimentally determined forces and the calculated forces from RFT demonstrates an excellent agreement. The experimental and theoretical force curves are used to deduce values for the drag coefficients of *C. elegans* swimming. Finally, a simple scaling argument is presented which postulates a relationship between the size of the worm and the mean propulsive and rms lateral force. We find our experimental data to be well described by the scaling argument.

We use a micropipette deflection technique to measure the forces generated by the undulatory microswimmer [37–39]. In this technique, a flexible glass micropipette that is more than three orders of magnitude thinner than its length deflects when subjected to an external force. Since the bending stiffness of the pipette has been determined through calibration, forces can be computed from deflections of the pipette. We catch worms by their tail end by applying suction, and hold them with the end of our pipettes. The micropipettes are capable of deflecting along the worm's swimming axis, as well as along the corresponding in-plane perpendicular direction. Thus, we can measure forces in two orthogonal directions [Figs. 1(b) and 1(c)] [39]. As the nematodes move, they generate forces in their propulsive and lateral directions, which we independently measure using the micropipette as a force transducer [Fig. 1(c)]. The deflections of the pipette are much smaller than length scales associated with the motion of the worms [39].

Upon capture, the worms perform a highly reproducible and periodic sequence of body movements, in which traveling waves are propagated down the body, which is akin to free swimming of *C. elegans* [Fig. 1(b)] [27,28]. However, when held fixed at one end, the traveling waves are of larger amplitude than in free swimming and have a node at the fixed end. The temporal oscillations of the curvature of the worm exhibit a well defined frequency, which remains constant at 2.4 ± 0.2 Hz for worms of various lengths [Fig. 1(d)]. The spatial and temporal oscillations in the curvature compare well with what has been measured for free swimming [27,28,31].

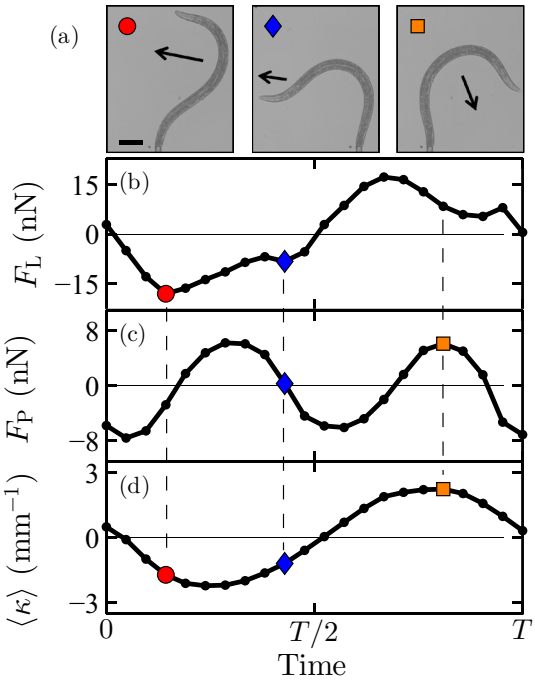

FIG. 2. (Color online) (a) Snapshots of a young adult worm at different stages of one swimming cycle. The labels refer to the markers in the graphs below and the arrows indicate the main velocity of the body. The scale bar represents 100 μm. (b) The lateral force experienced by the worm over one period, where a positive force denotes a force directed to the left. The peak negative force (red circle) corresponds to the worm moving directly left, generating a drag force to the right (negative direction). Secondary peaks (blue diamond) correspond to turning points in the swimming cycle, when an extra push in the lateral direction is instigated. This point roughly coincides with a zero in the propulsive force. (c) The propulsive force on the worm over one period, where a positive force denotes a force directed up (in the swimming direction). The maximum propulsive force (orange square) corresponds to the worm pushing fluid behind itself, generating a drag force forward. This point roughly coincides with a maximum in the curvature. (d) The mean curvature of the worm over one period.

Figure 2 shows direct *simultaneous measurements* of the force generated in the lateral and propulsive directions as well as images of the motion that caused specific forces [39]. Microswimmers inhabit a low Reynolds number environment, and as such, the net forces involved in swimming are dominated by viscous drag forces. The estimated Reynolds numbers for the worms in these experiment lie within the range 0.05–0.5 [39]. Thus, we are in a regime where inertial effects may not be negligible. However, it is known from previous work that *C. elegans* swimming in a buffer can indeed be treated as a

low Reynolds number swimmer, which suggests that viscous effects may dominate in our system [28]. Using this reasoning, the peak lateral forces (F_L) occur when the worm is moving with the greatest speed in the lateral direction [Fig. 2(b)]. Conversely, the largest propulsive forces (F_P) are generated when the worms push the greatest amount of fluid behind themselves [Fig. 2(c)]. Small secondary peaks can be found in the lateral force curve corresponding to turning points in the worm's cycle, in which the lateral motion experiences a small spike, and there is minimal motion in the propulsive direction. The maximum propulsive forces approximately coincide with the points of highest mean worm curvature $\langle\kappa\rangle$ [Fig. 2(d)].

In the low Reynolds number regime, drag forces are simply linearly proportional to velocities. According to RFT, one can deconstruct the drag force (dF) acting on each length segment (dl) of a slender body into forces in two orthogonal directions,

$$dF_T = -c_T v_T \mu\, dl, \quad dF_N = -c_N v_N \mu\, dl, \tag{1}$$

where μ and v denote the dynamic viscosity and speed respectively, c is the drag coefficient per unit length, and T and N denote directions tangential and normal to the length segment [15]. Since a slender body has little variation in thickness, c_N and c_T can be approximated as constants over the entire length of the swimmer. Although an experimental measurement of these two drag coefficients individually for this microscopic undulator is still needed, the ratio c_N/c_T has been determined through theory and experiment to be approximately 1.5 for body and swimming parameters characteristic of *C. elegans* [10,16,28]. If c_N and c_T are known, using this prescription, and given the speed of each segment of the undulator's body, it is possible to calculate the total drag force the swimmer experiences. Since our experiment is performed in conjunction with high-speed imaging, we can extract the velocities of the worm body. Using numerical integration, we generate the RFT prediction for the lateral and propulsive force curves. Subsequently, using two free parameters, we fit the RFT prediction of the two force curves to our lateral and propulsive data (Fig. 3). In our analysis, we fix c_N/c_T at 1.5 because our fits are not sensitive enough given the experimental error in the data to accurately determine this ratio. Thus, the first free parameter in our fitting controls the magnitude of the two drag coefficients, and functions as a vertical stretch on the curves. We find these drag coefficients to vary little for worms of all sizes ranging from ∼400 to ∼1200 μm (this agrees with the theoretical prediction of a weak logarithmic dependence on geometry, in which there is no dependence if the swimmer is self-similar for all sizes [10,15,18]), and measure $c_N = 5.1 \pm 0.3$, and $c_T = 3.4 \pm 0.2$. We have thus made an experimental quantification of the magnitude of the drag coefficients for *C. elegans* swimming in a fluid.

The second fitting parameter allows for a small horizontal time shift in the data. A phase shift is to be expected for several reasons, including damping of the force transducer, inertial effects of the worm, and imaging artifacts such as overexposure in the body's direction of travel. The observed phase shifts were always smaller than $T/20$, with T the period of the motion. Deviations between data and theory may be attributed to various sources of error [39].

Although other studies have generated predictions of the forces and powers involved in undulatory microswimming at larger length scales, they are reliant on theoretical models, including RFT [27,28]. The close agreement between the predictions of RFT and our experimental data demonstrates the applicability of this model in generating quantitative predictions in undulatory systems (Fig. 3). For the purposes of comparing our measured drag coefficients with theoretical predictions by Lighthill [10], we can use 1.0 ± 0.2 mm as an estimated wavelength, and 45 ± 5 μm as the typical thickness of a young adult. Substituting these parameters into Lighthill's expressions, we get $c_N = 4.9 \pm 0.4$, and $c_T = 3.0 \pm 0.3$, which fall within the error of our experimental values.

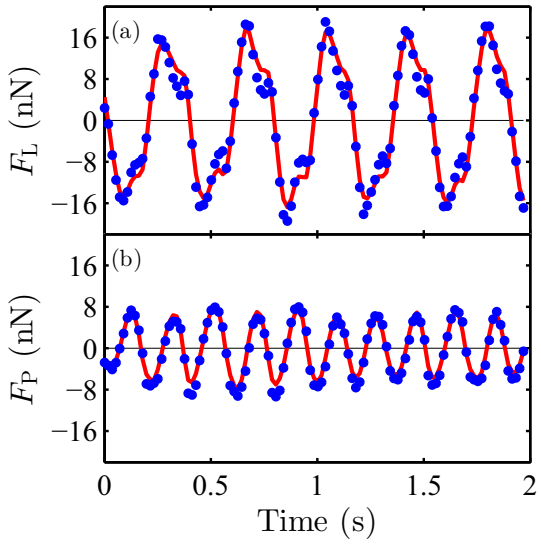

FIG. 3. (Color online) (a) The lateral and (b) propulsive force plotted as a function of time over several periods. The blue circular markers denote the experimental data which contain a systematic error of roughly 10% from uncertainty in the spring constant of the micropipette. The red solid curve represents the prediction from RFT which has been fit to the data. The error in the RFT curve is estimated to be 5%.

Slender body theory (SBT) is a more general model of microswimming, on which the simpler RFT is based [40]. SBT is expected to generate accurate predictions over a wider range of swimming parameters than RFT. However, since RFT captures our data within experimental error, it follows that it is in also in agreement with SBT [39].

Using simple scaling arguments, one can determine the dependence of the magnitudes of typical propulsive and lateral forces upon the worm size. In our experiments, we find that the drag coefficients are largely independent of the size of the worm. Thus, once the forces in Eq. (1) have been integrated over the worm's body, the forces will scale as $F \propto vL_{out}$, where v is a typical speed and L_{out} is the length of the worm outside of the pipette. The typical speed depends on the product of the amplitude (A) of the oscillations and the frequency (f) of the swimming. Therefore, the forces will scale as $F \propto AfL_{out}$. We make the approximation that the swimming of the worm is self-similar for all life stages, which implies that A will scale linearly with L_{out}. This assumption is influenced by previous measurements which showed that mechanical properties of the

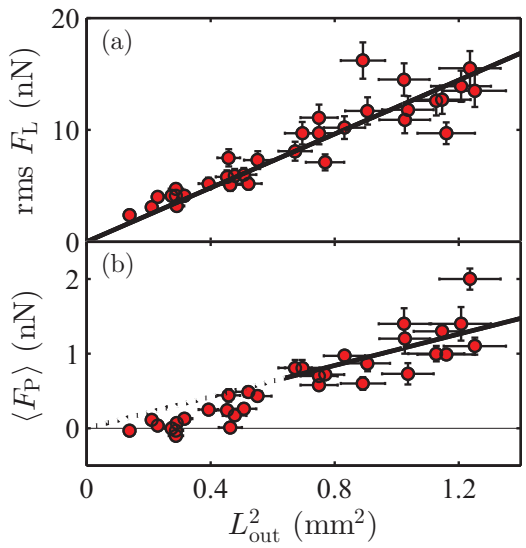

FIG. 4. (Color online) (a) The root-mean-squared lateral force and (b) the mean propulsive force as a function of the square worm length outside of the pipette. The mean and rms are taken over many cycles.

worms can be treated as self-similar [38]. In our experiments, we find that f does not depend on the worm size. Thus, we see that the typical viscous forces generated should scale as $F \propto L^2_{out}$. A plot of the root-mean-squared (rms) lateral force as a function of L^2_{out} yields approximately a straight line passing through the origin, in accordance with the scaling argument [Fig. 4(a)]. Since the worms are attempting to swim forward, one would expect there to be no net force in the lateral direction over one period. Indeed, for the worms, we measure a mean lateral force of 0.1 ± 0.7 nN. Consistent with the scaling argument we find that the mean propulsive force $\langle F_P \rangle$ also scales with L^2_{out} at large worm lengths [Fig. 4(b)]. However, at small worm lengths ($\lesssim$800 μm), the mean force drops. We attribute this to the fact that small worms undergo motions that are quite different from traveling waves and more "hooklike." This type of motion does not yield appreciable propulsion. The mean propulsive forces of larger worms we measure here are comparable to other estimates for *C. elegans* [28].

Here we report a direct measurement of the forces experienced by an undulatory microswimmer. Using micropipette deflection, we attain a high-resolution time sequence of drag forces felt by *C. elegans* while swimming in a buffer. By using these force measurements in conjunction with the low Reynolds number model resistive force theory, we demonstrate the success of this simple model in describing the locomotion of slender microswimmers. This direct verification of the theory, which has previously been assumed to apply at this Reynolds number, provides a better understanding of undulatory microswimming at length scales larger than of unicellular organisms. Furthermore, using RFT to describe our data, we extract measured values of drag coefficients for *C. elegans*, a highly studied model organism and microswimmer. These coefficients are in congruence with theoretical values, and will allow future studies to perform direct calculations of the forces generated by free swimmers simply by using high-speed imaging. Finally, simple scaling arguments successfully explain how the magnitude of lateral and propulsive forces scale with the size of the swimmer.

The financial support by Natural Science and Engineering Research Council of Canada is gratefully acknowledged.

[1] N. Darnton, L. Turner, K. Breuer, and H. Berg, Biophys. J. **86**, 1863 (2004).
[2] D. Weibel, P. Garstecki, D. Ryan, W. Diluzio, M. Mayer, J. Seto, and G. Whitesides, Proc. Natl. Acad. Sci. USA **102**, 11963 (2005).
[3] M. Kim and K. Breuer, Phys. Fluids **16**, L78 (2004).
[4] M. J. Kim and K. S. Breuer, Anal. Chem. **79**, 955 (2007).
[5] Y. W. Kim and R. R. Netz, Phys. Rev. Lett. **96**, 158101 (2006).
[6] M. J. Kim and K. S. Breuer, Small **4**, 111 (2008).
[7] E. Lauga and T. R. Powers, Rep. Prog. Phys. **72**, 096601 (2009).
[8] E. Purcell, Am. J. Phys. **45**, 3 (1977).
[9] M. Silverman and M. Simon, Nature (London) **249**, 73 (1974).
[10] J. Lighthill, SIAM Rev. **18**, 161 (1976).
[11] U. Ruffer and W. Nultsch, Cell Motil. **5**, 251 (1985).
[12] M. Polin, I. Tuval, K. Drescher, J. P. Gollub, and R. E. Goldstein, Science **325**, 487 (2009).
[13] G. Taylor, Proc. R. Soc. London, Ser. A **209**, 447 (1951).
[14] J. Gray, Q. J. Microsc. Sci. **94**, 551 (1953).
[15] J. Gray and G. Hancock, J. Exp. Biol. **32**, 802 (1955).
[16] J. Gray and H. W. Lissmann, J. Exp. Biol. **41**, 135 (1964).
[17] G. Tokic and D. K. P. Yue, Proc. R. Soc. B **279**, 3065 (2012).
[18] R. Cox, J. Fluid Mech. **44**, 791 (1970).
[19] R. S. Berman, O. Kenneth, J. Sznitman, and A. M. Leshansky, New J. Phys. **15**, 075022 (2013).
[20] G. Hancock, Proc. R. Soc. London, Ser. A **217**, 96 (1953).
[21] B. Friedrich, I. Riedel-Kruse, J. Howard, and F. Jülicher, J. Exp. Biol. **213**, 1226 (2010).
[22] K. Drescher, J. Dunkel, L. H. Cisneros, S. Ganguly, and R. E. Goldstein, Proc. Natl. Acad. Sci. USA **108**, 10940 (2011).
[23] N. C. Darnton, L. Turner, S. Rojevsky, and H. C. Berg, J. Bacteriol. **189**, 1756 (2007).
[24] R. P. McCord, J. N. Yukich, and K. K. Bernd, Cell Motil. Cytoskel. **61**, 137 (2005).
[25] S. Chattopadhyay, R. Moldovan, C. Yeung, and X. Wu, Proc. Natl. Acad. Sci. USA **103**, 13712 (2006).
[26] S. Brenner, Genetics **77**, 71 (1974).
[27] C. Fang-Yen, M. Wyart, J. Xie, R. Kawai, T. Kodger, S. Chen, Q. Wen, and A. D. Samuel, Proc. Natl. Acad. Sci. USA **107**, 20323 (2010).
[28] J. Sznitman, X. Shen, R. Sznitman, and P. E. Arratia, Phys. Fluids **22**, 121901 (2010).
[29] X. N. Shen and P. E. Arratia, Phys. Rev. Lett. **106**, 208101 (2011).
[30] X. N. Shen, J. Sznitman, P. Krajacic, T. Lamitina, and P. E. Arratia, Biophys. J. **102**, 2772 (2012).

[31] S. Park, H. Hwang, S.-W. Nam, F. Martinez, R. H. Austin, and W. S. Ryu, PLoS One **3**, e2550 (2008).

[32] T. Majmudar, E. E. Keaveny, J. Zhang, and M. J. Shelley, J. R. Soc. Interface **9**, 1809 (2012).

[33] G. Juarez, K. Lu, J. Sznitman, and P. Arratia, Europhys. Lett. **92**, 44002 (2010).

[34] S. Jung, Phys. Fluids **22**, 031903 (2010).

[35] A. Ghanbari, V. Nock, S. Johari, R. Blaikie, X. Chen, and W. Wang, J. Micromech. Microeng. **22**, 095009 (2012).

[36] J. C. Doll, N. Harjee, N. Klejwa, R. Kwon, S. M. Coulthard, B. Petzold, M. B. Goodman, and B. L. Pruitt, Lab Chip **9**, 1449 (2009).

[37] M.-J. Colbert, A. N. Ragen, C. Fradin, and K. Dalnoki-Veress, Eur. Phys. J. E **30**, 117 (2009).

[38] M. Backholm, W. S. Ryu, and K. Dalnoki-Veress, Proc. Natl. Acad. Sci. USA **110**, 4528 (2013).

[39] See Supplemental Material at http://link.aps.org/supplemental/10.1103/PhysRevE.89.050701 for experimental details, movies of the worm swimming and the forces produced, a calculation of the Reynolds number, and discussion of sources of error and slender body theory.

[40] B. Rodenborn, C.-H. Chen, H. L. Swinney, B. Liu, and H. Zhang, Proc. Natl. Acad. Sci. USA **110**, E338 (2013).

3.2 Paper II

Undulatory microswimming near solid boundaries

R.D. Schulman, M. Backholm, W.S. Ryu and K. Dalnoki-Veress, submitted to Physics of Fluids.

In this study, we investigate the effects of nearby solid boundaries on the viscous forces experienced by *C. elegans* swimming in a buffer. As discussed in Sec. 1.5 due to the nearby no-slip boundary condition in the fluid, the worm experiences larger viscous drag forces in proximity to a boundary. Once again using micropipette deflection, we study the forces at controlled distances from a single planar boundary, as well as two parallel planar boundaries (channel confinement).

Near a single solid boundary, the lateral and propulsive force curves appear vertically stretched compared to the corresponding force curves in an infinite fluid. In fact, the rms lateral forces and mean propulsive forces are approximately 2 to 3 times larger at the closest approaches to the single boundary than in the unbounded fluid. Using the same image analysis techniques as in Paper I, we successfully apply RFT to describe the forces produced in response to the swimming worms. However, in this work, we allow both c_{N} and c_{T} to be free parameters, thereby permitting us to extract both of these quantities independently. These drag coefficients decrease as a function of the distance away from the boundary, and compare well with the values determined in Paper I far from the boundary. We compare the drag coefficients with the predictions of Lighthill and Katz *et al.*, and find that the data is in agreement with the models in certain regimes [28, 40]. From our data, we find that $K = 1.5 \pm 0.1(5)$ at all distances from the single boundary.

In between two parallel solid boundaries, the forces experienced by the nematode increased substantially from the single boundary case. Once again, the drag coefficients are seen to decrease as the boundaries are placed further from the worm. In this geometry, we measure K to increase significantly as the worm is highly confined. In very wide channels, the worm swims in an effectively infinite fluid, and the drag coefficients measured are in agreement with Lighthill's predictions and the values determined in Paper I [28].

In high confinement, the worm is seen to modulate its gait. Included in this gait modulation is a large decrease in the swimming amplitude and a smaller decrease in the frequency. This modulation occurs as a response to the increased viscous forces present during confinement, and is analogous to that seen in studies in which the viscosity has been modified [67,68].

In this study, I designed and conducted the experiments, as well as all data analysis. I wrote the drafts of the manuscript, which were subject to editing by Matilda Backholm, Kari Dalnoki-Veress, and Wlliam Ryu.

Undulatory microswimming near solid boundaries

R. D. Schulman,[1] M. Backholm,[1] W. S. Ryu,[2] and K. Dalnoki-Veress[1, 3, a)]
[1)] *Department of Physics & Astronomy and the Brockhouse Institute for Materials Research, McMaster University, Hamilton, ON, L8S 4M1, Canada*
[2)] *Department of Physics and the Donnelly Centre, University of Toronto, Toronto, ON, M5S 1A7, Canada*
[3)] *Laboratoire de Physico-Chimie Théorique, UMR CNRS Gulliver 7083, ESPCI, Paris, France*

(Dated: 23 June 2014)

The hydrodynamic forces involved in the undulatory microswimming of the model organism *C. elegans* are studied in proximity to solid boundaries. Using a micropipette deflection technique, we attain direct and time-resolved force measurements of the viscous forces acting on the worm near a single planar boundary as well as confined between two planar boundaries. We observe a monotonic increase in the lateral and propulsive forces with increasing proximity to the solid interface. We determine normal and tangential drag coefficients for the worm, and find these to increase with confinement. The measured drag coefficients are compared to existing theoretical models. The ratio of normal to tangential drag coefficients is found to assume a constant value of $1.5 \pm 0.1(5)$ at all distances from a single boundary, but increases significantly as the worm is confined between two boundaries. In response to the increased drag due to confinement, we observe a gait modulation of the nematode, which is primarily characterized by a decrease in the swimming amplitude.

PACS numbers: 47.63.Gd, 47.15.G-, 87.19.ru
Keywords: Locomotion, Microswimming, *C. elegans*

I. INTRODUCTION

Locomotion through a fluid environment at small length scales, or "microswimming", is interesting because the relevant physics differs considerably from that applicable to macroscopic swimmers. Microorganisms dwell in a regime where viscous forces dominate and swimmers have negligible inertia[1]. That is, the Reynolds number (Re), which is a measure quantifying the ratio of inertial to viscous forces in a fluid, is typically much smaller than unity for microscopic swimmers. The activity within this field has increased substantially in recent years. This growth is, in part, due to rapidly improving experimental techniques capable of performing measurements of motile microorganisms, as well as more developed analytical and computational treatments of these systems. Beyond studies which have succeeded in providing precise kinematic observations of small swimmers, in the last decade, there have been direct force measurements of unicellular organisms using optical traps[2,3]. This large drive towards developing a better understanding of low Re locomotion is warranted, as it offers exciting application and research avenues, such as fluid pumping[4–6], collective motion of bacteria to generate mixing in microfluidic devices[7,8], and microscopic artificial swimmers capable of transporting loads for biomedical purposes such as advanced drug targeting and robotic surgery[9,10]. Furthermore, enhancing our ability to describe the relevant physics is a crucial step towards developing a more complete picture of the behaviours, capabilities, and interactions of bacteria, sperm, and other microorganisms.

There are numerous biologically relevant systems in which microorganisms move near a boundary, such as in surface-associated bacterial infections[11,12], sperm locomotion in the female reproductive tract[13], and biofilm formation[14,15]. To attain a complete picture of these systems, it is imperative to understand how the physics of a microswimmer differs upon proximity to an interface. However, microswimmers are typically studied whilst swimming in an effectively infinite fluid and few studies have investigated the effects of a nearby interface. In particular, due to the nearby no-slip boundary condition at a fluid-solid interface, there will be an increase in the shear of the velocity field near such a boundary. This increase in shear will cause an increase in viscous forces, which will influence the motility of organisms. Experiments have verified changes in both propulsion and trajectories of swimmers near solid boundaries at low Re[6,16–19].

A unique aspect of low Re locomotion is that, according to the Scallop Theorem, to achieve propulsion it is necessary to undergo a sequence of motions that is not time-reversible[1]. Microorganisms have developed various swimming mechanisms that satisfy this constraint, such as motions akin to a human breast stroke, as characterized by the alga cell *Chlamydomonas reinhardtii*[20,21], or the helical rotation of a bacterium's flagellum[1,22,23]. Undulatory locomotion, in which a swimmer propagates travelling waves down the length of its body, is another non-time-reversible mechanism, and is often employed by nematodes and sperm[24–27].

Undulatory locomotion has proved to be a highly efficient means of propulsion which is present over a length scales ranging from microns to tens of meters[28]. The locomotion of slender undulatory swimmers has been inves-

[a)] Electronic mail: dalnoki@mcmaster.ca

tigated by a multitude of theoretical studies[23,26,27,29,30]. A common approach is to derive resistance coefficients for the swimmer, such that given the velocity of the segments of the swimmer's body, it is possible to compute the force. Such a framework is called resistive force theory (RFT). In this model, one can decompose the force acting on each body segment into a component tangential and normal to the body, each of which is proportional to the speed of the segment along the corresponding direction, and related by the normal and tangential drag coefficients, c_{N} and c_{T}. In particular, the ratio $K = c_{\mathrm{N}}/c_{\mathrm{T}}$ is a quantity of interest, as it determines the magnitude and direction of propulsion of the swimmer. These drag coefficients have been derived for a slender undulator in an unbounded fluid[23,26] and for slender cylinders near boundaries[31,32]. In particular, the results of Katz *et al.* predict K=2 for a cylinder moving parallel to a nearby fluid-solid interface, and also predict K to increase past a value of 2 when the cylinder is confined between parallel solid plates[31]. Recently, the drag coefficients of an undulatory microswimmer in an infinite fluid were found using direct force measurements, and compared well with the theoretical result[33]. However, there have been no direct force or drag coefficient measurements for undulatory swimmers in proximity to a solid boundary, which is the focus of this study.

Experiments focusing on undulatory locomotion often employ the model organism *Caenorhabditis elegans*[34], a millimeter sized nematode, as its subject. The viscoelastic material properties of this worm have been determined[35], as well as its kinematic properties in a wide variety of media[36–44]. In addition, there has been much interest in the gait modulation of *C. elegans* from swimming to crawling, which involves a decrease in frequency and wavelength of undulatory motion[36–38]. The gait modulation is known to occur in response to changing environmental resistance, which has been realized in experiments by changing viscosity[36,37], and by pressing the worm down onto an agar surface with a glass plate[45]. Direct force measurements have been attained for *C. elegans* crawling on agar[46,47] and recently for *C. elegans* swimming in a buffer[33]. Although there have been some studies which have involved confining the worm[45,48], no experiments have measured swimming forces in proximity to an interface, nor have the kinematics been studied for confinement of the worm near solid boundaries. Despite this, many studies of free swimming *C. elegans* employ experimental designs in which the worm swims near a solid boundary, even though the effects of the boundary, in terms of changing drag coefficients and modulations in kinematics of the worm, are not properly understood. Studying the behaviour and forces experienced by *C. elegans* in confinement provides insight into the impact of the physical constraints that nematodes face in their true habitats (e.g. soils and other materials with small interstitial spaces).

In this paper, we perform direct force measurements using micropipette deflection[33,35,49,50] on the undulatory microswimmer and model organism *C. elegans* at controlled distances from a singe solid boundary and between two solid boundaries. The structure of the manuscript is as follows. In Sec. II we describe the experimental methods, including details of micropipette deflection and image analysis. In Sec. III A, we present measurements of forces and drag coefficients of the worm at varying distances from a single planar solid boundary, and compare these to existing theoretical models. In Sec. III B, we determine drag coefficients for the worm swimming midway between two planar solid boundaries with different spacings, and compare the measurements to theory. We discuss and present evidence of a gait modulation of the worm in response to increasing drag coefficients in confinement in Sec. III C. Finally, we provide a summary and conclusions in Sec. IV. We find that for increasing confinement, the drag coefficients and viscous forces generated by *C. elegans* increase monotonically. The drag coefficients are compared to theoretical models and exhibit partial agreement. We determine the drag coefficient ratio K, and find that it is constant at all distances from the single boundary, but find it to increase as the worm is confined between two boundaries. In addition, as the drag coefficients increase, the worm is seen to exhibit a gait modulation.

II. EXPERIMENTAL METHODS

A. Micropipette Deflection

As in previous work, we employ a micropipette deflection technique to measure time-resolved forces in dynamic, microscale systems[33,35,49,50]. In this experimental technique, a flexible glass micropipette that is more than three orders of magnitude thinner than it is long, deflects when subjected to an external force. Since the spring constant of the pipette has been determined through calibration, forces can be computed from measured pipette deflections[50]. In this study, two types of pipettes are employed. In the first part of the study, a straight pipette with an L-shaped bend at its end is used (Fig. 1(a)). The L-shaped bend, in which each length is about 300-600 μm, is highly rigid compared to the long straight portion of the pipette, which is roughly 3 cm long. For this reason, only the long straight portion exhibits appreciable deflection. Therefore, this micropipette is capable of deflecting in two perpendicular directions: along the worm's swimming axis, as well as along the corresponding in-plane perpendicular direction (Fig. 1(b)). Thus, using this pipette, we can measure both the propulsive and lateral hydrodynamic forces generated by the worm, by simply observing the L-shaped bend from below (the same approach has previously been employed[33]). In the second part of the study, a completely straight pipette which is roughly 3 cm long is used (Fig. 1(c)). Such a pipette can only deflect side-to-side, and can thus only measure the lateral forces generated by the worm. All pipettes

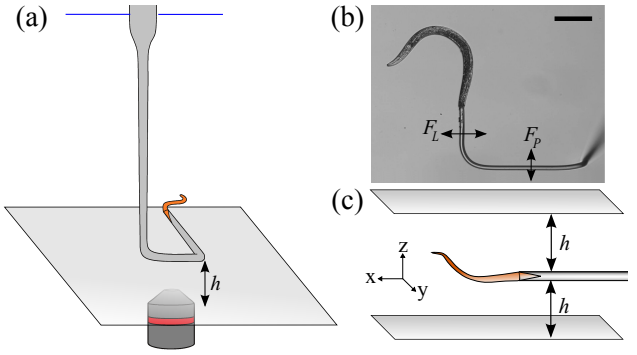

FIG. 1. (a) Experimental set up for the single boundary experiments. A straight pipette with an L-shaped bend at its end is used to measure forces of the worm swimming at a distance h from the boundary. The blue horizontal line represents the location of the buffer meniscus. (b) An image taken of a young adult worm swimming as it is being held with the L-shaped bend of a pipette. By observing the L-shaped bend move, we can measure both lateral ($F_{\rm L}$) and propulsive ($F_{\rm P}$) forces. The scalebar represents 200 μm. (c) Experimental set up for the channel confinement experiments. A straight pipette is used to measure lateral forces of the worm swimming in the x-y plane at a distance h from each boundary.

in this study have an outer diameter of ∼20 μm and an inner diameter of ∼10 μm. The spring constants of all pipettes are within the range of 2.7 - 8.9 nN/μm, with no more than 10% uncertainty in each spring constant. The deflections of the pipettes in these experiments are much smaller than length scales associated with swimming of the worms (i.e. pipettes can be treated as linear springs).

B. Experimental Design

In this study, force measurements are performed on L4, young adult, and adult worms. Wild-type worms (N2) were obtained from the Caenorhabditis Genetics Center and cultivated according to standard procedures[34]. The worms are picked off NGM plates and placed inside a chamber filled with M9 for the force measurements (see Fig. 1). Worms are captured by positioning the end of the micropipette in proximity to the worm's tail and applying suction through a syringe connected to the micropipette. Worms are never sucked in by more than 15% of their total length. Upon capture, the z-position of the pipette is adjusted and monitored using a digital actuator. The nematodes perform a highly reproducible undulatory motion when being held by the micropipettes. Worms are seen to swim in the plane of focus (parallel to the plane of the boundaries) during the majority of the experiments, as they are captured while swimming parallel to this plane. In each type of experiment, the system is observed from below with a microscope. Images of the swimming are taken with a high-speed camera (Allied Vision Technologies, Model: GT1660) at 56 fps. Data in which there is out of plane swimming results in a portion of the swimming cycle being out of focus – such data is discarded.

Worms are studied in two types of confinement: near a single planar boundary and inside a channel. For the single planar boundary experiment, a transparent cylindrical container is used[33]. In this case, the micropipette with the L-shaped bend is inserted into the chamber from above such that the thin flexible portion is fully immersed in the fluid, as seen in Fig. 1(a), where the horizontal line indicates the location of the buffer meniscus. By letting the thick stiff portion of the pipette pass through the meniscus, we prevent capillary forces at the contact line from disturbing the force measurements. The L-shaped bend is in a plane parallel to the bottom boundary. For the measurements, the worm is positioned to be at a desirable h away from the bottom boundary. The distance h is measured by moving the pipette until it is in contact with the bottom surface, and subsequently raising the pipette while keeping track of the relative change in height using the digital actuator.

For the channel confinement experiment, the channel is composed of two parallel glass slides spaced and held together by a chosen number of layers of melted Parafilm to achieve a desired channel height, $2h$ (Fig. 1(c)). The channel heights range from 58 μm to 1700 μm. This channel is mounted within a larger chamber filled with buffer in which the worms are placed, composed of two horizontal glass slides separated by rubber spacers. The buffer remains in the chamber due to surface tension. In these experiments, the straight pipette is inserted into the larger chamber from the side. For the measurements, the worm is captured from the larger chamber and positioned such that it is equidistant from the top and bottom plates of the internal channel, at a distance h from either plate. The flexible portion of the pipette is mainly in the larger chamber, and only a small portion at the end (containing the worm) is placed within the channel. Again, we ensure that the meniscus of the buffer is only in contact with the thicker portion of the pipette. The height of the channel $2h$ and the corresponding midpoint position are determined using the same technique as for the single boundary.

C. Image Analysis

The deflections of the micropipettes are analyzed using a cross-correlation technique, which, given the magnification of the microscope used in the experiment, is able to resolve deflections to a precision of ∼0.1 μm. This translates into a sub nN precision in our force measurements for the range of pipette spring constants used.

The nematode's motion during swimming is analyzed as follows. First, each snapshot of the swimming is thresholded into a binary image. Subsequently, each binary image is processed to attain a centerline of the worm's body. The raw data of each centerline is smoothed using a spline curve. From the resultant

smoothed centerline, it is possible to compute quantities such as the velocities of all points along the body (used for the RFT computations), body curvatures, and the amplitude of the swimming. All above analysis was done using inhouse code written in MATLAB. The worm's radius is measured near its vulva using ImageJ.

III. RESULTS AND DISCUSSION

A. Single Planar Boundary

1. Force measurements

At any distance from the boundary, lateral and propulsive force curves over a swimming cycle of the worm were obtained. The force curves were reproducible over time as well as from worm to worm. Examples of force curves for a single period of swimming at a distance close and far from the boundary are shown in Figs. 2(a) and 2(b). The Reynold's number of this system is in the range of 0.05-0.5[33], and previous studies have demonstrated that the physics describing the locomotion of *C. elegans* is compatible with that of a low Re swimmer[33,37]. For such low Re swimmers, the forces we measure are dominated by viscous forces[33]. As such, a maximum in the lateral force, for instance, roughly corresponds to the point in the worm's swimming cycle in which it moves with maximal velocity in the negative lateral direction (defined to be right in our experiments). Using the same logic, when the worm has a maximal velocity component in the negative propulsive direction, we measure a maximum force in the forwards swimming direction.

At close distances to the planar boundary, we observe significant increases in the forces generated by the worms. As seen in Figs. 2(a) and 2(b), the lateral and propulsive force curves are plotted as a function of time over one swimming period . Near the boundary, the force curves appear vertically stretched in comparison to the corresponding force curves of the same worm far from the boundary. At large distances from the planar boundary (roughly $h \sim 3000$ μm, or $h/r_w > 100$, where r_w is the radius of the worm), we observe the swimming of the worms to be similar in form and frequency as in previous work in an unbounded fluid[33]. Furthermore, at large distances, the magnitudes of the forces we measure compare well with past work. In Fig. 2(c), the normalized root-mean-square (rms) lateral force is plotted as a function of h/r_w. The rms lateral force increases continuously as the worms are brought closer to the boundary. The rms lateral force increases most significantly below $h/r_w \sim 10$, and at very close approaches to the boundary it can be more than 3 times larger than in an unbounded fluid. For the mean propulsive force, we measure $\langle F_P \rangle = 3 \pm 1$ nN at $h/r_w = 1.8 \pm 0.3$ for worms with $L_{out} = 880 \pm 60$ μm, where L_{out} is the length of the worm found outside of the pipette. In comparison, for worms of similar size in an unbounded fluid, $\langle F_P \rangle = 0.8 \pm 0.2$ nN[33]. Thus, in our experiments, the worms attain significantly larger mean propulsive forces when they swim near the boundary. Near the boundary, viscous drag forces are larger due to the nearby no-slip interface. Since the propulsion of microswimmers is derived from viscous forces, the propulsive forces are expected to increase near the solid boundary because of the increasing velocity gradient.

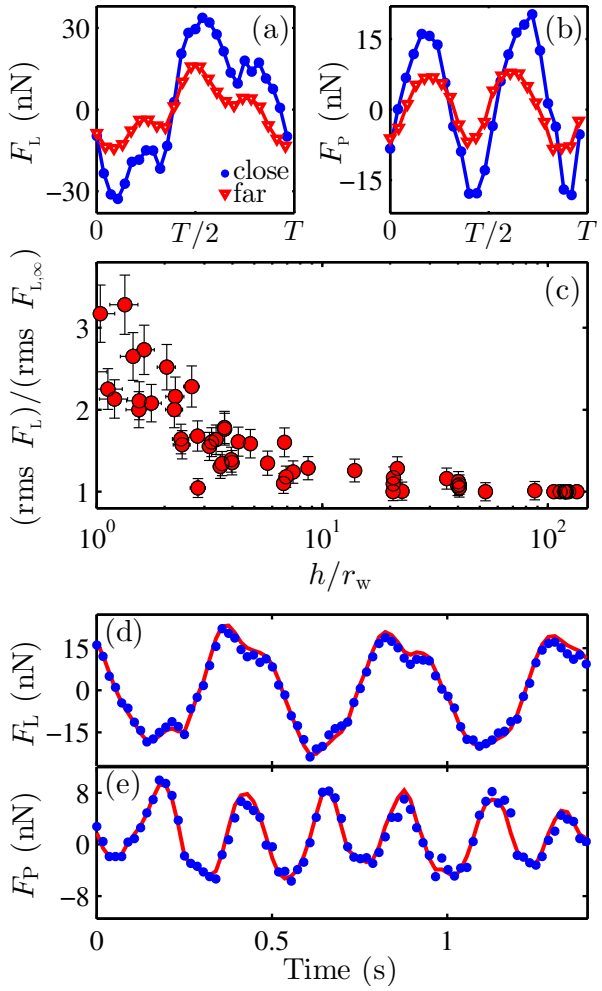

FIG. 2. The (a) lateral (F_L) and (b) propulsive (F_P) forces over one period of a young adult worm's swimming, close ($h = 35 \pm 4$ μm) and far ($h = 2524 \pm 4$ μm) from a single boundary. (c) The rms lateral force normalized to its value at infinity ($h/r_w > 100$) as a function of the distance to the boundary (h) normalized by the worm radius (r_w), for young adult worms. The vertical error bars come from uncertainties in the spring constant of the pipette and temporal variations of the forces. The horizontal error bars stem from uncertainties in determining the distance from the boundary and measuring the worm's radius. (a) Lateral and (b) propulsive forces (blue circle markers) for a young adult worm swimming near a single boundary ($h/r_w \sim 2.8$) plotted as a function of time over several periods. The solid red curves correspond to simultaneous RFT fits to the lateral and propulsive force data. In this case, $c_N = 7.8 \pm 1.2$ and $c_T = 5.1 \pm 0.8$.

2. Drag coefficients

For a swimmer moving through a fluid, the velocity of each infinitesimal segment of the swimmer's body can be decomposed into two perpendicular directions, a component tangential (v_{T}) and normal (v_{N}) to the body. In RFT, these velocities generate infinitesimal drag forces ($\mathrm{d}F$) on the corresponding body segment ($\mathrm{d}l$), which are given by

$$\mathrm{d}F_{\mathrm{T}} = -c_{\mathrm{T}} v_{\mathrm{T}} \mu \, \mathrm{d}l \quad \text{and} \quad \mathrm{d}F_{\mathrm{N}} = -c_{\mathrm{N}} v_{\mathrm{N}} \mu \, \mathrm{d}l, \qquad (1)$$

where μ is the dynamic viscosity, c represents the drag coefficient per unit length, and T and N denote directions tangential and normal to the body segment[26]. The ratio $c_{\mathrm{N}}/c_{\mathrm{T}}$ has been estimated through theoretical as well as experimental studies to be approximately 1.5 for *C. elegans* in an infinite fluid medium[23,27,37]. We previously measured these drag coefficients for *C. elegans* in an unbounded fluid to be $c_{\mathrm{N}} = 5.1 \pm 0.3$, and $c_{\mathrm{T}} = 3.4 \pm 0.2$, where the ratio of the drag coefficients, K, was fixed to be 1.5[33]. However, these coefficients have not been experimentally determined in the proximity to a boundary.

If c_{N} and c_{T} as well as the speed of each segment of the worm's body are known, one may integrate Eq. 1 to find the total viscous force acting on the undulator. From image analysis of our high speed image sequences attained during experiments, we can extract kinematic data, including body segment speeds, for the worm's swimming. Since c_{N} and c_{T} are not known in the presence of a solid boundary, we can treat these as free parameters, in calculating RFT's prediction of the lateral and propulsive forces. Using this procedure, we can fit the RFT force curves to the experimental force curves, and as such, extract best fit values for c_{N} and c_{T}. A third free parameter is employed in our fits which allows for a relative phase shift between the theoretical and experimental force curves. This horizontal time shift may be present for several reasons, including viscous damping of the micropipette, inertial effects of the worm, and various imaging artifacts. These phase shifts are always smaller than $T/20$, where T is the period of the worm's motion. Examples of RFT fits to lateral and propulsive force data for a young adult worm swimming near a boundary are shown in Figs. 2(d) and 2(e), where the data is plotted alongside the RFT prediction. As seen in these figures, the RFT fit describes the data within experimental error. In addition, as seen in Figs. 2(d) and 2(e), the experimental force curves are reproducible over time.

The fits are performed at several values of h/r_{w} for L4, young adult, and adult worms. The swimming of these worms is observed to be approximately self-similar, meaning that the swimming motions and waveforms all scale with the size of the worm. The resultant values of c_{N} and c_{T} are plotted as a function of h/r_{w} in Figs. 3(a) and 3(b). As demonstrated in these plots, the data collapses for a large range of values of h/r_{w}, since both h and r_{w} (~ 14 μm to ~ 35 μm) are varied, this suggests that this ratio is an important controlling parameter.

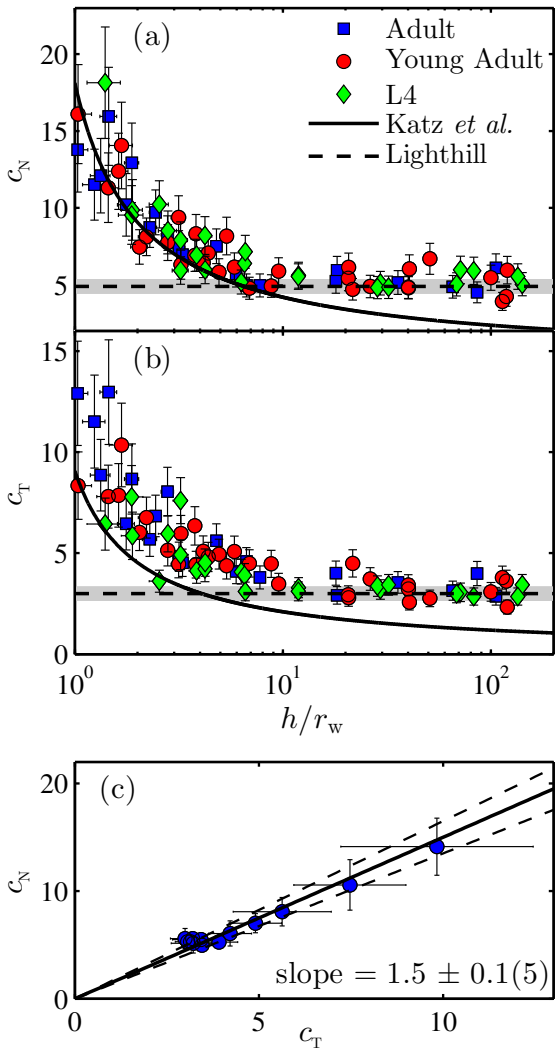

FIG. 3. (a) c_{N} and (b) c_{T} plotted against the normalized distance from the boundary for adult, young adult, and L4 worms. The vertical error bars come from uncertainty in the spring constant of the pipette and the fitting procedure. The solid and dashed curves correspond to the predictions of Katz *et al.* and Lighthill[23,31]. The grey area denotes the uncertainty range in evaluating Lighthill's drag coefficients. (c) Binned values of c_{N} and c_{T} from (a) and (b) respectively, demonstrating that a linear correlation (solid line) with a slope of 1.5 ± 0.1(5) describes the data within error. The dashed lines correspond to lines given by the upper and lower bounds of the slope. The error bars of the data points come from the scatter in the binning of (a) and (b).

Katz *et al.* incorporated the effects of a nearby solid planar boundary into the calculation of the drag coefficients for a straight cylinder[31]. Their values of c_{N} and c_{T}, which contain no free parameters, are plotted along with the data in Figs. 3(a) and 3(b), represented by the solid curves. In their analysis, the resultant resistance coefficients are derived in the regime $r_0 << h << l/2$, where r_0 and l are the radius and length of the cylinder re-

spectively. For a young adult worm in our experiments, $r_w \sim 24$ μm and $L_{out}/2 \sim 450$ μm. Evidently, there is no value of h which is much larger than the worm radius, and simultaneously much smaller than half the worm length. Thus, *C. elegans* falls outside of the ideal regime for which the derivation by Katz *et al.* is applicable. However, there are no studies which incorporate boundary effects into a calculation for the drag coefficients of an undulating cylinder. Thus, although limited in its applicability to our system, the study of Katz *et al.* provides the most relevant comparison near a boundary. Despite this, as seen in Fig. 3(a), their predictions describe the c_N data well for $h/r_w \lesssim 4$. On the other hand, one can see in Fig. 3(b) that there is a consistent underestimate of c_T compared to our measurements for all h/r_w. In the limit $h >> r_w$, the worm can be well approximated as swimming in an unbounded fluid, where the theoretical predictions of drag coefficients for an undulatory swimmer become applicable[23,26]. In this regime, the wavelength of the swimming is a more relevant length scale than the distance from the boundary, and the prediction of Katz *et al.*, which does not take into account the effects of undulations, is expected to fail. Since Lighthill's resistance coefficients have been shown to exhibit excellent agreement with experimental values in an unbounded fluid[23,33], we expect the data for c_N and c_T to match this theoretical prediction in the $h >> r_w$ regime. Indeed, as seen in Figs. 3(a) and 3(b), Lighthill's resistance coefficients, given by $c_N = 4.9 \pm 0.4$, and $c_T = 3.0 \pm 0.3$[23], represented by dashed lines, agree with the data for $h/r_w \gtrsim 10$. In generating this prediction, we have used parameters characteristic of young adult worms: 1.0 ± 0.2 mm as an estimated wavelength, and $r_w = 45 \pm 5$ μm, but since the swimming can be approximated as self-similar[33], the theoretical drag coefficients for adults and L4's are within error of the values above.

In Fig. 3(c), binned averaged values of c_N are plotted as a function of binned averaged values of c_T. The binning is performed evenly as a function of $\log_{10}(h/r_w)$ with bin sizes of 0.15, large enough to have sufficient data in each bin. An average value within each bin is subsequently computed. We see that this data is well represented by a single line of slope $K = 1.5 \pm 0.1(5)$. Thus, the ratio $K = c_N/c_T$ assumes a constant, distance-independent value of $1.5 \pm 0.1(5)$ for undulatory swimming in a plane parallel to a solid planar boundary. In the straight cylinder calculation of Katz *et al.*, a constant value of $K = 2$ is derived. Lighthill's calculation yields $K = 1.6 \pm 0.2$, which is in agreement with our experimental value for all h/r_w. Interestingly, theoretical and experimental estimates which have suggested that $K \sim 1.5$ have been carried out for an infinite fluid medium[23,27,37], yet our results imply that this ratio remains valid in the proximity of a solid planar boundary.

As a consistency check, it is worthwhile comparing to see that the increase in the magnitude of the forces we measure close to a boundary, scale with the increase in drag coefficients. Nearby the boundary ($h/r_w = 1.8 \pm 0.3$), where we found $\langle F_P \rangle = 3 \pm 1$ nN, c_N and c_T are both roughly 2.5 times larger than in an unbounded fluid, where $\langle F_P \rangle = 0.8 \pm 0.2$ nN[33]. The mean propulsive force and rms lateral forces should scale linearly with the magnitude of the drag coefficients. Thus, we would expect $\langle F_P \rangle$ near the boundary to be roughly 2.5 times larger than in an unbounded fluid, or $\langle F_P \rangle \sim 2$ nN, which agrees with the measured value within experimental error. Furthermore, the rms lateral force near the boundary is found to be 2.3 ± 0.2 times larger than in an unbounded fluid. This increase is roughly consistent with the 2.5 times increase in the drag coefficients.

B. Channel Confinement

For the studies of a worm confined between two solid boundaries (Fig. 1(c)), the confining geometry restricted us to a straight pipette and only lateral forces could be measured. Thus, our resistive force theory curves are, in this case, only fit to lateral force data[51]. In the same way as before, we can extract the values of c_N and c_T from our free fits. The results are shown as a function of h/r_w in Figs. 4(a) and 4(b) for adult, young adult, and L4 worms. For the smallest channel, the drag coefficients are more than an order of magnitude larger compared to in an unbounded fluid. Thus, we see that the effect of a second solid boundary, is not simply additive in terms of the increase in the drag coefficients experienced by the worm. Instead, the second boundary imposes a significant restriction on the fluid flow surrounding the worm's body compared to in the single boundary case, causing this large increase in viscous drag.

In their study, Katz *et al.* also investigate the case of parallel plate confinement of a straight cylinder moving in the central plane of the channel[31]. Once again, the derivation is carried out for a straight cylinder in the $r_0 << h << l/2$ limit, and is thus limited in its applicability to our system. Nevertheless, for comparison, this theoretical prediction for the drag coefficients, as well as Lighthill's results, are plotted alongside the data in Figs. 4(a) and 4(b). Here we see that the predictions of Katz *et al.* are in agreement with data near the intersection with Lighthill's drag coefficients. For larger h/r_w, Lighthill's results capture our data within error. For smaller h/r_w, the results of Katz *et al.* overestimate c_N and underestimate c_T. The failure is not a failure of the theory, rather it is to be expected since *C. elegans* falls outside of the regime in which the derivation of Katz *et al.* is carried out. Despite this, as mentioned previously, the study of Katz *et al.* provides the most relevant theoretical comparison of drag coefficients near a boundary.

The data of c_T contains more scatter than the data for c_N. We believe that this can in part be attributed to c_T being more influenced by changes in geometry of the experiment. The thin chambers that we use may not

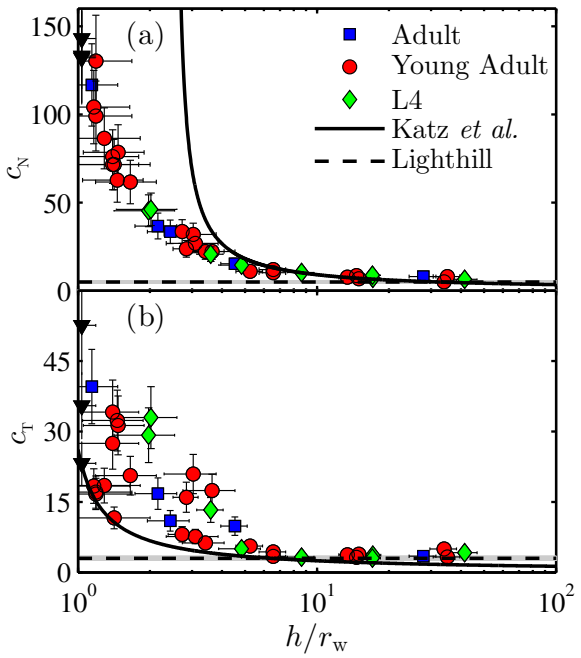

FIG. 4. (a) c_N and (b) c_T as a function of the normalized distance to each boundary in channel confinement for adult, young adult, and L4 worms. The predictions of Katz *et al.* and Lighthill are plotted as solid and dashed curves. The black triangle markers correspond to three measurements on the same worm at three separate y-positions (Fig. 1(c)). This translation affects c_T more significantly than c_N.

be perfectly parallel ($\pm$ 0.5°) and the swimming plane of the worm may also be subject to a tilt ($\pm$ 2°), such that the swimming of the worm is not exactly in plane with the chamber walls. Furthermore, there is an inherent error in determining the midpoint of the chamber ($\pm$ 2 μm) These sources of scatter would be more significant for experiments with higher confinement. To demonstrate the possibility of scatter due to uncertainties in geometry, we performed an experiment in which we placed the worm at the center of a very thin chamber, and measured the drag coefficients at three separate y-positions (Fig. 1(c)), each a few hundred microns apart. These three measurements are represented by the black triangle markers in Fig. 4. As seen in the figure, this procedure resulted in significant scatter in the value of c_T, yet relatively little scatter in the value of c_N, where two of the data points are so close that they are indistinguishable in the plot. Another source of scatter may stem from the RFT fitting. Since the final contribution of tangential body motion to the lateral force is smaller than the contribution from normal body motion, our fits will be more sensitive to determining c_N precisely.

Interestingly, the predictions of Katz *et al.* involve a monotonically increasing value of K upon increasing the confinement within the channel, in contrast with the case of the single boundary. In our experiments, we find that for very large channels (at $h/r_w = 35 \pm 6$), $K = 1.8 \pm 0.7$, which is in agreement with the results for an essentially unbounded fluid (i.e. far from the single plane boundary). On the other hand, for very narrow channels (at $h/r_w = 1.3 \pm 0.1$), we find $K = 5 \pm 2$. Thus, when confined between two plates there is an increase in K for highly confined worms, whereas we obtain a constant value of K for an undulatory swimmer near a single plane boundary.

C. Gait Modulation

For very wide channels, or at large distances from a single boundary, the same swimming is seen as for an unbounded fluid[33]. However, as the worm is placed into channels of high confinement, there is a significant difference in the swimming of the worm (see movies in the supplemental information[51]). Most noticeably, the amplitude of the motion is greatly reduced compared to that seen in an unbounded fluid. Time-lapses of the nematode's centerline over one period of motion are shown in Figs. 5(a) and 5(b), for $h/r_w = 28 \pm 4$ and $h/r_w = 1.1 \pm 0.3$. For the highly confined worm, the shape of the worm's body is more akin to a sinusoid about the swimming axis, and more similar to the free swimming waveform of *C. elegans*[36,37]. In Fig. 5(c), the lateral position of the head of the worm (x_{head}) is plotted as a function of time for the worm in low and high channel confinements, corresponding to Figs. 5(a) and 5(b). As seen, the amplitude of the worm's head motion is much larger when it is not confined (red open circle markers) compared to under high confinement (blue filled circle markers). In addition, the confined worm is seen to swim with a reduced frequency.

To quantify the change of amplitude discussed above, experienced by the worm as it modulates its gait, we measure the mean angular amplitude, A_θ, which is defined as half the angle swept out by the worm's head during swimming. As seen in Figs. 5(a) and 5(b), the angular amplitude is significantly smaller for the confined worm. Since it is known that *C. elegans* experiences a gait modulation in response to increasing environmental resistance (such as increasing viscosity), it is not surprising that the swimming form will change with increasing values of c_N and c_T. In our system, we quantify the amount of environmental resistance by the sum $c_N + c_T$, which increases by a factor of 20 from an unbounded fluid to the most confined worms studied (analogous to a 20-fold increase in viscosity from that of a buffer, as seen in Eq. 1). The angular amplitude is plotted as a function of $c_N + c_T$ in Fig. 5(d) for worms swimming in channel confinement as well as in the presence of a single boundary. The angular amplitude decreases as a function of $c_N + c_T$. This decrease is most rapid for $c_N + c_T \lesssim 30$. In addition, since the worm simply modulates its gait in response to changing resistance, the results for the single boundary and for the channel confinement fall on the same curve. Included in this gait modulation is a slight decrease in

the swimming frequency from 2.4 ± 0.2 Hz for an unbounded fluid[33], to 2.07 ± 0.13 Hz for $c_N + c_T = 108 \pm 9$.

The significant difference in swimming amplitude that we measure by confining the worm has not been seen over the same range of increasing environmental resistance in studies of gait modulation in which the fluid viscosity has been changed[36,37]. In these studies, the amplitude of free swimming worms was found to remain relatively constant over a 20-fold increase in the viscosity from that of a buffer. However, the fact that our worm is tethered at the tail is a crucial difference, and the swimming amplitude we measure in the unbounded buffer differs from that of a free swimming worm. Therefore, it is not surprising that some kinematic parameters, such as the amplitude, may exhibit different behaviours in the gait modulation of our system. Studies on gait modulation in *C. elegans* measure a decrease in the swimming frequency of roughly 10-20% from that in a buffer[36,37], which is consistent with our findings. In studying gait modulation by changing the viscosity, the chemical composition of the fluid is altered, which may have implications on the behaviour of the worm. In addition, the osmotic pressure of the solution is changed, which may upset the ionic balance of the nematode. Therefore, our results indicate that confinement near solid boundaries is another complimentary way in which gait modulation can be investigated without changing composition of the fluid.

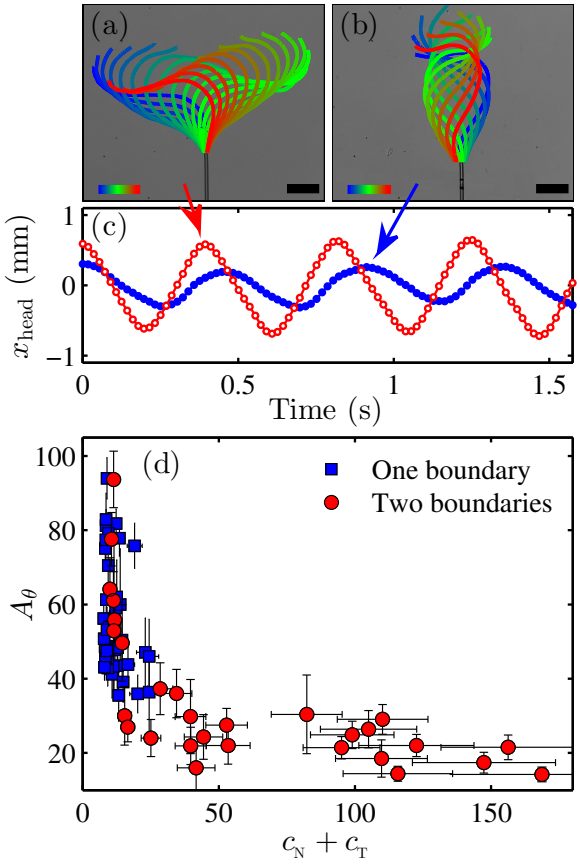

FIG. 5. Time-lapses of the worm's centerline over one swimming period for (a) very low ($h/r_w = 28 \pm 4$) and (b) very high ($h/r_w = 1.1 \pm 0.3$) confinement, in which only every other centerline in the image sequence is plotted. The colourbar indicates the temporal progression along the single period (from t=0 to t=T) and the scalebar represents 200 μm. (c) The lateral position of the head (x_{head}) of the worm in high and low channel confinement as a function of time for several swimming periods. The red open circles and the blue filled circles correspond to the worms in (a) and (b). (d) The angular amplitude as a function of $c_N + c_T$ for young adult and adult worms swimming near a single boundary (blue squares) and in channel confinement (red circles).

IV. SUMMARY AND CONCLUSIONS

In this study, we present an experimental investigation into drag forces acting on an undulatory microswimmer in proximity to solid boundaries. We employ micropipette deflection to directly measure the viscous forces during the swimming of the model organism *C. elegans* in a plane parallel to nearby boundaries. This represents the first direct force measurement of a microswimmer in which boundary effects have been investigated. We witness large increases in the lateral and propulsive forces of the worm as it approaches a single boundary. Using kinematic data from the high speed image sequences of the swimming in conjunction with our force measurements, we are able to extract the normal and tangential drag coefficients for the worm. The drag coefficients decrease as a function of the distance away from the solid boundary. Despite the study being limited in its applicability to our experimental system, the predictions of Katz *et al.* capture the general trends of c_N and c_T near the boundary, but with some deviations. Lighthill's results for c_N and c_T are successful at large separations from the boundary. We find $K = c_N/c_T = 1.5 \pm 0.1(5)$ at *all* distances from the boundary. This is an interesting result, as it suggests that a propulsive force increase of an undulator swimming in plane with a nearby boundary cannot be attributed to a changing ratio of the drag coefficients.

For confinement between two planar boundaries, the drag coefficients increase by a factor of 20 for the highest confinements compared to in an unbounded fluid, and we observe an increase in K for high confinements. In this geometry, Lighthill's results are still in agreement with our data for very large channels. Our results suggest that the analytical results for the drag coefficients in proximity to a boundary are not entirely suitable for this system, and require reconsideration by further theoretical studies. For both channel and single boundary geometries, as the drag coefficients increase, the nematode is seen to undergo a gait modulation characterized by a large decrease in the amplitude of its swimming. This gait modulation is independent of whether the worm is swimming

near one or two boundaries, and is only a function of the drag coefficients it is experiencing. These results offer a promising new means of investigating the gait modulation of *C. elegans* by confining the worm, rather than changing the viscosity and hence altering the chemical composition of the fluid.

ACKNOWLEDGMENTS

The financial support by Natural Science and Engineering Research Council of Canada is gratefully acknowledged. The authors also thank Alexandra Kasper for useful comments.

[1]E. M. Purcell, "Life at low Reynolds-number," Am. J. Phys. **45**, 3–11 (1977).
[2]R. P. McCord, J. N. Yukich, and K. K. Bernd, "Analysis of force generation during flagellar assembly through optical trapping of free-swimming *Chlamydomonas reinhardtii*," Cell Motil. Cytoskel. **61**, 137–144 (2005).
[3]S. Chattopadhyay, R. Moldovan, C. Yeung, and X. L. Wu, "Swimming efficiency of bacterium *Escherichia coli*," Proc. Natl. Acad. Sci. USA. **103**, 13712–13717 (2006).
[4]Y. W. Kim and R. R. Netz, "Pumping fluids with periodically beating grafted elastic filaments," Phys. Rev. Lett. **96**, 158101 (2006).
[5]M. J. Kim and K. S. Breuer, "Microfluidic pump powered by self-organizing bacteria," Small **4**, 111–118 (2008).
[6]E. Lauga and T. R. Powers, "The hydrodynamics of swimming microorganisms," Rep. Prog. Phys. **72**, 096601 (2009).
[7]M. J. Kim and K. S. Breuer, "Enhanced diffusion due to motile bacteria," Phys. Fluids **16**, L78–L81 (2004).
[8]M. J. Kim and K. S. Breuer, "Controlled mixing in microfluidic systems using bacterial chemotaxis," Anal. Chem. **79**, 955–959 (2007).
[9]N. Darnton, L. Turner, K. Breuer, and H. C. Berg, "Moving fluid with bacterial carpets," Biophys. J. **86**, 1863–1870 (2004).
[10]D. B. Weibel, P. Garstecki, D. Ryan, W. R. Diluzio, M. Mayer, J. E. Seto, and G. M. Whitesides, "Microoxen: Microorganisms to move microscale loads," Proc. Natl. Acad. Sci. USA. **102**, 11963–11967 (2005).
[11]G. L. Cooper, A. L. Schiller, and C. C. Hopkins, "Possible role of capillary action in pathogenesis of experimental catheter-associated dermal tunnel infections," J. Clin. Microbiol. **26**, 8–12 (1988).
[12]G. Harkes, J. Dankert, and J. Feijen, "Bacterial migration along solid surfaces," Appl. Environ. Microbiol. **58**, 1500–1505 (1992).
[13]S. S. Suarez and A. A. Pacey, "Sperm transport in the female reproductive tract," Hum. Reprod. Update **12**, 23–37 (2006).
[14]J. W. Costerton, Z. Lewandowski, D. E. Caldwell, D. R. Korber, and H. M. Lappin-Scott, "Microbial biofilms," Annu. Rev. Microbiol. **49**, 711–745 (1995).
[15]M. C. Van Loosdrecht, J. Lyklema, W. Norde, and A. J. Zehnder, "Influence of interfaces on microbial activity," Microbiol. Rev. **54**, 75–87 (1990).
[16]D. F. Katz, "On the propulsion of micro-organisms near solid boundaries," J. Fluid Mech. **64**, 33–49 (1974).
[17]D. F. Katz, T. D. Bloom, and R. H. Bondurant, "Movement of bull spermatozoa in cervical mucus," Biol. Reprod. **25**, 931–937 (1981).
[18]E. Lauga, W. R. DiLuzio, G. M. Whitesides, and H. A. Stone, "Swimming in circles: motion of bacteria near solid boundaries," Biophys. J. **90**, 400–412 (2006).
[19]W. R. DiLuzio, L. Turner, M. Mayer, P. Garstecki, D. B. Weibel, H. C. Berg, and G. M. Whitesides, "*Escherichia coli* swim on the right-hand side," Nature **435**, 1271–1274 (2005).
[20]U. Ruffer and W. Nultsch, "High-speed cinematographic analysis of the movement of *Chlamydomonas*," Cell Motil. **5**, 251–263 (1985).
[21]M. Polin, I. Tuval, K. Drescher, J. P. Gollub, and R. E. Goldstein, "*Chlamydomonas* swims with two 'gears' in a eukaryotic version of run-and-tumble locomotion," Science **325**, 487–490 (2009).
[22]M. Silverman and M. Simon, "Flagellar rotation and the mechanism of bacterial motility," Nature **249**, 73–74 (1974).
[23]J. Lighthill, "Flagellar hydrodynamics - the John von Neumann Lecture, 1975," SIAM Rev. **18**, 161–230 (1976).
[24]G. Taylor, "Analysis of the swimming of microscopic organisms," Proc. R. Soc. Lond. A **209**, 447–461 (1951).
[25]J. Gray, "Undulatory propulsion," Q. J. Microsc. Sci. **94**, 551–578 (1953).
[26]J. Gray and G. J. Hancock, "The propulsion of sea-urchin spermatozoa," J. Exp. Biol. **32**, 802–814 (1955).
[27]J. Gray and H. W. Lissmann, "The locomotion of nematodes," J. Exp. Biol. **41**, 135–154 (1964).
[28]G. Tokic and D. K. P. Yue, "Optimal shape and motion of undulatory swimming organisms," Proc. R. Soc. B **279**, 3065–3074 (2012).
[29]R. G. Cox, "The motion of long slender bodies in a viscous fluid. Part 1. General theory," J. Fluid Mech. **44**, 791–810 (1970).
[30]R. S. Berman, O. Kenneth, J. Sznitman, and A. M. Leshansky, "Undulatory locomotion of finite filaments: lessons from *Caenorhabditis elegans*," New J. Phys. **15**, 075022 (2013).
[31]D. F. Katz, J. R. Blake, and S. L. Paveri-Fontana, "On the movement of slender bodies near plane boundaries at low Reynolds number," J. Fluid Mech. **72**, 529–540 (1975).
[32]N. J. De Mestre, "Low-Reynolds-number fall of slender cylinders near boundaries," J. Fluid Mech. **58**, 641–656 (1973).
[33]R. D. Schulman, M. Backholm, W. S. Ryu, and K. Dalnoki-Veress, "Dynamic force patterns of an undulatory microswimmer," Phys. Rev. E **89**, 050701 (2014).
[34]S. Brenner, "The genetics of *Caenorhabditis elegans*," Genetics **77**, 71–94 (1974).
[35]M. Backholm, W. S. Ryu, and K. Dalnoki-Veress, "Viscoelastic properties of the nematode *Caenorhabditis elegans*, a self-similar, shear-thinning worm," Proc. Natl. Acad. Sci. USA. **110**, 4528–4533 (2013).
[36]C. Fang-Yen, M. Wyart, J. Xie, R. Kawai, T. Kodger, S. Chen, Q. Wen, and A. D. T. Samuel, "Biomechanical analysis of gait adaptation in the nematode *Caenorhabditis elegans*," Proc. Natl. Acad. Sci. USA. **107**, 20323–20328 (2010).
[37]J. Sznitman, X. Shen, R. Sznitman, and P. E. Arratia, "Propulsive force measurements and flow behavior of undulatory swimmers at low Reynolds number," Phys. Fluids **22**, 121901 (2010).
[38]X. N. Shen, J. Sznitman, P. Krajacic, T. Lamitina, and P. E. Arratia, "Undulatory locomotion of *Caenorhabditis elegans* on wet surfaces," Biophys. J. **102**, 2772–2781 (2012).
[39]X. N. Shen and P. E. Arratia, "Undulatory swimming in viscoelastic fluids," Phys. Rev. Lett. **106**, 208101 (2011).
[40]P. Sauvage, M. Argentina, J. Drappier, T. Senden, J. Siméon, and J.-M. Di Meglio, "An elasto-hydrodynamical model of friction for the locomotion of *Caenorhabditis elegans*," J. Biomech. **44**, 1117–1122 (2011).
[41]S. Park, H. Hwang, S.-W. Nam, F. Martinez, R. H. Austin, and W. S. Ryu, "Enhanced *Caenorhabditis elegans* locomotion in a structured microfluidic environment," PLoS One **3**, e2550 (2008).
[42]T. Majmudar, E. E. Keaveny, J. Zhang, and M. J. Shelley, "Experiments and theory of undulatory locomotion in a simple structured medium," J. R. Soc. Interface **9**, 1809–1823 (2012).
[43]G. Juarez, K. Lu, J. Sznitman, and P. E. Arratia, "Motility of small nematodes in wet granular media," Europhys. Lett. **92**, 44002 (2010).
[44]S. Jung, "*Caenorhabditis elegans* swimming in a saturated particulate system," Phys. Fluids **22**, 031903 (2010).
[45]F. Lebois, P. Sauvage, C. Py, O. Cardoso, B. Ladoux, P. Hersen, and J.-M. Di Meglio, "Locomotion control of *Caenorhabditis el-*

egans through confinement," Biophys. J. **102**, 2791–2798 (2012).
[46]A. Ghanbari, V. Nock, S. Johari, R. Blaikie, X. Chen, and W. Wang, "A micropillar-based on-chip system for continuous force measurement of *C. elegans*," J. Micromech. Microeng. **22**, 095009 (2012).
[47]J. C. Doll, N. Harjee, N. Klejwa, R. Kwon, S. M. Coulthard, B. Petzold, M. B. Goodman, and B. L. Pruitt, "SU-8 force sensing pillar arrays for biological measurements," Lab Chip **9**, 1449–1454 (2009).
[48]R. Ghosh and J. Sznitman, "Visualization of nematode *Caenorhabditis elegans* swimming in a liquid drop," J. Vis. **15**, 277–279 (2012).
[49]M.-J. Colbert, A. N. Ragen, C. Fradin, and K. Dalnoki-Veress, "Adhesion and membrane tension of single vesicles and living cells using a micropipette-based technique," Eur. Phys. J. E **30**, 117–121 (2009).
[50]M.-J. Colbert, F. Brochard-Wyart, C. Fradin, and K. Dalnoki-Veress, "Squeezing and detachment of living cells," Biophys. J. **99**, 3555–3562 (2010).
[51]See supplemental material at [URL to be inserted by AIP] for examples of RFT fits for swimming near one and two boundaries, and for movies of the worm swimming before and after confinement.

3.3 Paper III

Tangling of tethered swimmers: Interactions between two nematodes

M. Backholm, R.D. Schulman, W.S. Ryu and K. Dalnoki-Veress, Phys. Rev. Lett., **113**, 138101 (2014).

To study the interactions between two adjacent worms, we perform experiments in which two worms are held nearby one another by micropipettes at controlled separations while swimming in the same plane. Although no appreciable hydrodynamic interactions are witnessed, a striking consequence of steric interactions arises: tangling. The tangling events between the worms generate much larger pipette deflections compared to those associated with ordinary swimming, and thus, tangling events can be detected and counted by closely inspecting the deflection curves. In these experiments, two types of tangles, called 2 and 3 tangles, are identified to reproducibly occur. The name of the tangle is derived from the number of overlapping points present between the worms during a tangle. 3 tangles are found to be more stable and more likely to occur at small separations, compared with 2 tangles.

When the worms are separated by a large distance, no tangles occur. In fact, there is a critical separation within which tangles start to form. By considering the worms' heads as moving laterally in a sinusoidal fashion, a model is derived to predict the onsets of 2 and 3 tangles. The model's predictions are in agreement with the experimental onsets within error.

We find that the experimental probability for the occurence of tangles increases very sharply after the onset. We are able to develop a model to predict how this experimental probability should scale with the separation distance of the worms. Once again, our model's prediction for the probability are in excellent agreement with the expermental data.

Matilda Backholm designed and performed the experiments for this study. I contributed to developing the model to describe the tangling onsets and probabilities. Matilda Backholm composed the drafts, which were subject to editing from me, Kari-Dalnoki-Veress, and William Ryu.

Tangling of Tethered Swimmers: Interactions between Two Nematodes

Matilda Backholm,[1] Rafael D. Schulman,[1] William S. Ryu,[2] and Kari Dalnoki-Veress[1,3,*]
[1]Department of Physics & Astronomy and the Brockhouse Institute for Materials Research, McMaster University, Hamilton, Ontario L8S 4M1, Canada
[2]Department of Physics and the Donnelly Centre, University of Toronto, Toronto, Ontario M5S 1A7, Canada
[3]Laboratoire de Physico-Chimie Théorique, UMR CNRS Gulliver 7083, ESPCI, Paris, France
(Received 9 June 2014; published 23 September 2014)

The tangling of two tethered microswimming worms serving as the ends of "active strings" is investigated experimentally and modeled analytically. *C. elegans* nematodes of similar size are caught by their tails using micropipettes and left to swim and interact at different separations over long times. The worms are found to tangle in a reproducible and statistically predictable manner, which is modeled based on the relative motion of the worm heads. Our results provide insight into the intricate tangling interactions present in active biological systems.

DOI: 10.1103/PhysRevLett.113.138101 PACS numbers: 87.85.gj, 46.70.Hg, 47.63.Gd

Entanglements are ubiquitous in our everyday lives with headphone cords forming braids and knots in our pockets, collections of small items like staples arranging into large tangled networks [1], and hair strands knotting into disordered snarls [2]. A less common example is the knotting of the umbilical cord which occurs at birth for about 1% of the population [3]. At smaller scales, like in the case of DNA, knots occur naturally in the recombination and replication cycles and are thought to contribute to gene regulation [4–6]. Tangling in polymers [7], proteins [3], and the flagella in groups of spermatozoa [8,9] as well as bacteria are further examples. Flagellar entanglements have been shown to stabilize bacterial networks in biofilms [10,11] and also give rise to the well-studied run-and-tumble motion of bacteria, where several flagella are tangled into a propellerlike bundle, allowing for propulsion in a specific direction [12–14].

Over recent years, active networks of, e.g., highly packed bacteria [15,16], cilia [17–20], nematodes [21,22], sperm cells [23], self-locomoting slender rods [24], microtubule filaments [25,26], and colloidal particles [27] have been studied for the purpose of bioengineering applications [28] and understanding the complex, collective interactions present in these living or active liquids [29,30]. In addition to hydrodynamic coupling and collisions, entanglements play a vital role in determining the final physical properties and biological function of the active material. In the case of cilia, for example, the synchronized beating enables locomotion of a variety of microorganisms as well as the transport of mucus from our lungs. Any tangling of the cilium strands would certainly have severe biological consequences.

Mathematicians and physicists have taken a keen interest in understanding the formation and topology of knots and tangles. To spontaneously form a knot, a long and flexible string with a certain excluded volume and bending stiffness has to be given enough energy to move around and explore its surroundings [31]. For very small strings, like polymer chains, thermal energy is sufficient to reptate and entangle the molecules [7]. For larger objects, however, extra energy input is needed, as in the case of the driven helical rotation of bacterial flagella [12–14] or for vigorously shaken ball chains and strings [32–35]. Independent of the formation strategy, the tangle topology can be defined by the Conway notation [36–40].

The formation, lifetime, and untying of knots has been investigated experimentally in macroscopic systems consisting of single strings, chains, and ropes of different lengths and stiffnesses [32–35]. Upon shaking these passive strings, self-induced knots of different types were found, and the knotting probability was theoretically modeled. Most knots form and disappear due to the string ends moving in and out of chain loops and around straight segments of the chain. To the best of our knowledge, this intricate chain end motion has not been closely studied, nor has the interaction between two chain ends.

Here we present a time-resolved experimental system illustrated in Fig. 1(a), probing the dynamic tangling of two

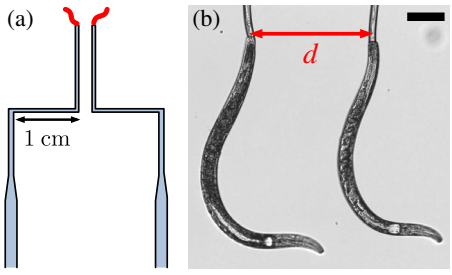

FIG. 1 (color online). (a) Schematic illustration of the experimental setup where two worms were held by *Z*-shaped micropipettes. (b) Optical microscopy image of two young adult *C. elegans* worms swimming at a separation d. Scale bar 200 μm.

small worms serving as active, i.e., self-driven, strings on a millimetric scale. The nematode *Caenorhabditis elegans* is a millimeter-sized microswimmer used as a model organism to probe undulatory locomotion experimentally [41–45]. When tail anchored, *C. elegans* has been shown to move in a highly reproducible, undulatory fashion with a well-defined frequency and amplitude [43]. In our experiments, the nematodes were placed in a buffer solution and held by their tails with long (~2 cm) and thin (~20 μm) micropipettes made as described in Refs. [46,47], and carefully placed side by side at a separation d as shown in Fig. 1(b) (see the Supplemental Material for more experimental details [48]). The motion of the worms was monitored with a camera (56 fps) as shown in the time-lapse snapshots of Fig. 2(a) (see the Supplemental Material movie SM1.avi [48]). The lateral positions of the worm heads were tracked and are plotted as a function of time in Fig. 2(b), where sinusoidal functions have been fit to the three first noninteracting periods of both worms, showing the smooth, undulatory motion of the swimmers.

At close enough distances, the worms were seen to frequently overlap and form temporary tangles. A typical example of the formation of such a tangle is shown by the head positions in Fig. 2(b). The undulatory motion of the slender bodies remains unchanged throughout a tangle, deeming the attempt frequency to untangle the same as the swimming frequency of the worms, which finally exit the locked configuration by moving their heads apart. The undoing of the tangle is sometimes driven by the motion of only one of the worms.

Here, two different types of tangles shown in Figs. 2(c) and 2(d) were found to occur frequently and in a reproducible manner. These could be recognized by the number of overlapping points and are here defined as a 2- and 3-tangle, respectively (in the Conway notation, these tangles would correspond to vertical rational tangles of type $1/2$ and $1/3$ [36]). To understand the formation of these specific tangles, the worms were modeled as strings with an average length $L \sim L_{\mathrm{left}} \sim L_{\mathrm{right}}$ and radius R. Consistent with our observations, the lateral position of the string ends (worm heads) were defined as sinusoidal functions with a maximum amplitude of $A = kL$, where k is an experimentally determinable constant. The left and right string end positions could, thus, be written as $x_L = A\sin(t+\phi)$ and $x_R = A\sin t + d$, respectively, where $\phi \in [0,\pi]$ is the phase shift between the active strings, and $d > 0$ is the distance between their anchors.

The probability of these strings entangling will vanish at large distances and become increasingly probable as the string ends start to overlap, i.e., at some point in time, $x_L \geq x_R$. This results in a critical ratio between the distance and amplitude for any overlap to be possible: $d/A \leq \sin(t+\phi) - \sin t$. For an entanglement to be physically possible, it is not sufficient for only the string ends to overlap. Instead, a certain fraction (L_c/L) of each string needs to be available to form a full tangle with a minimum length of L_c. We, therefore, consider that both worms must have a swimming amplitude such that they reach a distance greater than L_c beyond the symmetry plane [exemplified by the left worm in the second frame of Fig. 2(a)]. Thus, we

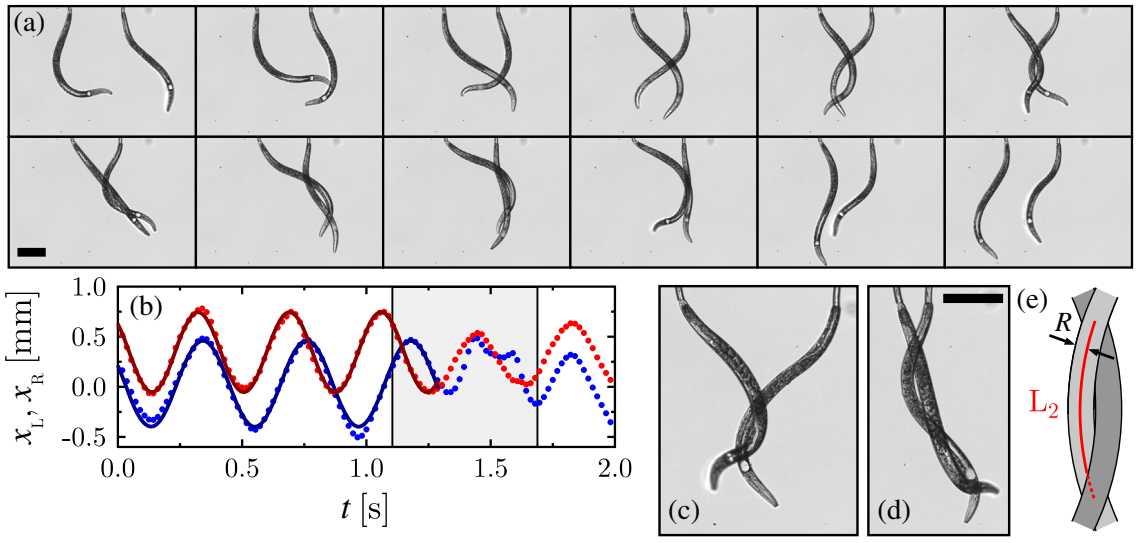

FIG. 2 (color online). (a) Snapshots (0.054 s between each image) showing the tangling of two worms swimming at a distance $d = 370$ μm apart. (b) The lateral position of the heads of the same worms. The worms slowly shift from in-phase to out-of-phase swimming, allowing the heads to overlap and the worms to wrap around each other's bodies and form a tangle. Subsequently, they exit the tangle in phase with the same sinusoidal motion as prior to the tangling event. The gray zone in the graph denotes the time frame of the snapshots in (a) (image of every third data point shown). The solid lines are sinusoidal fits to the head positions of both of the worms. (c),(d) Two worms at different separations forming a 2- and 3-tangle, respectively. (e) A schematic illustration of a 2 tangle modeled as a helix with radius R, twist π, and arc length L_2. All scale bars represent 200 μm.

can state that for a tangle to occur, $A \geq d/2 + L_c$, which yields

$$\frac{L}{d} \geq \left[2\left(k - \frac{L_c}{L}\right)\right]^{-1}. \quad (1)$$

This equation corresponds to an upper bound to the critical ratio between the chain length and distance for an entanglement to be theoretically possible.

The lowest-order tangle seen in our system is the 2 rational tangle [Fig. 2(c)] illustrated schematically in Fig. 2(e). This tangle can be described as a helix with a radius R (the same as the worm radius), curvature κ, and twist π. The arc length (minimum string length required for this tangle) then is $L_c = L_2 = \pi\sqrt{R/\kappa}$. The proportionality constant relating the maximum swimming amplitude (see the Supplemental Material [48]) to the worm length has been measured as $k = 0.8 \pm 0.05$ for single worms. By measuring the mean radius and length of the worms used in this study (young adults and adults, $R = 29 \pm 2$ μm and $L = 1080 \pm 70$ μm) and the mean of the absolute curvature of the first (anterior) half of their bodies in a state of normal swimming ($\kappa = 3.3 \pm 0.2$ mm^{-1}), an estimate of $L_2/L = 0.27 \pm 0.02$ could, thus, be made. By applying the helix model to Eq. (1), the predicted critical ratio between the worm length and distance for any entanglement to be possible is $(L/d)_2 \geq 0.95 \pm 0.10$. Following the same approach, the critical ratio for a 3 tangle modeled as a helix with a twist of 2π is calculated as $(L/d)_3 = 2.0 \pm 0.3$.

The experiments were performed at different distances with several pairs of worms of similar size. In a particular experiment, the presence of 2- and 3-tangles were noted. In Fig. 3(a), we plot if a tangle could be observed at a given ratio L/d and also indicate the type of tangle. The two vertical lines in the graph denote the theoretically predicted critical ratios $(L/d)_2$ and $(L/d)_3$, and the experimental onsets are, within error, in excellent agreement with the model. Note that 2 tangles were always present in experiments in which 3 tangles were observed.

In Figs. 3(b) and 3(c), the distributions of entanglement lifetimes are shown for several experiments performed in the two extreme cases of large ($L/d = 1.0 \pm 0.2$) and small ($L/d = 5.7 \pm 2.8$) separations, respectively (for further details, see the Supplemental Material [48]). At the larger separation, only 2 tangles are possible and have an average lifetime of $\tau_2 = 0.18 \pm 0.03$ s. However, for the shorter separation, both 2- and 3-tangles were possible, and this is clearly seen in Fig. 3(c) where a shoulder around $\tau_3 \approx 0.4$ s $\approx 2\tau_2$ has formed due to the occurrence of the more long-lived 3 tangle stabilized by an additional crossing which requires extra time to become undone. Note that, as one might expect, even for short distances, the 3 tangles are much less probable than 2 tangles. A slight shift and widening of the 2 peak at close distances is also apparent

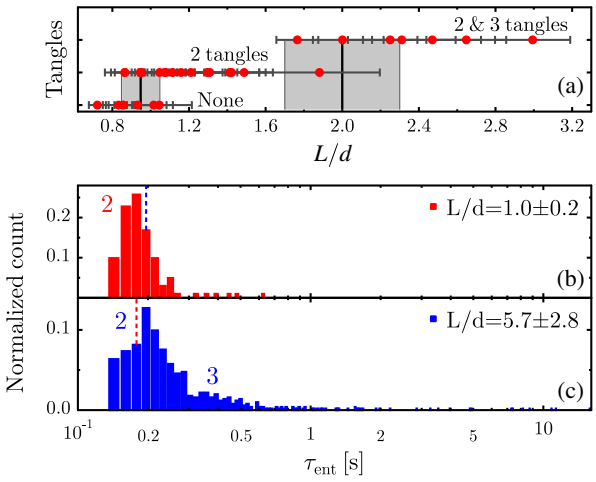

FIG. 3 (color online). (a) The experimental onset of 2- and 3-tangles (filled circles) with horizontal error bars as a function of the worm length-distance ratio. The vertical lines are the theoretical crossover predictions $(L/d)_2 = 0.95 \pm 0.10$ and $(L/d)_3 = 2.0 \pm 0.3$. (b),(c) Histograms of the entanglement lifetimes of several worm pairs far apart [$L/d = 1.0 \pm 0.2$, (b)] and close together [$L/d = 5.7 \pm 2.8$, (c)]. The count has been normalized with the total number of tangles. The vertical dashed lines indicate the peak position of the other histogram.

when comparing the two distributions [see vertical dashed lines in Figs. 3(b) and 3(c)], indicating more variations in the tangling events as the worms are brought closer together. A few 3 tangles remained stable for around 10 s, which corresponds to over 20 full swimming cycles (untangling attempts). These dynamic tangles were beating and rotating reminiscent of bacterial bundles (see the Supplemental Material movie SM2.avi [48]). Variables that affect the tangle stability are the length, thickness, and bending stiffness of the worms, the attempt frequency to untangle, the friction between the worms [49], as well as contact between the worms eliciting mechanosensory responses [50]. The latter of these has previously been shown not to affect the collective swimming of *C. elegans* [21] and did not seem to strongly affect the tangling dynamics in our experiments either.

To investigate the entanglement probability as L/d increases above the critical ratios derived above, we now follow the lateral motion of the point (x_c) on the worm body located at a distance of L_c from the head. Since the worm propagates traveling waves down its body, $x_c(t)$ can also be modeled as a sinusoidal function with an amplitude $A_c = k_c L$, where k_c is an experimentally determinable constant. For the left and right worms, we thereby have $x_{c,L} = A_c \sin(t + \phi)$ and $x_{c,R} = A_c \sin t + d$, respectively. At a given separation distance, these sinusoidal functions intersect at a range of phase shifts above some critical value. For an entanglement to be possible, the maximum value of the difference $\Delta = x_{c,L} - x_{c,R}$ needs to be greater than zero. Using a trigonometric

identity, $x_{c,L} - x_{c,R} = 2A_c \cos[(2t+\phi)/2]\sin(\phi/2) - d$. Maximizing this difference with respect to time yields $\Delta = 2A_c \sin(\phi/2) - d \geq 0$ and, thus,

$$\phi \geq \phi_c = 2\sin^{-1}\left(\frac{d}{2A_c}\right). \quad (2)$$

This is the critical phase shift needed to form a tangle at a specific L/d ratio. In other words, the farther apart the worms are, the more out of phase they have to swim in order to intersect and the smaller is the range of phase shifts which yield intersections.

Although the worms have very similar average frequencies ($f = 2.1 \pm 0.2$ Hz), small temporal variations in this quantity allow the worms to explore all relative phase shifts, as exemplified in Fig. 2(b). Since the worms explore all relative phase shifts over time, and since a certain fraction of intersection events between the worm ends will lead to entanglements, it is reasonable to hypothesize that the entanglement probability will be proportional to the fraction of relative phase shifts which contain an intersection at the separation distance d. However, we also expect that entanglement events will be more likely to occur if the worm heads have more space (and time) to wrap around each other's bodies. Thus, we make the first-order assumption that the probability of entanglements at a given separation distance is proportional to the fraction of relative phase shifts which contain an intersection but where each phase shift is linearly weighted by the maximum separation between the worm heads, giving

$$p \propto \int_{\phi_c}^{\pi} \frac{\Delta}{L} d\phi, \quad (3)$$

where L is used to nondimensionalize the weighting. Evaluating this integral and substituting $A_c = k_c L$ gives

$$p \propto 2k_c\sqrt{4 - \left(\frac{d}{k_c L}\right)^2} - \frac{d}{L}\left[\pi - 2\sin^{-1}\left(\frac{d}{2k_c L}\right)\right], \quad (4)$$

which shows how the entanglement probability scales with the worm length-distance ratio.

The number of worm entanglements were counted, and the experimental entanglement probability was calculated as the ratio between the number of entanglements and entanglement attempts (the sum of the number of swimming cycles and successful tangling events). The probability is plotted as a function of L/d in Fig. 4 for all experiments performed with different worm pairs at different distances. The entanglement probability increases sharply at a worm separation close to one worm length. Equation (4) is successfully fit to the data, and the model is clearly in excellent agreement with the experimental observations. Two fitting parameters were used to fit the data in Fig. 4. The first is a compressing factor (0.11 ± 0.03) in the y direction, which corresponds to the proportionality prefactor of Eq. (4). Any mechanosensory interactions present between the worms would enter into this factor. The second fitting parameter defines the horizontal shift of the theoretical curve and is given by $k_c = 0.64 \pm 0.10$. Comparing this value to that derivable from the helix model giving $A_{c,\mathrm{helix}}/L = k - L_2/L = 0.53 \pm 0.05$, we find the two models to be, within error, in excellent agreement.

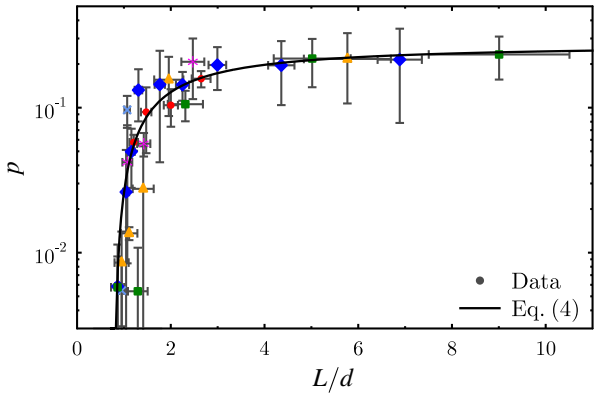

FIG. 4 (color online). The entanglement probability as a function of L/d. The different markers denote experiments with different worm pairs. The solid line is the analytical fit of Eq. (4) to the data.

To form a tangle in our experiments, the worms were forced to deviate from their otherwise planar swimming motion to form a three-dimensional helix. If significant out-of-plane swimming occurred, the entanglement probability was seen to vastly decrease, as easily explained by our geometric model. The clear entanglement difference between the nearly 2D versus a complete 3D motion could, thus, be a significant factor in, e.g., how arrays of cilia avoid tangling due to their sophisticated 3D motion [51]. The aspect ratio of cilia can be as high as $L/D = 100$ (versus 19 for our worms), where D is the diameter. Since cilia are typically arranged at distances 0.27–0.4 μm apart [52], $(L/d)_{\mathrm{cilia}} = 75$. The lack of ciliar entanglements is, thus, surprising when compared to our experimental findings in planar swimming and highlights the importance of the specific motion patterns used to avoid or achieve a tangled network. Strong hydrodynamic interactions could also act to modify ciliar entanglements at close distances. Hydrodynamic interactions were not discovered between the worms in our experiments, consistent with the findings of others [21].

Here we have presented a time-resolved, dynamic study of the tangling of active stringlike worms. By describing the system with a simple model based on the overlap probability of the worm heads during their undulatory swimming, the critical ratio between the worm length and distance for any entanglement to be possible was

quantitatively predicted and shown to be in excellent agreement with experimental observations. Furthermore, the entanglement probability was analytically derived and successfully fit to the data. It is clear that the tangling of the active strings is far from random but a statistically predictable process based on the relative motion of their ends. These experiments provide an interesting model system to understand the intricate interactions present in active matter such as cilia and bacterial flagella.

The financial support by NSERC of Canada is gratefully acknowledged. The authors also thank Solomon Barkley for helpful discussions.

*dalnoki@mcmaster.ca

[1] N. Gravish, S. V. Franklin, D. L. Hu, and D. I. Goldman, Phys. Rev. Lett. **108**, 208001 (2012).
[2] D. T. English and H. E. Jones, Arch. Dermatol. **107**, 77 (1973).
[3] A. Goriely, in *Physical and Numerical Models in Knot Theory*, edited by J. A. Calvo, K. C. Millett, E. J. Rawdon, and A. Stasiak (World Scientific, Singapore, 2005), Chap. 6.
[4] S. A. Wasserman and N. R. Cozzarelli, Science **232**, 951 (1986).
[5] E. Ercolini, F. Valle, J. Adamcik, G. Witz, R. Metzler, P. De Los Rios, J. Roca, and G. Dietler, Phys. Rev. Lett. **98**, 058102 (2007).
[6] J. Tang, N. Du, and P. S. Doyle, Proc. Natl. Acad. Sci. U.S.A. **108**, 16153 (2011).
[7] P.-G. de Gennes, Macromolecules **17**, 703 (1984).
[8] K. J. Eckelbarger, C. M. Young, and J. L. Cameron, Biol. Bull. **176**, 257 (1989).
[9] D. M. Woolley and G. G. Vernon, J. Exp. Biol. **204**, 1333 (2001).
[10] C. J. Ingham and E. Ben-Jacob, BMC Microbiol. **8**, 36 (2008).
[11] D. O. Serra, A. M. Richter, G. Klauck, F. Mika, and R. Hengge, mBio **4**, e00103-13 (2013).
[12] L. Turner, W. S. Ryu, and H. C. Berg, J. Bacteriol. **182**, 2793 (2000).
[13] R. M. Macnab, Proc. Natl. Acad. Sci. U.S.A. **74**, 221 (1977).
[14] M. Kim, J. C. Bird, A. J. Van Parys, K. S. Breuer, and T. R. Powers, Proc. Natl. Acad. Sci. U.S.A. **100**, 15481 (2003).
[15] M. F. Copeland and D. B. Weibel, Soft Matter **5**, 1174 (2009).
[16] J. Dunkel, S. Heidenreich, K. Drescher, H. H. Wensink, M. Bär, and R. E. Goldstein, Phys. Rev. Lett. **110**, 228102 (2013).
[17] L. Gheber and Z. Priel, Biophys. J. **55**, 183 (1989).
[18] S. Gueron, K. Levit-Gurevich, N. Liron, and J. J. Blum, Proc. Natl. Acad. Sci. U.S.A. **94**, 6001 (1997).
[19] P. Lenz and A. Ryskin, Phys. Biol. **3**, 285 (2006).
[20] S. Michelin and E. Lauga, Phys. Fluids **22**, 111901 (2010).
[21] J. Yuan, D. M. Raizen, and H. H. Bau, Proc. Natl. Acad. Sci. U.S.A. **111**, 6865 (2014).
[22] S. Gart, D. Vella, and S. Jung, Soft Matter **7**, 2444 (2011).
[23] H. S. Fisher, L. Giomi, H. E. Hoekstra, and L. Mahadevan, Proc. R. Soc. B **281**, 20140296 (2014).
[24] D. Saintillan and M. J. Shelley, Phys. Rev. Lett. **99**, 058102 (2007).
[25] T. Sanchez, D. Welch, D. Nicastro, and Z. Dogic, Science **333**, 456 (2011).
[26] T. Sanchez, D. T. N. Chen, S. J. DeCamp, M. Heymann, and Z. Dogic, Nature (London) **491**, 431 (2012).
[27] A. Bricard, J.-B. Caussin, N. Desreumaux, O. Dauchot, and D. Bartolo, Nature (London) **503**, 95 (2013).
[28] N. Darnton, L. Turner, K. Breuer, and H. Berg, Biophys. J. **86**, 1863 (2004).
[29] D. L. Koch and G. Subramanian, Annu. Rev. Fluid Mech. **43**, 637 (2011).
[30] T. Vicsek and A. Zafeiris, Phys. Rep. **517**, 71 (2012).
[31] A. Belmonte, Proc. Natl. Acad. Sci. U.S.A. **104**, 17243 (2007).
[32] A. Belmonte, M. J. Shelley, S. T. Eldakar, and C. H. Wiggins, Phys. Rev. Lett. **87**, 114301 (2001).
[33] E. Ben-Naim, Z. A. Daya, P. Vorobieff, and R. E. Ecke, Phys. Rev. Lett. **86**, 1414 (2001).
[34] J. Hickford, R. Jones, S. Courrech du Pont, and J. Eggers, Phys. Rev. E **74**, 052101 (2006).
[35] D. M. Raymer and D. E. Smith, Proc. Natl. Acad. Sci. U.S.A. **104**, 16432 (2007).
[36] J. H. Conway, in *Computational Problems in Abstract Algebra*, edited by J. Leech (Pergamon Press, New York, 1969), pp. 329–358.
[37] S. A. Bleiler, Trans. Am. Math. Soc. **282**, 385 (1984).
[38] J. R. Goldman and L. H. Kauffman, Adv. Appl. Math. **18**, 300 (1997).
[39] L. H. Kauffman and S. Lambropoulou, Adv. Appl. Math. **33**, 199 (2004).
[40] D. Meluzzi, D. E. Smith, and G. Arya, Annu. Rev. Biophys. **39**, 349 (2010).
[41] S. Brenner, Genetics **77**, 71 (1974).
[42] M. Backholm, W. S. Ryu, and K. Dalnoki-Veress, Proc. Natl. Acad. Sci. U.S.A. **110**, 4528 (2013).
[43] R. D. Schulman, M. Backholm, W. S. Ryu, and K. Dalnoki-Veress, Phys. Rev. E **89**, 050701 (2014).
[44] P. Sauvage, M. Argentina, J. Drappier, T. Senden, J. Siméon, and J.-M. Di Meglio, J. Biomech. **44**, 1117 (2011).
[45] X. N. Shen and P. E. Arratia, Phys. Rev. Lett. **106**, 208101 (2011).
[46] M.-J. Colbert, A. N. Raegen, C. Fradin, and K. Dalnoki-Veress, Eur. Phys. J. E **30**, 117 (2009).
[47] M.-J. Colbert, F. Brochard-Wyart, C. Fradin, and K. Dalnoki-Veress, Biophys. J. **99**, 3555 (2010).
[48] See Supplemental Material http://link.aps.org/supplemental/10.1103/PhysRevLett.113.138101 for experimental details and movies of the worms tangling.
[49] J. H. Maddocks and J. B. Keller, SIAM J. Appl. Math. **47**, 1185 (1987).
[50] R. O'Hagan and M. Chalfie, International review of neurobiology **69**, 169 (2005).
[51] A. Vilfan and F. Jülicher, Phys. Rev. Lett. **96**, 058102 (2006).
[52] Z. Teff, Z. Priel, and L. A. Gheber, Biophys. J. **92**, 1813 (2007).

Chapter 4

Conclusions

In the work presented in this thesis, we have aimed to understand the hydrodynamics associated with the swimming of the model organism *C. elegans* using a micropipette deflection technique to measure forces. Although the nematode lives at a Reynolds number for which inertial effects may be important, it appears that viscous forces are able to fully describe the relevant hydrodynamics. In particular, although RFT is derived in the limit of $\mathrm{Re} = 0$, it exactly captures the worm's lateral and propulsive forces, which we have measured. By fitting the predictions of RFT to experimental data, we have extracted the worm's drag coefficients, for which we have fixed $K = 1.5$. The measured drag coefficients are in agrement with Lighthill's predictions (Eq. 1.27) within error. Lighthill's study contains the most sophisticated derivation of c_{T} and c_{N}, so it is not surprising that our measured values are in better agreement with his results rather than those of Gray and Hancock (Eq. 1.25). This work comprises the first experimental determination of the drag coefficients of *C. elegans*.

Furthermore, we have investigated the effects of nearby solid boundaries on the swimming of the worm. In particular, we have found that the drag forces experienced by the nematode increase near the interfaces, as we may have anticipated from the discussion in Sec. 1.5. Once again, RFT captures the measured force curves well at all distances from the boundary. In the RFT fits of this work, we have treated both c_{T} and c_{N} (K free to vary) as free parameters. The drag coefficients increase upon approaching solid boundaries. However, we have found that K assumes a constant value of $1.5 \pm 0.1(5)$ at all distances from a single boundary, whereas K increases

beyond a value of 2 in channel confinement. This comprises the first experimental evidence of K increasing beyond the limiting value of 2 near solid boundaries, and is consistent with the prediction made by Katz *et al.* in their study. We have also observed the worm to modulate its gait as it is subjected to higher confinements, and thus, larger drag forces. This gait modulation is typically studied by altering the viscosity of the buffer solution. However, confinement offers a lucrative alternative for studying the transition, as it avoids altering the chemical composition of the worm's environment.

Lastly, we have studied the tangling events between two worms swimming adjacent to one another at controlled separations. In this work, there is no evidence of hydrodynamic interactions between the worms. Simple geometric models produce predictions for the onset and probability of tangles as a function of separation, and are in good agreement with the experimental results.

In all this work, we have aimed to address some of the questions posed in the introduction to this thesis. In particular, how well do current theoretical models describe the forces of microswimmers? How do microscopic swimmers interact with nearby boundaries? And, what are the interactions between nearby swimmers? Although much research remains to be done to fully answer these questions and others of similar kind, I hope that this thesis work will supplement the current understanding within the field as a whole.

Bibliography

[1] E. M. Purcell. Life at low Reynolds-number. *Am. J. Phys.*, 45(1):3–11, 1977.

[2] M. J. Kim and K. S. Breuer. Enhanced diffusion due to motile bacteria. *Phys. Fluids*, 16(9):L78–L81, 2004.

[3] M. J. Kim and K. S. Breuer. Controlled mixing in microfluidic systems using bacterial chemotaxis. *Anal. Chem.*, 79(3):955–959, 2007.

[4] Y. W. Kim and R. R. Netz. Pumping fluids with periodically beating grafted elastic filaments. *Phys. Rev. Lett.*, 96(15):158101, 2006.

[5] M. J. Kim and K. S. Breuer. Microfluidic pump powered by self-organizing bacteria. *Small*, 4(1):111–118, 2008.

[6] E. Lauga and Thomas R. Powers. The hydrodynamics of swimming microorganisms. *Rep. Prog. Phys.*, 72(9):096601, 2009.

[7] N. Darnton, L. Turner, K. Breuer, and H. C. Berg. Moving fluid with bacterial carpets. *Biophys. J.*, 86(3):1863–1870, 2004.

[8] D. B. Weibel, P. Garstecki, D. Ryan, W. R. Diluzio, M. Mayer, J. E. Seto, and G. M. Whitesides. Microoxen: Microorganisms to move microscale loads. *Proc. Natl. Acad. Sci. USA.*, 102(34):11963–11967, 2005.

[9] R. P. McCord, J. N. Yukich, and K. K. Bernd. Analysis of force generation during flagellar assembly through optical trapping of free-swimming *Chlamydomonas reinhardtii*. *Cell Motil. Cytoskel.*, 61(3):137–144, 2005.

[10] S. Chattopadhyay, R. Moldovan, C. Yeung, and X. L. Wu. Swimming efficiency of bacterium *Escherichia coli*. *Proc. Natl. Acad. Sci. USA.*, 103(37):13712–13717, 2006.

[11] D. J. Acheson. *Elementary fluid dynamics*. Oxford University Press, 1990.

[12] T. E. Faber. *Fluid dynamics for physicists*. Cambridge University Press, 1995.

[13] Clay Mathematics Institute. Millennium problems. http://http://www.claymath.org/millennium-problems. Online, accessed: 2014-06-25.

[14] P.-G. De Gennes, F. Brochard-Wyart, and D. Quéré. *Capillarity and wetting phenomena: drops, bubbles, pearls, waves*. Springer, 2003.

[15] D. Rind. Complexity and climate. *Science*, 284(5411):105–107, 1999.

[16] N. Cohen and J. H. Boyle. Swimming at low reynolds number: a beginners guide to undulatory locomotion. *Contemp. Phys.*, 51(2):103–123, 2010.

[17] E. Lauga. Life around the scallop theorem. *Soft Matter*, 7(7):3060–3065, 2011.

[18] E. Lauga and D. Bartolo. No many-scallop theorem: Collective locomotion of reciprocal swimmers. *Phys. Rev. E*, 78(3):030901, 2008.

[19] H. C. Berg and R. A. Anderson. Bacteria swim by rotating their flagellar filaments. *Nature*, 245(5425):380, 1973.

[20] U. Ruffer and W. Nultsch. High-speed cinematographic analysis of the movement of *Chlamydomonas*. *Cell Motil.*, 5(3):251–263, 1985.

[21] M. Polin, I. Tuval, K. Drescher, J. P. Gollub, and R. E. Goldstein. *Chlamydomonas* swims with two 'gears' in a eukaryotic version of run-and-tumble locomotion. *Science*, 325(5939):487–490, 2009.

[22] I. R. Gibbons. Cilia and flagella of eukaryotes. *J. Cell Biol.*, 91(3):107s–124s, 1981.

[23] G. Tokic and Yue D. K. P. Optimal shape and motion of undulatory swimming organisms. *Proc. R. Soc. B*, 279(1740):3065–3074, 2012.

[24] J. Gray and H. W. Lissmann. The locomotion of nematodes. *J. Exp. Biol.*, 41(1):135–154, 1964.

[25] G. Taylor. Analysis of the swimming of microscopic organisms. *Proc. R. Soc. Lond. A*, 209(1099):447–461, 1951.

[26] A. J. Reynolds. The swimming of minute organisms. *J. Fluid Mech.*, 23(2):241–360, 1965.

[27] G. J. Hancock. The self-propulsion of microscopic organisms through liquids. *Pro. R. Soc. Lond. A. Math. Phys. Sci.*, 217(1128):96–121, 1953.

[28] J. Lighthill. Flagellar hydrodynamics - the John von Neumann Lecture, 1975. *SIAM Rev.*, 18(2):161–230, 1976.

[29] J. Gray and G. J. Hancock. The propulsion of sea-urchin spermatozoa. *J. Exp. Biol.*, 32(4):802–814, 1955.

[30] R. G. Cox. The motion of long slender bodies in a viscous fluid. Part 1. General theory. *J. Fluid Mech.*, 44(4):791–810, 1970.

[31] B. M. Friedrich, I. H. Riedel-Kruse, J. Howard, and F. Jülicher. High-precision tracking of sperm swimming fine structure provides strong test of resistive force theory. *J. Exp. Biol.*, 213(8):1226–1234, 2010.

[32] N. C. Darnton, L. Turner, S. Rojevsky, and H. C. Berg. On torque and tumbling in swimming *Escherichia coli*. *J. Bacteriol.*, 189(5):1756–1764, 2007.

[33] K. Drescher, J. Dunkel, L. H. Cisneros, S. Ganguly, and R. E. Goldstein. Fluid dynamics and noise in bacterial cell–cell and cell–surface scattering. *Proc. Natl. Acad. Sci. USA.*, 108(27):10940–10945, 2011.

[34] Z. Costerton, J . W.and Lewandowski, D. E. Caldwell, D. R. Korber, and H. M. Lappin-Scott. Microbial biofilms. *Annu. Rev. Microbiol.*, 49(1):711–745, 1995.

[35] M. C. Van Loosdrecht, J. Lyklema, W. Norde, and A. J. Zehnder. Influence of interfaces on microbial activity. *Microbiol. Rev.*, 54(1):75–87, 1990.

[36] S. S. Suarez and A. A. Pacey. Sperm transport in the female reproductive tract. *Hum. Reprod. Update*, 12(1):23–37, 2006.

[37] G. L. Cooper, A. L. Schiller, and C. C. Hopkins. Possible role of capillary action in pathogenesis of experimental catheter-associated dermal tunnel infections. *J. Clin. Microbiol.*, 26(1):8–12, 1988.

[38] G. Harkes, J. Dankert, and J. Feijen. Bacterial migration along solid surfaces. *Appl. Environ. Microbiol.*, 58(5):1500–1505, 1992.

[39] D. F. Katz. On the propulsion of micro-organisms near solid boundaries. *J. Fluid Mech.*, 64(1):33–49, 1974.

[40] D. F. Katz, J. R. Blake, and S. L. Paveri-Fontana. On the movement of slender bodies near plane boundaries at low Reynolds number. *J. Fluid Mech.*, 72(3):529–540, 1975.

[41] L. J. Fauci and A. McDonald. Sperm motility in the presence of boundaries. *Bull. Math. Biol.*, 57(5):679–699, 1995.

[42] D. F. Katz, T. D. Bloom, and R. H. Bondurant. Movement of bull spermatozoa in cervical mucus. *Biol. Reprod.*, 25(5):931–937, 1981.

[43] E. Lauga, W. R. DiLuzio, G. M. Whitesides, and H. A. Stone. Swimming in circles: motion of bacteria near solid boundaries. *Biophys. J.*, 90(2):400–412, 2006.

[44] W. R. DiLuzio, L. Turner, M. Mayer, P. Garstecki, D. B. Weibel, H. C. Berg, and G. M. Whitesides. *Escherichia coli* swim on the right-hand side. *Nature*, 435(7046):1271–1274, 2005.

[45] N. H. Mendelson, A. Bourque, K. Wilkening, K. R. Anderson, and J. C. Watkins. Organized cell swimming motions in bacillus subtilis colonies: patterns of short-lived whirls and jets. *J. Bacteriol.*, 181(2):600–609, 1999.

[46] A. Sokolov, I. S. Aranson, J. O. Kessler, and R. E. Goldstein. Concentration dependence of the collective dynamics of swimming bacteria. *Phys. Rev. Lett.*, 98(15):158102, 2007.

[47] H. Moore, K. Dvorakova, N. Jenkins, and W. Breed. Exceptional sperm cooperation in the wood mouse. *Nature*, 418(6894):174–177, 2002.

[48] H. D. Moore and D. A. Taggart. Sperm pairing in the opossum increases the efficiency of sperm movement in a viscous environment. *Biol. Reprod.*, 52(4):947–953, 1995.

[49] F. Hayashi. Sperm co-operation in the fishfly, parachauliodes japonicus. *Funct. Ecol.*, 12(3):347–350, 1998.

[50] D. R. Brumley, K. Y. Wan, M. Polin, and R. E. Goldstein. Flagellar synchronization through direct hydrodynamic interactions. *eLife*, 3:e02750, 2014.

[51] L. J. Fauci. Interaction of oscillating filaments: a computational study. *J. Comput. Phys.*, 86(2):294–313, 1990.

[52] R. M. Macnab. Bacterial flagella rotating in bundles: a study in helical geometry. *Proc. Natl. Acad. Sci. USA.*, 74(1):221–225, 1977.

[53] S. Gart, D. Vella, and S. Jung. The collective motion of nematodes in a thin liquid layer. *Soft Matter*, 7(6):2444–2448, 2011.

[54] J. Yuan, D. M. Raizen, and H. H. Bau. Gait synchronization in caenorhabditis elegans. *Proc. Natl. Acad. Sci. USA.*, 111(19):6865–6870, 2014.

[55] B. Wood. *The nematode Caenorhabditis elegans*. Cold Spring Harbor Laboratory Press, New York, 1988.

[56] S. Brenner. The genetics of *Caenorhabditis elegans*. *Genetics*, 77(1):71–94, 1974.

[57] L. Byerly, R.C. Cassada, and R. L. Russell. The life cycle of the nematode *Caenorhabditis elegans*: I. Wild-type growth and reproduction. *Dev. Biol.*, 51(1):23–33, 1976.

[58] S.-J. Park, M. B. Goodman, and B. L. Pruitt. Analysis of nematode mechanics by piezoresistive displacement clamp. *Proc. Natl. Acad. Sci. USA.*, 104(44):17376–17381, 2007.

[59] M. Backholm, W. S. Ryu, and K. Dalnoki-Veress. Viscoelastic properties of the nematode *Caenorhabditis elegans*, a self-similar, shear-thinning worm. *Proc. Natl. Acad. Sci. USA.*, 110(12):4528–4533, 2013.

[60] G. Juarez, K. Lu, J. Sznitman, and P. E. Arratia. Motility of small nematodes in wet granular media. *Europhys. Lett.*, 92(4):44002, 2010.

[61] S. Jung. *Caenorhabditis elegans* swimming in a saturated particulate system. *Phys. Fluids*, 22(3):031903, 2010.

[62] X. N. Shen, J. Sznitman, P. Krajacic, T. Lamitina, and P. E. Arratia. Undulatory locomotion of *Caenorhabditis elegans* on wet surfaces. *Biophys. J.*, 102(12):2772–2781, 2012.

[63] X. N. Shen and P. E. Arratia. Undulatory swimming in viscoelastic fluids. *Phys. Rev. Lett.*, 106(20):208101, 2011.

[64] D.A. Gagnon, X. N. Shen, and P. E. Arratia. Undulatory swimming in fluids with polymer networks. *Europhys. Lett.*, 104(1):14004, 2013.

[65] S. Park, H. Hwang, S.-W. Nam, F. Martinez, R. H. Austin, and W. S. Ryu. Enhanced *Caenorhabditis elegans* locomotion in a structured microfluidic environment. *PLoS One*, 3(6):e2550, 2008.

[66] T. Majmudar, E. E. Keaveny, J. Zhang, and M. J. Shelley. Experiments and theory of undulatory locomotion in a simple structured medium. *J. R. Soc. Interface*, 9(73):1809–1823, 2012.

[67] J. Sznitman, X. Shen, R. Sznitman, and P. E. Arratia. Propulsive force measurements and flow behavior of undulatory swimmers at low Reynolds number. *Phys. Fluids*, 22(12):121901, 2010.

[68] C. Fang-Yen, M. Wyart, J. Xie, R. Kawai, T. Kodger, S. Chen, Q. Wen, and A. D. T. Samuel. Biomechanical analysis of gait adaptation in the nematode *Caenorhabditis elegans*. *Proc. Natl. Acad. Sci. USA.*, 107(47):20323–20328, 2010.

[69] P. Krajacic, X. Shen, P. K. Purohit, P. Arratia, and T. Lamitina. Biomechanical profiling of *Caenorhabditis elegans motility*. *Genetics*, 191(3):1015–1021, 2012.

[70] A. Ghanbari, V. Nock, S. Johari, R. Blaikie, X. Chen, and W. Wang. A micropillar-based on-chip system for continuous force measurement of *C. elegans*. *J. Micromech. Microeng.*, 22(9):095009, 2012.

[71] J. C. Doll, N. Harjee, N. Klejwa, R. Kwon, S. M. Coulthard, B. Petzold, M. B. Goodman, and B. L. Pruitt. SU-8 force sensing pillar arrays for biological measurements. *Lab Chip*, 9(10):1449–1454, MAY 2 2009.

[72] F. Lebois, P. Sauvage, C. Py, O. Cardoso, B. Ladoux, P. Hersen, and J.-M. Di Meglio. Locomotion control of *Caenorhabditis elegans* through confinement. *Biophys. J.*, 102(12):2791–2798, 2012.

[73] M.-J. Colbert, A. N. Ragen, C. Fradin, and K. Dalnoki-Veress. Adhesion and membrane tension of single vesicles and living cells using a micropipette-based technique. *Eur. Phys. J. E*, 30:117–121, 2009.

[74] M.-J. Colbert, F. Brochard-Wyart, C. Fradin, and K. Dalnoki-Veress. Squeezing and detachment of living cells. *Biophys. J.*, 99(11):3555–3562, 2010.